THE UNIVERSITY *of* EDINBURGH

Simulations of Dynamics and Motility in Active Fluids

Ana Regina Fialho

Doctor of Philosophy
The University of Edinburgh
March 2020

Lay Summary

Nonequilibrium physics studies systems which are constantly changing over time due, for example, to a permanent flux of energy. It is possible to distinguish between two different types of nonequilibrium systems: driven or active; the latter is the topic of this thesis. In driven systems the energy is taken in from an external source. For example, a pot of water boiling on the stove due to the heat from the flame; or a river flowing downhill because the slope creates a difference in the gravitational energy. In active systems however, the energy source is internal. Standard examples of active systems can be found in nature and include bird flocks, fish shoals, and herds of sheep. In all three examples, the animals - which represent the active particles constituting the system - burn their own chemical energy in order to move. Thus, each one of them acts as an energy source for the system. We also know, from observing these animals in the wild, that they can often move in a seemingly coordinated way. This is an example of the interesting collective phenomena that can be found in active systems.

Of the three previous examples, only fish swim in a fluid, making them a "wet" active system. Swimming organisms deserve a special distinction because they can interact, or "communicate", through the fluid. When one of them moves, it perturbs the liquid around, creating a flow that can be transmitted to its neighbours. We can find more examples of swimming active particles by diving into the microscopic biological world. Bacteria and algae use strokes of their flagella to roam in aqueous mediums, looking for food. Inside our own cells, there are also structures that move through the cytoplasm using active motors. These are responsible for the cell structure, help guide cellular division, and are also involved in muscular contraction.

When microscopic organisms or intracellular filaments and motors swim, they generate stresses on the fluid around by pushing, pulling or rotating it. For instance, *E. coli* moves by helically rotating a bundle of flagella located at its

rear. *E. coli* is, at the same time, pushing the fluid to move forward and rotating it in a screw like fashion. The stresses generated by active movement, or active stresses, are the basis of our study.

We first look at an active system enclosed in a droplet. This is a very simplified model for a cell or a colony of bacteria. We find that the active stresses can drive the droplet into a range of motile states. For example, the droplet can either move forward in a straight line or rotate in place. This depends on whether the active particles are pinned at the surface or not. Both types of movement are mediated by the collective organisation of active particles inside the droplet.

In the second part of the thesis, we focus on the microscopic rotations and torques generated by active particle movement. The reason rotations are involved in biological motility is that biological structures are often chiral, *i.e.* different from their mirror image, or left-right asymmetric. The same is true for many macroscopic organisms. For example, humans and other vertebrates have their heart and lungs positioned in a way that is left-right asymmetric. Understanding the mechanisms behind this asymmetry is one of the most interesting open questions in developmental biology. Here, by means of computer simulations, we investigate systems of microscopic chiral particles. Our results show that the chirality propagates to the entire system, resulting in asymmetric twisted structures and fluid flows. These twisted systems are very similar to cholesteric liquid crystals, which we can find inside some television displays and mood rings. However, they have a very different origin. Our systems twist spontaneously due to their internal active energy.

Abstract

Active fluids are ubiquitous in nature, spanning both microscopic and macroscopic length scales. They belong to an interesting new class of nonequilibrium systems in physics. In contrast with externally driven materials, active fluids are intrinsically forced out of equilibrium by their constituent active particles, which consume energy from the environment, using it to engage in nonequilibrium activities, such as motility and replication. Two of the most prevalent examples of active particles are bacteria and actomyosin complexes. In both cases, we observe rich collective behaviour giving rise to, respectively, the multicellular organisation of bacterial colonies and the intracellular structure in eukaryotes.

A hydrodynamic description can be used to model the behaviour of active fluids. This approach is based on the fact that the active particles exert stresses on the surrounding fluid as they move through it. Within the hydrodynamic framework, we can study many interesting nonequilibrium phenomena, including hydrodynamic instabilities and spontaneous symmetry breaking. These provide an explanation for macroscopic motility patterns in active systems. In our work, we use a hybrid lattice Boltzmann method to simulate a range of motile states and their chiral characteristics.

We start by studying the dynamics of an active fluid enclosed in a droplet with imposed orientational anchoring at the interface. Our results show that when the anchoring is strong enough, active extensile and contractile stresses lead to spontaneous droplet rotation. In contrast, if the anchoring is weak, the droplet instead translates. The signature of the observed rotating states is a significant deformation of the droplet shape, distinguishing it from the rotation of spiral defects, which has been previously reported. Moreover, the sense of rotation is selected via spontaneous symmetry breaking, so that the droplet is equally likely to start rotating clockwise or anticlockwise, acquiring a random chirality.

Most biological active particles are also microscopically chiral themselves. Thus, active processes must involve chiral interactions at the microscale. We address this feature by considering a chiral active stress originating from a collection of active torque dipoles. We find that the active chiral stresses drive a nonequilibrium transition to a self-assembled cholesteric phase in both active fluids and dry active systems. This spontaneously twisted phase shares many of the characteristics of equilibrium cholesterics, including the formation of layered and fingering patterns, and the existence on non-singular defects. If the activity is sufficiently high, chiral active stresses are capable of untwisting an equilibrium cholesteric configuration (which is thermodynamically favoured).

Finally, we look at active fluids with both achiral (extensile, contractile) and chiral active stresses. We observe that contractile activity suppresses the spontaneous twist, while extensile activity enhances it. We also show the existence of a pitch-splay instability in these systems, leading to a bend deformation of cholesteric layers.

Declaration

I declare that this thesis was composed by myself, that the work contained herein is my own except where explicitly stated otherwise in the text, and that this work has not been submitted for any other degree or professional qualification except as specified.

Parts of this work have been published in [1].

(*Ana Regina Fialho, March 2020*)

Acknowledgements

First I would like to deeply thank my supervisor Davide Marenduzzo for his unfaltering kindness and support. Over the past few years, he has encouraged, advised, and motivated me on many academic and non-academic pursuits.

Thank you also to my collaborators, in particular Elsen Tjhung and Matthew Blow, whose work and ideas have contributed to this thesis.

Likewise, I would like to thank my colleagues in the Physics department and my officemates in 1511: Katy, Yair, Hanna, and Carolina. They were constant and reliable companions during my four years in the Physics building, and we have celebrated many significant milestones together. I am also profoundly grateful to Martina, she has been an exceptional colleague, but an even better flatmate, travel buddy, and all round friend, who has kept me grounded through all the ups and downs of life as a PhD student (and life in general).

A very warm thanks goes to all my friends and family for supporting me and still, after all these years, being interested enough to ask me about the topic of my research (even if they do not always listen or understand after). I would especially like to thank my parents for always supporting me and making me believe I can achieve anything (and everything).

Finally, I would like to acknowledge the CM-CDT for funding, and thank all of its members, as well as all the colleagues from the Soft Matter group in Edinburgh, for being such an amazing professional network, which has certainly helped me more than a few times.

Contents

List of Figures

List of Tables

Chapter 1

Introduction

1.1 What is active matter

All living matter is out of thermodynamic equilibrium. In biological systems, the detailed balance is typically broken by the release of chemical energy from the conversion of a nucleoside tri-phosphate molecule into its di-phosphate form (*i.e.* ATP $\rightarrow$ ADP). This energy can, in turn, be used to perform mechanical work, leading to motility and growth. Biological systems fall into the general definition of *active matter*: they are forced out of equilibrium as a result of internal processes, instead of external forces or gradients. This distinction is important in nonequilibrium physics and, as we shall see throughout this thesis, it leads to novel and intriguing physical phenomena.

In simple terms, active matter can be idealised as a collection of individual units - referred to as *active particles*. Each active particle is capable of absorbing energy from the surroundings (or from an internal fuel tank) and dissipate it to engage in a variety of nonequilibrium activities, including spontaneous movement, growth, and replication [2, 15, 16].

Active and driven systems are fundamentally distinct. In the latter, the constituent particles are passive and are driven out of equilibrium by an external field or gradient (*e.g.* an electric field, temperature, or chemical potential). What differentiates active matter is that the energy is locally input into the system

by the active particles themselves. Thus, even without external driving, active particle systems are intrinsically out of equilibrium. Furthermore, the particle movement is dictated internally and not imposed by external fields [2, 15].

In general, active particles are anisotropic. Therefore, active systems can exhibit macroscopic orientational order, similar to equilibrium polar or nematic liquid crystals [17]. When in an aligned phase, the particles can "communicate" via the propagation of orientational deformations. As a result, we can observe remarkable collective behaviour, much richer than that of their passive counterparts or other nonequilibrium driven systems. Examples include flocking [6], giant density fluctuations [18], mechanical instabilities [4], spontaneously flowing states[19, 20], and turbulence at low Reynolds number [21, 22].

Active systems can be further classified in two groups: dry active systems and active fluids. Swimming microorganisms, such as bacteria and algae, are an example of active fluids because the swimmers are suspended in a passive solvent. Another example is provided by vibrated granular rods [18]. In this case, even though there is no solvent, the rods collectively behave as a fluid with some effective viscosity. The main distinction is that active fluids must satisfy momentum conservation, while dry systems do not. For instance, a flock of birds [1], in which the direction of flying can change suddenly, is a dry active system.

In this thesis we mostly focus on the study of active fluids and their hydrodynamics. This is the most relevant class for the understanding of microbiology, and provides valuable insights into the mechanics of living matter.

1.2 Biological examples of active systems

Instances of biological activity can be found at all length scales in nature, and serve as inspiration for the study of active matter. Biological active particles can be macroscopic, like the fish in a shoal [23] and the birds flying in a flock[1]; or microscopic such as swimming bacteria [24] and cytoskeletal organelles inside the cell [25]. In the sections below, we shall discuss some of the most explored examples, highlighting their active characteristics and unusual physical behaviour.

1.2.1 Bird flocks and fish shoals

The flocking of birds is a natural realisation of emergent collective behaviour [26], where interactions between self-propelled individuals produce large-scale coherent patterns (see Fig. 1.1 (a)). Even though each of the birds is an active particle with its own position and velocity, the flock is, strikingly, able to select and update the collective flight direction [1]. In a following section, we will introduce a simple theoretical model, formulated by Vicsek *et al.* [6], that reproduces flocking phenomena from particle interactions. Curiously, recent numerical studies of the flock's interaction network have shown that the interactions depend on a topological, rather than metric, distance [27]. Thus, at each instant, a bird appears to be comparing its position and velocity to those of only $5-7$ topological neighbours, instead of all the other birds within a given distance. The authors argue that a topological interaction is indispensable to maintain the flock's cohesion against the large density changes caused by external perturbations, typically predation.

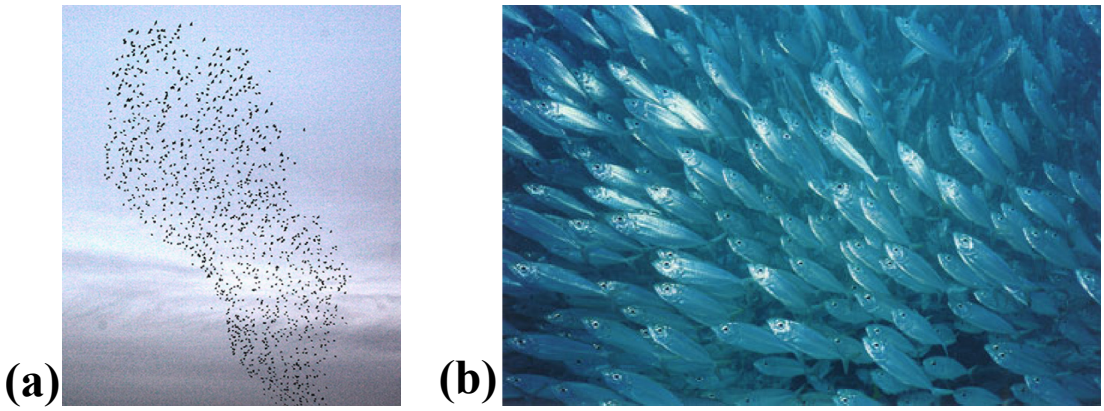

Figure 1.1 *(a) Snapshot of a bird flocking event. Image reproduced from [1]. (b) A shoal of fish illustrating the tendency towards parallel alignment while swimming. Image reproduced from [2].*

Another example of collective dynamics in the animal world, this time in a fluid, is the case of fish shoals. In a shoal, the fish tend to align parallel to each other while swimming (see Fig. 1.1 (b)). Studies of large-scale shoals [23] have revealed a relatively rapid time-scale for reorganization. Also, evidence was found of "fish waves" that occur at regular intervals and propagate internal disturbances within the system. These disturbances have scales far larger than that of individual fish and are also transmitted at much higher wave speeds.

1.2.2 Bacterial suspensions

In nature, bacteria are often found in organised populations. Bacterial structures are among the simplest examples of self-assembly in living organisms. They grow in different shaped structures, predominantly as films, chains, mats and colonies [28]. These multicellular patterns [24] can confer many biological advantages to bacteria, such as increased antibiotic resistance and resilience to environmental changes [29].

A bacterial suspension can be experimentally studied in the laboratory and constitutes a canonical active fluid example. Bacteria are self-propelled particles with a swimming motion which is typically driven by the rotation of a flagella bundle [30]. In dense suspensions or within semi-solid media such as agar, where swimming is hindered by crowding, or impossible, bacterial activity can also arise from growth and replication. Structurally, bacteria are often elongated or rod-shaped [31], with polar direction defined by the swimming velocity.

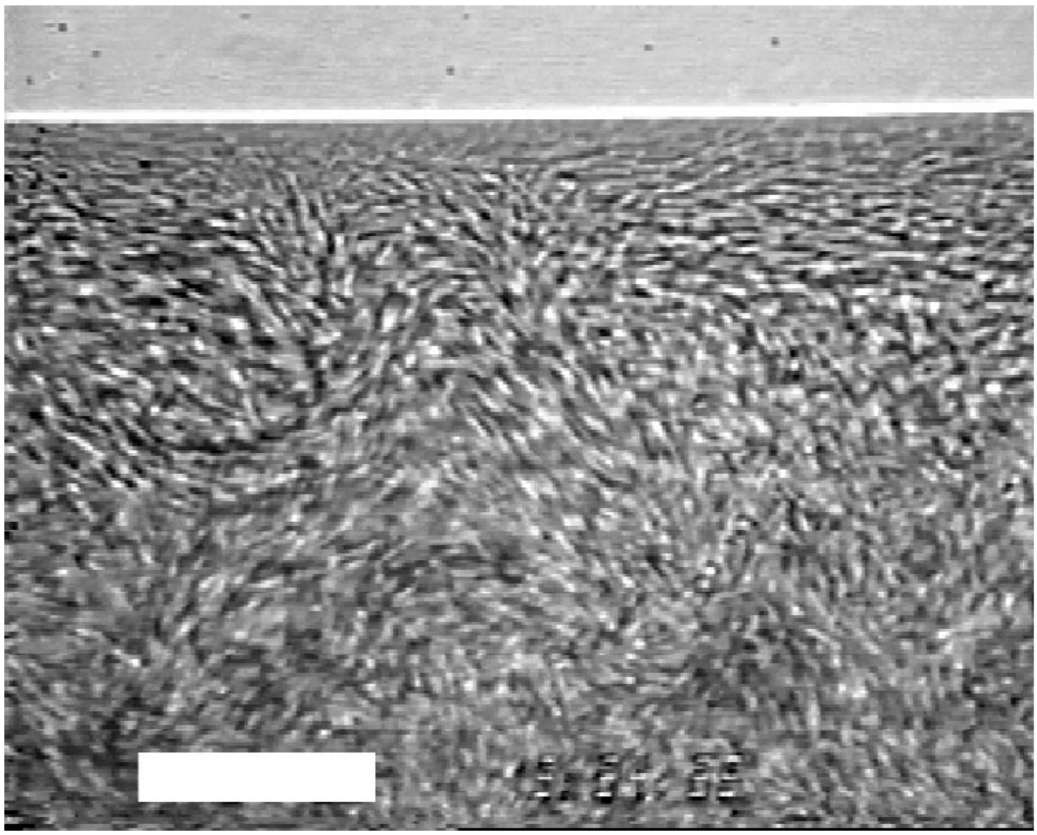

Figure 1.2 *Bacterial "turbulence" at zero Reynolds number in a sessile drop of Bacillus subtilis, viewed from below. The scale is* $35\mu m$*. Figure reproduced from [3].*

At high concentrations, bacterial suspensions display collective behaviour typical of aligning systems, such as pattern formation [28] and turbulence [21] (see Fig. 1.2). The process by which bacteria acquire macroscopic polar order can be seen as two-fold[32]. First, excluded volume interactions cause the organisms to align with with each other. This results in an equilibrium-like transition into a nematically ordered state, which takes place for increasing density. The bacterial nematic state is unstable to self-propulsion. As the swimming speed of the bacteria is increased, there is a phase separation into domains of bacteria with the same polarity, *i.e.* swimming in the same direction. Because it is driven by active swimming, the phase transition from nematic to polar order is a nonequilibrium one.

1.2.3 Actomyosin inside eukaryotic cells

The bulk of an eukaryotic cell is mostly made up of a complex network of protein filaments, microtubules, and molecular motors, called the cytoskeleton. The cytoskeleton network provides the mechanical rigidity necessary for cell movement, such as cell crawling and muscle contraction. It also plays a pivotal role in the transport of organelles across the cytoplasm and the segregation of chromosomes during cell division. In line with the other examples of active fluids, the cytoskeleton can exhibit complex pattern formation, yielding a variety of structures which include arrangements of asters, vortices, and spirals [25, 33, 34].

Among the cytoskeleton components, actomyosin is believed to play an important role in cell motility [35]. Actomyosin is actually an active structure [36] made of protein filaments (actin), which are cross-linked by motor proteins (myosin), and immersed in a fluid solvent. This mixture is described as an "active gel" because it involves two active processes. Firstly, an actin filament can grow or polymerise at one of its ends and shrink or depolymerise at the other (see Fig. 1.3 (a)). Thus, the filaments are polar: they have a plus (growing) and a minus (shrinking) end. Secondly, they can attach to myosin motors which "walk" towards the positive ends. If the myosin attaches to a pair of filaments with the same orientation, it will simply slide through them. However, if the filaments are antiparallel, then the motor pulls them together, causing contraction (see Fig. 1.3 (b)).

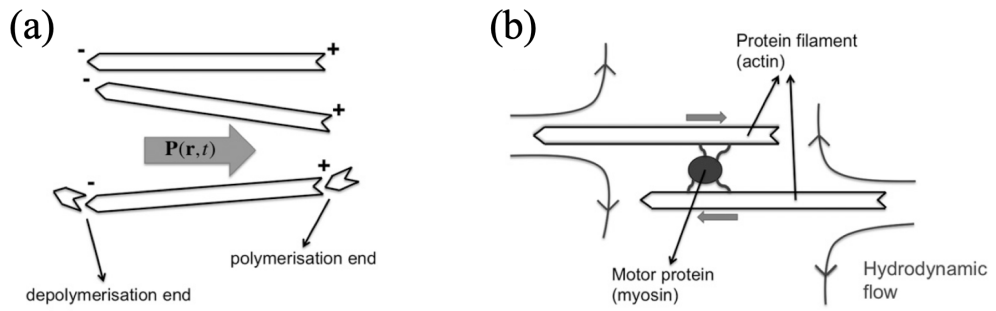

Figure 1.3 *Schematic representation of active processes in actomyosin. (a) Polymerization (+ end) and depolymerisation (− end) of the actin filaments. (b) A myosin motor pulling two actin filaments together. This is a contraction movement and induces hydrodynamic flows around the actomyosin complex. Figure reproduced from [4].*

1.3 The physics of active matter

1.3.1 Run-and-tumble bacteria as hot colloids

Freely swimming bacteria, such as *E. coli* during chemotaxis, move in a fluid via a characteristic run-and-tumble dynamics (see Fig. 1.4). Essentially, the movement involves a series of roughly straight-line "runs" punctuated by rapid changes of direction, or "tumbles" [37]. This is a consequence of the helical beating of their flagella. When the flagella rotate synchronously counterclockwise, the bacteria swim in a direction that is basically straight (run). The motors responsible for rotating the flagella can also suddenly change direction due to stochastic intracellular events. Thus, one or more filaments start rotating clockwise, and the organism tumbles, changing its direction [38]. The tumble is of short duration and can be considered instantaneous in comparison to a run. This run-and-tumble dynamics can, in idealized form, serve as a paradigm for non-Brownian diffusive motion and it can be used to explore some central concerns of non-equilibrium dynamics.

Let us assume that during a run, of variable duration τ, the bacteria move in a fixed direction with velocity v. Tumbles occur randomly and instantaneously at rate α so that $\langle \tau \rangle = \frac{1}{\alpha}$. It can be shown that in free space such run-and-tumble organisms obey the diffusion equation at long time and length scales.

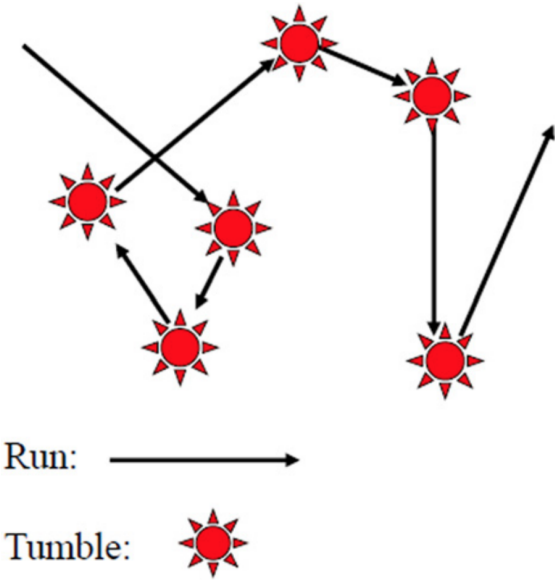

Figure 1.4 *Schematized representation of run-and-tumble dynamics in E.coli. Figure from [5].*

The corresponding diffusivity is calculated to be [37]

$$D_{bacteria} = \frac{v^2}{\alpha\ d}\ , \tag{1.1}$$

where d is the dimensionality of the space.

It is useful to compare this diffusivity with the one obtained for a dilute solution of colloids, which is a system in thermodynamic equilibrium. For colloidal particles, the diffusion constant D is given by the Stokes-Einstein formula (which is a consequence of the fluctuation-dissipation theorem [39])

$$D = \frac{k_B T}{3\pi\eta l}\ . \tag{1.2}$$

k_B is the Boltzmann constant, T is the temperature, η is the fluid viscosity and l is the colloidal diameter. Bacteria such as *E. coli* are around $1\mu m$ in size and swim at a speed $\sim 20\mu s^{-1}$. By entering the relevant numbers for the run-and-tumble bacteria, we find that the diffusion constant $D_{bacteria}$ is hundreds of times larger than what would be predicted by stokes law (1.1). This is because the fluctuation-dissipation theorem only holds for systems close to thermodynamical equilibrium, which bacteria are not. Bacteria are then said to behave as "hot colloids" because their diffusivity can be approximated by that of a colloidal

suspension, only with an effective temperature which is $\sim 10^2$ times higher than the actual temperature of the system, $T_{eff} \sim 10^2\ T_{real}$ [37, 40].

$$D_{bacteria} = D\ \frac{T_{eff}}{T_{real}} \sim 10^2 D\ . \tag{1.3}$$

1.3.2 The Vicsek model: flocking and giant number fluctuations

Active particles, besides being able to self-propel, also have a tendency to align with each other. The Vicsek model [6, 41] provides a simple prototypical way of addressing the ordering observed in such active systems.

In the original Vicsek model, the particles move in two dimensions, following a defined set of rules. Each particle is a point-like entity with position $\mathbf{r}_i(t)$ and angular orientation $\theta_i(t)\ \epsilon\ [-\pi, \pi]$. The swimming speed is taken to be v_0. At every time-step, the particles rotate their orientation in order to align with the average velocities of their neighbours.

$$\theta_i\left(t + \Delta t\right) = \left\langle \theta_i \right\rangle_r + \Delta\theta_i \tag{1.4}$$

The angle brackets $\langle\cdot\rangle_r$ denote the average of orientations, calculated in a circle of radius r and centered at $\mathbf{r}_i$ (particle i is normally included in the average as well). The term $\Delta\theta$ represents the addition of some random noise. The noise is a random number chosen uniformly from the interval $[-\eta, \eta],\ \ \eta\ \epsilon\ [0, \pi]$. The noise strength is, therefore, controlled by the parameter η.

After re-orienting, the particle takes a step with velocity

$$\mathbf{v}_i = v_0\left(\cos\left(\theta_i\left(t + \Delta t\right)\right), \sin\left(\theta_i\left(t + \Delta t\right)\right)\right)\ , \tag{1.5}$$

so that the position at time $t + \Delta t$ is

$$\mathbf{r}_i\left(t + \Delta t\right) = \mathbf{r}_i\left(t\right) + \mathbf{v}_i\left(t + \Delta t\right)\Delta t\ . \tag{1.6}$$

The Vicsek family of models displays a well defined phase transition from an isotropic state to a coherently ordered flock, which can be observed when the

noise decreases or the number density increases [6, 42, 43].

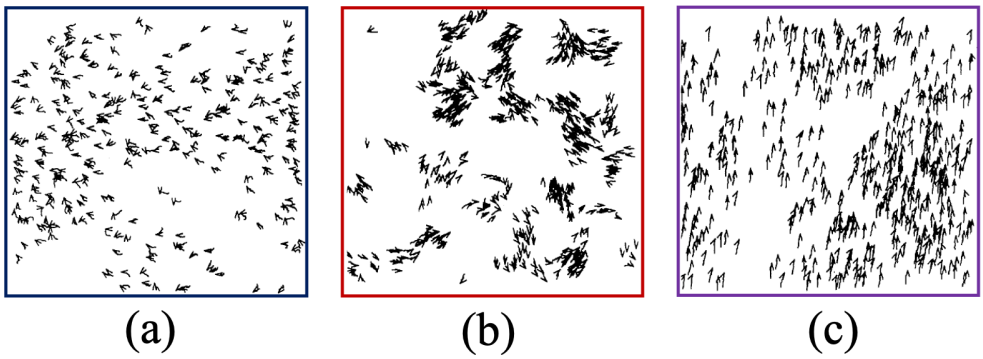

Figure 1.5 *Flocking transition in Vicsek particles. (a) For large noise the particles swim independently in a disordered phase. (b) Near the transition, the particles form groups that move coherently. (c) Macroscopically ordered phase, observed for small noise and high density. Figure from [6]*

For large η (or small densities), noise prevails, and particles move independently, without any particular order (Fig. 1.5 (a)). On the other hand, if the noise is small (or the density is high), particles tend to align to each other, driving the whole system into an ordered flocking state (Fig. 1.5 (c)). The transition is discontinuous and, near criticality, we observe a coexistence between the two phases where the particles form small groups that move coherently in random directions (Fig. 1.5 (b))

Unlike XY spins, nonequilibrium flocking models do not respect the Mermin–Wagner theorem and exhibit true long-range order even in two dimensions. This is because the particles are motile and, therefore have an extended range of influence on their neighbours, ultimately leading to the suppression of large scale fluctuations of the orientation.

Finally, in a flock, we can also encounter giant number fluctuations [18]. For a system in thermodynamic equilibrium with a reservoir, number density fluctuations are expected to go down with the system size as $\frac{\Delta N}{N} \sim \frac{1}{\sqrt{N}}$, with N being the total number of particles. This is a consequence of the central limit theorem. However, in active systems the particles can cluster together, increasing the number density to obtain $\frac{\Delta N}{N} \sim N^{\alpha}$, with $\frac{1}{2} < \alpha < 1$. The microscopical reason behind this phenomenon is the coupling of density fluctuations to the alignment of the individuals.

1.3.3 The individual swimmer

The simplest realisation of an active particle swimming in a fluid is a permanent force dipole [16]. This can be understood by applying Newton's third law to the particle's motion. In order to move, the active particle exerts forces on the surrounding fluid, which responds by exerting an equal and opposite force on the particle. Thus, the net force on the "swimmer" is zero (note that there are no external forces). The lowest order force distribution that this neutrally buoyant particle can exert on its surrounding fluid is a force dipole [16]. The direction of the dipole defines the particle's orientation and often coincides with its long axis.

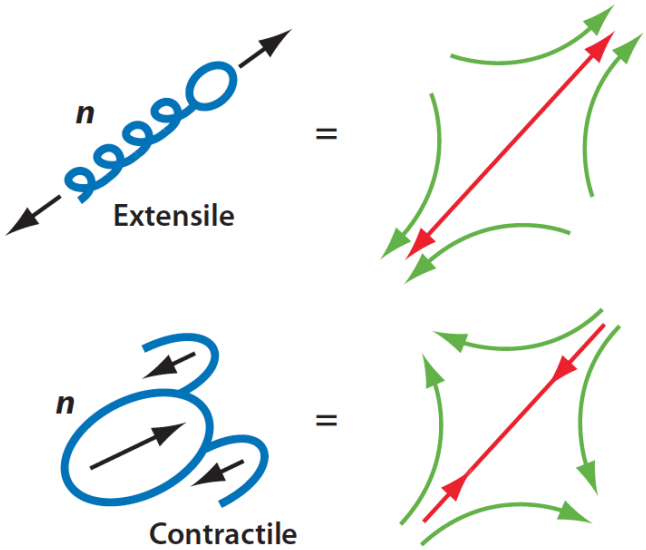

Figure 1.6 *Quadupolar flows around a swimming bacterium (top) and an algal cell (bottom). The dipolar direction and forces are represented in red, and the fluid flow in green. Bacteria are extensile, and algae contractile, force dipoles. Figure taken from [7].*

Depending on the character of the swimmer, we can distinguish between extensile and contractile particles [31]. Extensile particles, also called pushers, push the fluid out along their long axis and pull the fluid along their mid-points. The fluid flow generated can be seen in Fig. 1.6 (top). Inversely, contractile swimmers (or pullers) pull the fluid along the dipolar direction and push it out perpendicularly at the mid-point (see Fig. 1.6 (bottom)).

E. coli, and other bacteria that swim using flagella at their rear, are extensile movers (see Fig. 1.6 (top)). The quadrupolar fluid flow around a single bacterium has been measured experimentally [8] and is shown in Fig. 1.7. The flow is observed to be long-range, decaying as $\sim \frac{1}{r^2}$. Thus, the flow generated by a

bacterium, can affect the motion of other bacteria swimming a distance r away from it, through a long-range hydrodynamic interaction. Algea, and bacteria that swim with strokes of frontal flagella, are contractile (see Fig. 1.6 (bottom)). Actomyosin also moves through contractile forces, as we have described before.

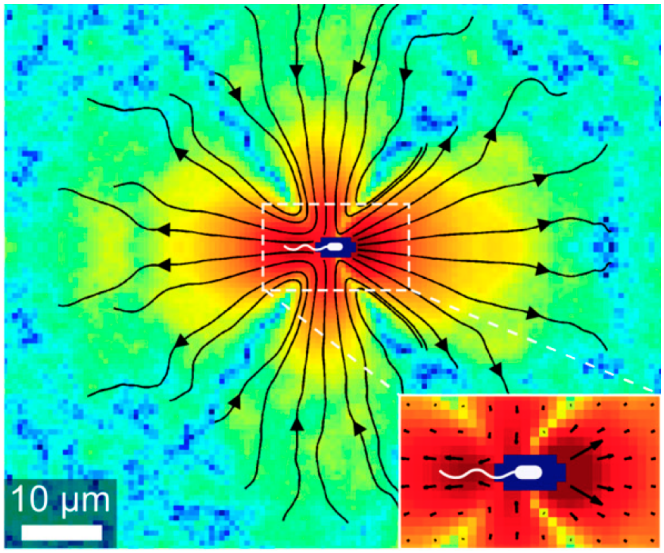

Figure 1.7 *Experimentally measured flow field around an E.coli bacterium. Figure from [8].*

Active particle suspensions of extensile or contractile swimmers also have interesting rheology. In particular, they can increase or decrease the viscosity of the fluid. Figure 1.8 shows a pictorial representation of the mechanism behind this phenomenon. Let us consider a collection of active particles under an applied shear. The particles are elongated and tend to align with the fluid flow (here, we are considering the flow aligning regime). If the particles are extensile, then the forces exerted are along the shear direction. On the other hand, if the particles are extensile, then the active forces oppose the flow. This is equivalent to saying that extensile particles decrease the effective viscosity of the fluid, while contractile particles increase it.

1.4 Thesis Outline

In this thesis, we present a computational study of hydrodynamic instabilities in active fluid systems.

Chapters 2 and 3 provide the theoretical background for our approach. In chapter 2, we introduce the phenomenological equations to describe the dynamics of

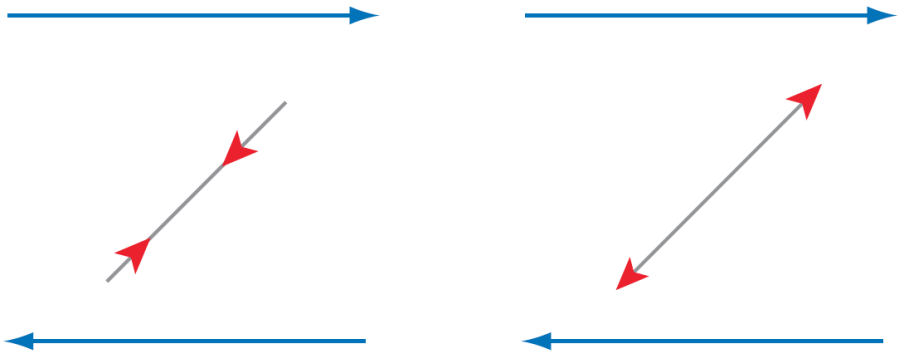

Figure 1.8 *Schematic representation of how activity modifies viscosity. Shear orients the filaments; the permanent force dipoles pull back, if contractile, and push out, if extensile, on the flow. Figure taken from [7].*

active fluids at large time and length scales. We also derive the active stress term from the microscopic force distribution, and demonstrate the emergence of generic instabilities in the hydrodynamic model. Chapter 3 consists of a brief overview of the hybrid Lattice Boltzmann method, which we use for computational simulations.

In chapter 4, we focus on the study of an active gel droplet on which we impose strong anchoring at the interface. We find that under strong anchoring conditions the droplet spontaneously starts to rotate due to activity. We characterise the nonequilibrium transition to rotational states in both extensile and contractile droplets. We further investigate the importance of surface tension and interfacial anchoring to the observed states. Our results show that without anchoring the droplets become self-motile instead of chiral. Surface tension is also important as it allows the droplet to acquire a "bean" or "S" shape, distinguishing our results from the previously reported rotation of circular asters and vortices.

Chapter 5 is dedicated to the study of active chiral fluids. We start by introducing the torque dipole approximation for chiral active particles and deriving the chiral contribution to the active stress. We then show, by a combination of linear stability analysis and computational results, that the chiral active stresses lead to the self-assembly of a nonequilibrum cholesteric where the particle orientation twists spontaneously. Finally, we present simulations to highlight the similarities in between the actively self-assembled cholesteric phase and its equilibrium counterpart. Namely, we present layered and fingering structures, and the nucleation of non-singular defects, which are motile.

We conclude, in chapter 6, by looking at the interaction between chiral stresses and (i) thermodynamic chirality (*i.e*, equilibrium cholesterics); (ii) achiral contractile and extensile stresses. We show that active chirality is able to change the pitch of an equilibrium cholesteric, by adding or removing layers. Moreover, we see that the chiral active stress is able to fully untwist the cholesteric, returning it to a purely aligned state. The non-equilibrium cholesteric phase is suppressed by contractile stresses and enhanced by extensile ones. We also show that there is a pitch-splay instability in quasi-2D systems with extensile and chiral active stresses, leading to the formation of nonequilibrium undulating cholesteric layers.

Chapter 2

The hydrodynamic model

In this thesis, we choose the hydrodynamic approach to model the properties of active matter. With such a theoretical framework, we can describe the large-scale, long-time behaviour of the system using only a small number of continuum fields. The evolution of those fields follows a set of hydrodynamic equations that we shall introduce in the following sections. We will also use this model to demonstrate the existence of the so called generic instabilities, which appear as a consequence of activity and are relevant to interpret the motility patterns found in our results.

2.1 Hydrodynamic fields

Let us begin by describing the system of active particles, focussing on the individual swimmers. We consider a collection of N self-propelled particles with centres of mass located at the positions $\{\mathbf{r}_1, \mathbf{r}_2, ..., \mathbf{r}_N\}$. We take these particles to be polar objects with orientation given by the unit vectors $\{\hat{\nu}_1, \hat{\nu}_2, ..., \hat{\nu}_N\}$. We also assume that the particles swim in the direction of $\hat{\nu}_i$ with speed v, so that $v_i = v\hat{\nu}_i$.

In principle, we could model the dynamics of the active particles microscopically. To do so, we would need to solve the equations that describe the position and velocity of each of the N particles. These equations must take into account the tendency of the particles to align with each other, like in the Vicsek model [6]. In addition to the particle velocities, it is also necessary to solve for the fluid velocity $\mathbf{u}$, in order to include hydrodynamic interactions. The result is a set

of $6N$ equations for the variables $\{(\mathbf{r}_1, \hat{\nu}_1), (\mathbf{r}_2, \hat{\nu}_2), ..., (\mathbf{r}_N, \hat{\nu}_N)\}$ that describe each of the individual swimmers in three-dimensions and are coupled to the fluid velocity $\mathbf{u}$.

Instead, we take the hydrodynamic (continuum) limit. This is a simpler and less costly approach that yields good results in the description of large scale collective phenomena [4, 19, 32, 44, 45]. Following the hydrodynamic method, we use coarse-graining to find a set of continuous fields, each a function of time t and position $\mathbf{r}$, which allow the exploration of much larger lengthscales.

The hydrodynamic description is effectively a macroscopic theory. It looks at the system at length and time scales much larger than those of the molecular processes. At these scales, we can use phenomenological parameters to capture the physics of the systems, without having to consider the precise microscopic mechanisms of energy transduction [45].

The hydrodynamic fields chosen to describe such a system are: the local concentration of active particles $\phi(\mathbf{r}, t)$

$$\phi(\mathbf{r}, t) = \left\langle \sum_{i=1}^{N} \delta(\mathbf{r} - \mathbf{r}_i(t)) \right\rangle \ ; \tag{2.1}$$

their average polar orientation, or polarisation, $\mathbf{p}(\mathbf{r}, t)$

$$\mathbf{p}(\mathbf{r}, t) = \frac{1}{\phi(\mathbf{r}, t)} \left\langle \sum_{i=1}^{N} \hat{\nu}_i(t) \delta(\mathbf{r} - \mathbf{r}_i(t)) \right\rangle \ ; \tag{2.2}$$

and the average velocity $\mathbf{u}(\mathbf{r}, t)$ of the solvent. In this thesis we will study a system of "shakers", *i.e.* particles that are active but do not self-propel. Since "shakers" have swimming speed $v = 0$, they move with the velocity of the solvent $v_{particle} = \mathbf{u} + v\mathbf{p} = \mathbf{u}$.

The angle brackets in Eqs. (2.1) and (2.2) denote local averages, so that the concentration and polarisation are simply mesoscopic averages of the particles' positions and orientations, respectively.

The continuum fields just defined evolve according to a set of hydrodynamic equations. These equations can be derived directly from the microscopic dynamics [31], but here we choose to write them phenomenologically based on

the conservation laws and broken symmetries of the system [16, 32].

2.2 Hydrodynamic Equations

Free energy

We start by describing the system's behaviour in the near-equilibrium, or passive, limit. Because the active particles have an elongated shape, excluded volume interactions cause them to align in a liquid crystalline way. Thus, the particles tend to form an aligned polar phase, minimising the free energy

$$\mathcal{F}(\phi, \mathbf{p}) = \int f(\mathbf{r})\, d\mathbf{r} \ , \tag{2.3}$$

with free energy density

$$\begin{aligned} f(\mathbf{r}, \phi, \mathbf{p}) &= V(\phi, \nabla\phi) + f_{bulk} + f_{elastic} \\ &= V(\phi, \nabla\phi) + \left[-\frac{A}{2}\frac{(\phi - \phi_{cr})}{\phi_{cr}}|\mathbf{p}|^2 + \frac{A}{4}|\mathbf{p}|^4 \right]_{bulk} + \left[\frac{K}{2}(\nabla\mathbf{p})^2 \right]_{elastic} . \end{aligned} \tag{2.4}$$

There are three different contributions to the free energy density. The first one is a potential V, depending on the concentration ϕ and its gradients. This potential allows us to include multi phase fluids. We introduce the explicit form of V in Chapter 4, where we use a binary fluid approach to generate active gel droplets. The second term is a bulk contribution. It includes the Landau terms proportional to $|\mathbf{p}|^2$ and $|\mathbf{p}|^4$ which describe the transition to the polar phase for a critical concentration ϕ_{cr} [46]. The constant A controls the magnitude of order, $A > 0$ ensures that the energy is bounded from below and the equilibrium state corresponds to polar alignment. The third and final term, $\frac{K}{2}(\nabla\mathbf{p})^2$, is a free energy penalisation for elastic distortions of the alignment (splay, bend and twist). Here, we use the generic single elastic constant approximation: $K_{splay} = K_{bend} = K_{twist} = K$ [17]. This elastic contribution is valid for non-chiral liquid crystals. In chapter 6 we will introduce the cholesteric term.

The free energy describes the thermodynamic characteristics of the polar active fluid and must be complemented by the equations of motion for ϕ, $\mathbf{p}$, and $\mathbf{u}$.

Concentration

Assuming conservation of the number of active particles, the concentration ϕ follows the convective diffusion equation

$$\frac{D\phi}{Dt} = M\nabla^2\mu \ . \tag{2.5}$$

Here, $\frac{D}{Dt} = \frac{\partial}{\partial t} + \mathbf{u}\cdot\nabla$ is the material derivative including the convection of the particles by the fluid velocity. The right hand side of Eq. (2.5) describes the passive diffusive current from regions of high chemical potential to regions of low chemical potential. The chemical potential μ can be derived from the free energy as $\mu = \frac{\delta\mathcal{F}}{\partial\phi}$, and M represents the mobility parameter associated with it.

If the particles are self-motile with velocity $v\mathbf{p}$ relative to the solvent, then the material derivative must include a self-advection term $v\mathbf{p}\cdot\nabla$. This is the first active contribution in the model. In our simulations, we have turned off self-advection and considered only active stresses on the fluid.

Polarisation

The dynamics of the polarisation field $\mathbf{p}$ follows from polar liquid crystal theory [17, 47] and can be written as

$$\frac{D\mathbf{p}}{Dt} = -\frac{1}{\Gamma}\mathbf{h} - \underline{\underline{\Omega}}\mathbf{p} + \xi\underline{\underline{\nu}}\mathbf{p} \ . \tag{2.6}$$

Here, Γ is the rotational viscosity and $\mathbf{h}$ the molecular field $\mathbf{h} = \frac{\delta F}{\delta \mathbf{p}}$. $\underline{\underline{\nu}}$ and $\underline{\underline{\Omega}}$ are, respectively, the symmetric and anti-symmetric parts of the velocity gradient tensor ∇u

$$\underline{\underline{\nu}} = \frac{\nabla\mathbf{u} + (\nabla\mathbf{u})^T}{2} \ , \tag{2.7}$$

$$\underline{\underline{\Omega}} = \frac{\nabla\mathbf{u} - (\nabla\mathbf{u})^T}{2} \ . \tag{2.8}$$

The parameter ξ is a shape factor related to the geometry of the active particles:

$\xi > 0$ for rod-like particles and $\xi < 0$ for disk-like particles. ξ also determines whether the particles tend to align to a shear flow ($|\xi| > 1$), or tumble ($|\xi| < 1$). Equation (2.6) addresses the fact that the elongated molecules can be rotated by gradients of the velocity field. This is the first of two major differences between the hydrodynamics of liquid crystals and that of simple fluids [48]. The second difference, which we will see below, is that liquid crystals exhibit both a viscous and an elastic response to external stress. This is due to the complexity of their free energy.

Fluid velocity: Navier-Stokes

Momentum balance in the system is enforced through the Navier-Stokes equation.

$$\rho \frac{D\mathbf{u}}{Dt} = -\nabla P + \nabla \cdot \underline{\underline{\sigma}}^{total} - \gamma \mathbf{u} \tag{2.9}$$

The fluid is also assumed to be incompressible, so that

$$\nabla \cdot \mathbf{u} = 0 \ . \tag{2.10}$$

In Eq.(2.9), ρ is the constant density of the fluid, P is the isotropic pressure and $-\gamma \mathbf{u}$ the frictional force. The total hydrodynamic stress $\underline{\underline{\sigma}}^{total}$ includes contributions from the viscosity and elasticity of the medium, as well as an active term.

$$\underline{\underline{\sigma}}^{total} = \underline{\underline{\sigma}}^{viscous} + \underline{\underline{\sigma}}^{elastic} + \underline{\underline{\sigma}}^{active} \tag{2.11}$$

The three stress contributions are as follows. The viscous stress is given by

$$\sigma^{viscous}_{\alpha\beta} = \eta \left(\partial_\alpha u_\beta + \partial_\beta u_\alpha \right) , \tag{2.12}$$

where η is the shear viscosity and the Greek indices indicate cartesian coordinates. Greek index summation rule will be used throughout this thesis.

The elastic stress arises from liquid crystal dynamics and is equal to

$$\sigma_{\alpha\beta}^{elastic} = \frac{1}{2}\left(p_\alpha h_\beta - p_\beta h_\alpha\right) - \frac{\xi}{2}\left(p_\alpha h_\beta + p_\beta h_\alpha\right) - K\partial_\alpha p_\gamma \partial_\beta p_\gamma \ . \tag{2.13}$$

The final contribution is the active stress (which we derive in section 2.3 below) and has the form

$$\sigma_{\alpha\beta}^{active} = -\zeta\ \phi\ p_\alpha p_\beta \ . \tag{2.14}$$

2.3 Active Stress

We will now proceed by deriving the stress exerted on the fluid by a suspension of active particles. We consider, as seen in chapter 1, that the active particles push or pull the fluid around them with a dipolar force distribution. As a reminder, the force dipole is the simplest force distribution for swimming particles that are neutrally buoyant. In most cases of biological swimmers, *e.g.* bacteria and actomyosin, the direction of the torque dipole coincides with the orientation of the particle.

Let us take an active particle i, of length l and orientation $\hat{\nu}_i$. We assume that the particle is an effective force dipole with dipolar force strength F and has an homogeneous mass distribution so that the centre of mass is located at the midpoint $\frac{l}{2}$. Figure 2.1 shows a representation of such a particle for the case of extensile (a), and contractile (b) forces.

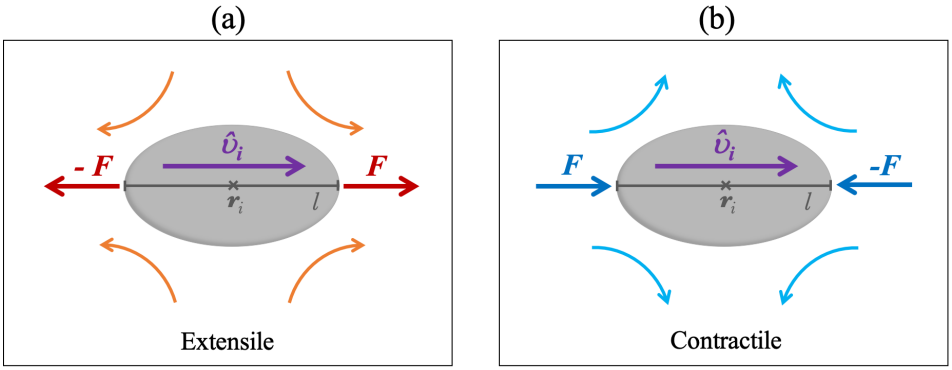

Figure 2.1 *(a) Extensile and (b) contractile active particles.*

The force density exerted on the fluid by 1 of these particles is

$$\mathbf{f}_i(\mathbf{r}) = \pm\left[F\hat{\nu}_i\delta\left(\mathbf{r}-\mathbf{r}_i-\frac{l}{2}\hat{\nu}_i\right) - F\hat{\nu}_i\delta\left(\mathbf{r}-\mathbf{r}_i+\frac{l}{2}\hat{\nu}_i\right)\right] \tag{2.15}$$

In Eq. 2.15, the + sign applies to extensile particles and the − sign to contractile ones (see Fig. 2.1). For the remainder of this derivation, we shall focus on the extensile case (the − sign will be recovered at the end for contractile particles)

By summing over the N particles, we obtain the total active force acting on the fluid

$$\mathbf{f}^{active}(\mathbf{r}) = \sum_{i=1}^{N} F\hat{\nu}_i\delta\left(\mathbf{r}-\mathbf{r}_i-\frac{l}{2}\hat{\nu}_i\right) - F\hat{\nu}_i\delta\left(\mathbf{r}-\mathbf{r}_i+\frac{l}{2}\hat{\nu}_i\right) \ . \tag{2.16}$$

We can now Taylor expand the delta function

$$\delta\left(\mathbf{r}-\mathbf{r}_i\pm\frac{l}{2}\hat{\nu}_i\right) = \delta(\mathbf{r}-\mathbf{r}_i) \pm \frac{l}{2}\hat{\nu}_i\cdot\nabla\delta(\mathbf{r}-\mathbf{r}_i) + O\left(l^2\nabla^2\right) \ , \tag{2.17}$$

in order to obtain (in cartesian coordinates)

$$\mathbf{f}_\alpha^{active}(\mathbf{r}) = -F\ l\ \partial_\beta \sum_{i=1}^{N} \hat{\nu}_{i,\alpha}\hat{\nu}_{i,\beta}\delta(\mathbf{r}-\mathbf{r}_i) \ . \tag{2.18}$$

Since we want to describe the system in terms of the hydrodynamic fields, we add a coarse graining step by performing the local average:

$$\mathbf{f}_\alpha^{active}(\mathbf{r}) = -Fl\partial_\beta\left\langle \sum_{i=1}^{N} \hat{\nu}_{i,\alpha}\hat{\nu}_{i,\beta}\delta(\mathbf{r}-\mathbf{r}_i)\right\rangle \ , \tag{2.19}$$

and find

$$\mathbf{f}_\alpha^{active}(\mathbf{r}) = -F\ l\ \partial_\beta(\phi\ p_\alpha p_\beta) \, . \tag{2.20}$$

Finally, we note that the force can be written as the gradient of the active stress,

which takes the form:

$$\sigma_{\alpha\beta}^{active} = -\zeta\ \phi\ p_\alpha p_\beta\ , \tag{2.21}$$

with $\zeta = Fl$. [16]. ζ is the activity parameter and it is proportional to the force dipole. $\zeta > 0$ corresponds to extensile stresses and $\zeta < 0$ to contractile ones.

2.4 Generic instabilities

One of the key predictions of the hydrodynamic theory for active fluids is the existence of instabilities in the orientational field, that lead to spontaneously flowing steady states [19, 49]. In this section, we will demonstrate this instability by following the linear stability calculations of [19, 32].

We start by considering a quasi-1D active fluid. This means that $\mathbf{p}$ and $\mathbf{u}$ are three dimensional but depend only on one of the coordinates, that we take to be z. The system is uniform with $\phi = constant$. We also consider that the fluid is confined between two walls, located at $z = 0$ and $z = L$. At the walls, we have no-slip boundary conditions for the fluid $\mathbf{u}(z = 0, t) = \mathbf{u}(z = L, t) = 0$ and $\frac{\partial p}{\partial z}|_{z=0} = \frac{\partial p}{\partial z}|_{z=L} = 0$ for the polarisation.

With this setup, the hydrodynamic equations (2.6), (2.9) and (2.10) describing the active fluid become

$$\frac{\partial p}{\partial t} + \mathbf{u}\cdot\nabla\mathbf{p} = -\underline{\underline{\Omega}}\cdot\mathbf{p} + \xi\underline{\underline{\nu}}\cdot\mathbf{p} + \frac{\mathbf{h}}{\Gamma} \tag{2.22}$$

$$-\nabla P + \eta\nabla^2\mathbf{u} + \nabla\cdot\underline{\underline{\sigma}} = 0 \tag{2.23}$$

$$\nabla\cdot\mathbf{u} = 0 \tag{2.24}$$

Note that we have neglected the inertial term in the Navier-Stokes equation (2.9). This is because the Reynolds number for active particles, such as bacteria, is typically very low and of the order of 10^{-5} (Stokes limit). We will also assume that $\xi > 0, |\xi| > 1$, as is the case for elongated, flow aligning particles (see Fig. 2.1).

The set of equations (2.22)-(2.24) above has an aligned steady state solution,

where the particles are static and have their orientations along y.

$$\mathbf{p}_0 = (0, 1, 0) \tag{2.25}$$

$$\mathbf{u}_0 = (0, 0, 0) \tag{2.26}$$

We investigate the stability of the rest state by adding a small perturbation:

$$\mathbf{p}(z,t) = \mathbf{p}_0 + \delta\mathbf{p}(z,t) = \begin{pmatrix} \delta p_x(z,t) \\ 1 \\ \delta p_z(z,t) \end{pmatrix}, \tag{2.27}$$

$$\mathbf{u}(z,t) = \mathbf{u}_0 + \delta\mathbf{p}(z,t) = \begin{pmatrix} \delta u_x(z,t) \\ \delta u_y(z,t) \\ 0 \end{pmatrix}. \tag{2.28}$$

Because of the conditions $|\mathbf{p}| = 1$ and $\nabla \cdot \mathbf{u} = 0$ (incompressibility), we have $\delta p_y = 0$ and $\delta u_z = 0$.

Introducing the perturbation in the equations (2.22)-(2.24), and keeping in mind the geometry of our system, we get a linear system of equations for δp_z and δu_y

$$\frac{\partial}{\partial t}\begin{pmatrix} \delta p_z \\ \delta u_y \end{pmatrix} = \begin{pmatrix} \frac{K}{\Gamma}\partial_z^2 & \frac{1}{2}(\xi-1)\partial_z \\ -\frac{K(\xi-1)}{2}\partial_z^3 - \zeta\phi\partial_z & \eta\partial_z^2 \end{pmatrix}\begin{pmatrix} \delta p_z \\ \delta u_y \end{pmatrix} \tag{2.29}$$

We can then decompose δp_z and δu_y in the following Fourier ansatz, chosen to respect the boundary conditions at the walls.

$$\delta p_z(z,t) = \sum_{n=1}^{\infty} \tilde{p}_{zn} e^{\lambda_n t} \cos\left(\frac{n\pi z}{L}\right) \tag{2.30}$$

$$\delta u_y(z,t) = \sum_{n=1}^{\infty} \tilde{u}_{yn} e^{\lambda_n t} \sin\left(\frac{n\pi z}{L}\right). \tag{2.31}$$

Thus, Eq. 2.29 is transformed into an eigenvalue problem:

$$\lambda_n \begin{pmatrix} \tilde{p}_{zn} \\ \tilde{u}_{yn} \end{pmatrix} = \underbrace{\begin{pmatrix} -\frac{K}{\Gamma}\frac{n^2\pi^2}{L^2} & -\frac{1}{2}(\xi-1)\frac{n\pi}{L} \\ \frac{K(\xi-1)}{2}\frac{n^3\pi^3}{L^3} - \zeta\phi\frac{n\pi}{L} & -\eta\frac{n^2\pi^2}{L^2} \end{pmatrix}}_{A} \begin{pmatrix} \tilde{p}_{zn} \\ \tilde{u}_{yn} \end{pmatrix} \tag{2.32}$$

If both eigenvalues are negative, then the aligned rest state is stable and the perturbations decay exponentially with time. However, if at least one of them is positive, the rest state is unstable, and the system will start to flow. By analysing Eq. 2.32, we can see that $Tr(A)$, which is equal to the sum of the eigenvalues, is negative. We conclude that either both eigenvalues are negative, or one is negative and the other one positive. If the latter is true, then $det(A)$, which is equal to the product of the eigenvalues, is also negative. We can then simply say that the system is unstable to linear perturbations if $det(A) < 0$. This condition is equivalent to having the activity above a certain critical threshold $|\zeta| > \zeta_c$, with ζ_c:

$$\zeta_c = \frac{K\pi^2\left[(\xi-1)^2 + \frac{4\eta}{\Gamma}\right]}{2\phi L^2(\xi-1)} \ . \tag{2.33}$$

We note that the critical activity scales with the system size as $\zeta_c \sim \frac{1}{L^2}$. Therefore, increasing L is another way of reaching the threshold for instability. The origin of this scaling is related to the hydrodynamic interaction. We recall that the hydrodynamic interaction between force dipoles is long-range and that the fluid flow generated decays with distance as $\sim \frac{1}{r^2}$. In our confined system, the walls limit the distance of interaction between particles because the fluid flow must be zero at the wall (no-slip conditions). Thus, increasing the distance between the walls increases the effective range for hydrodynamic interaction between particles. This makes it more likely to introduce macroscopic effects.

This instability of the active fluid is known in the literature as hydrodynamic or generic instability. It is characterised by a switch between a state of no flow and a state of macroscopic coherent motion. The flowing states are always associated with disturbances in the orientational order. Let us take the case of contractile dipoles to illustrate the mechanics of the instability (see Fig.2.2). In the aligned state (1) the active forces balance and there is no flow. However, if a small splay deformation is introduced, the force density becomes larger on the left than on the right (2). As a result, a flow is set up from left to right, which causes the splay

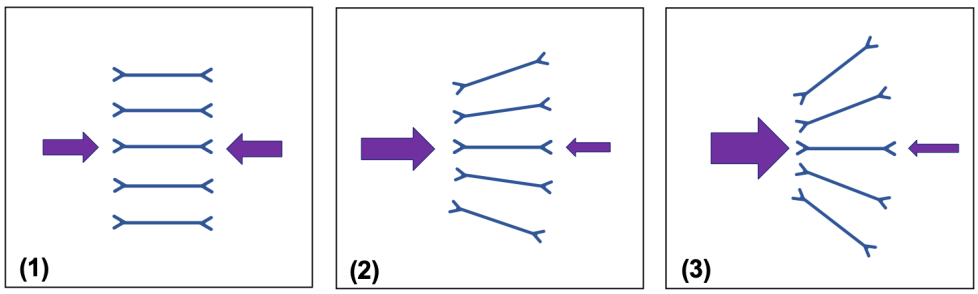

Figure 2.2 *Schematic representation of the force imbalance in the generic instability for contractile particles ($\zeta < 0, |\zeta| > \zeta_c$). (1) When the system is aligned, the active forces (purple arrows) balance. (2) A splay of the orientation leads to a force imbalance and creates flow to the right. (3) The flow generated creates further splay, thus setting up the instability.*

to increase (3). Hence, the system is unstable and it starts to flow. Inverting the signs of the force dipole, the same argument tells us that extensile fluids are stable with respect to splay. In the extensile case, bend deformations are the ones to grow and induce flows. Contractile fluids are unstable to splay, and extensile fluids are unstable to bend [50]. This argument has remarkable consequences for motility in active fluids, as we will see throughout this thesis.

Chapter 3

Hybrid lattice Boltzmann method

In order to study the properties of active fluids, we typically need to solve two coupled sets of partial differential equations. These equations define the active fluid hydrodynamic model, as presented in Chapter 2. One set describes the spatio-temporal evolution of the order parameters (concentration – Eq. (2.5), and polarisation – Eq. (2.6)), whereas the other set describes the conservation of mass and momentum (*via* the incompressible Navier-Stokes equation for the velocity field – Eqs. (2.9)-(2.10)).

Due to their inherent non-linearities, these equations are very complex to solve numerically. In particular, solving the incompressible Navier-Stokes equation implies updating the fluid velocity $\mathbf{u}$ (at time $t + \Delta t$), while simultaneously keeping $\nabla \cdot \mathbf{u} = 0$. Lattice Boltzmann (LB) offers an ideal approach to solve these equations, which efficiently addresses the full fluid dynamics, inclusively in three dimensions. The LB algorithm proceeds by introducing a "mesoscopic" distribution, proportional to the density of fluid particles sitting at a lattice node with a certain velocity (which is chosen from a discrete set of velocities), at a certain time t. The distribution functions evolve according to an appropriate local dynamic – the LB equation. The continuity and Navier-Stokes equations are recovered upon coarse-graining, provided conservation constraints are applied to the moments of the distribution that correspond to key physical properties.

In this thesis, we apply a hybrid lattice Boltzmann method where the LB algorithm is used to solve the Navier-Stokes equation, and is coupled to standard finite differences for the order parameter dynamics. With this procedure, at each time step, the fluid velocity found by LB is used to calculate the advection of the

order parameters; and the updated order parameters are fed back to the Navier-Stokes equation. This division of labour means that LB is *only* used to handle the momentum and mass transport – the problem for which it was originally devised. The hybrid approach reduces significantly the amount of required memory, which is particularly important in multicomponent or three-dimensional simulations.

In the following sections we describe the LB scheme and its implementation in 3D. We have used the 3D implementation throughout. Where quasi-2D and quasi-1D systems are simulated, one or two of the lattice dimensions (respectively) are set to 1. More details on the LB technique can be found in Refs [9, 48, 51–55].

3.1 The lattice Boltzmann equation

Lattice Boltzmann algorithms were first developed as mean-field versions of cellular automata simulations [56, 57] but can also usefully be viewed as a particular discretized version of the general Boltzmann equation:

$$\frac{\partial f}{\partial t} + \mathbf{u} \cdot \nabla_{\mathbf{x}} f + \frac{\mathbf{F}}{m} \cdot \nabla_{\mathbf{u}} f = \left(\frac{\partial f}{\partial t} \right)_{coll} . \tag{3.1}$$

Here, $f(\mathbf{x}, \mathbf{u}, t)$ is a distribution function, defined as the average number of particles that, at time t, are at position $\mathbf{x}$ having velocity $\mathbf{u}$. $\mathbf{F}$ is the external force acting on the particles and $\left(\frac{\partial f}{\partial t}\right)_{coll}$ is a collision term describing the relaxation to equilibrium. Note that in chapter 3 we use $\mathbf{x} = (x, y, z)$ to denote the discrete position and avoid confusion with the continuous position $\mathbf{r}$ used in chapter 2.

To obtain a discrete representation, we consider a 3D cubic lattice with lattice spacings $\Delta x = \Delta y = \Delta z$. The velocities are also discretized so that $\mathbf{v}$ can only take a finite set of values $\{\mathbf{e}_0, ..., \mathbf{e}_{N_v}\}$. In 3D, we use a scheme with $N_v = 15$ different velocities, known as the D3Q15:

$$\begin{aligned} \mathbf{e}_0^{(0)} &= (0, 0, 0) \\ \mathbf{e}_{1-6}^{(1)} &= (0, 0, \pm c), (0, \pm c, 0), (\pm c, 0, 0) \\ \mathbf{e}_{7-14}^{(2)} &= (\pm c, \pm c, \pm c) \ . \end{aligned} \tag{3.2}$$

$c = \frac{\Delta x}{\Delta t}$ so that the discrete velocities correspond to moving by one lattice site in a time-step. The velocities are assigned to different groups by the superscript $s = 0, 1, 2$. The groups $\mathbf{e}_i^{(s)}$ are defined so that all the velocities

in one group have the same absolute value (which is different from the other groups). For simpler visualisation, a schematic representation of the 15 velocity vectors $\{\mathbf{e}_i\}, i = 0, ..., 14$ is shown in Fig. 3.1.

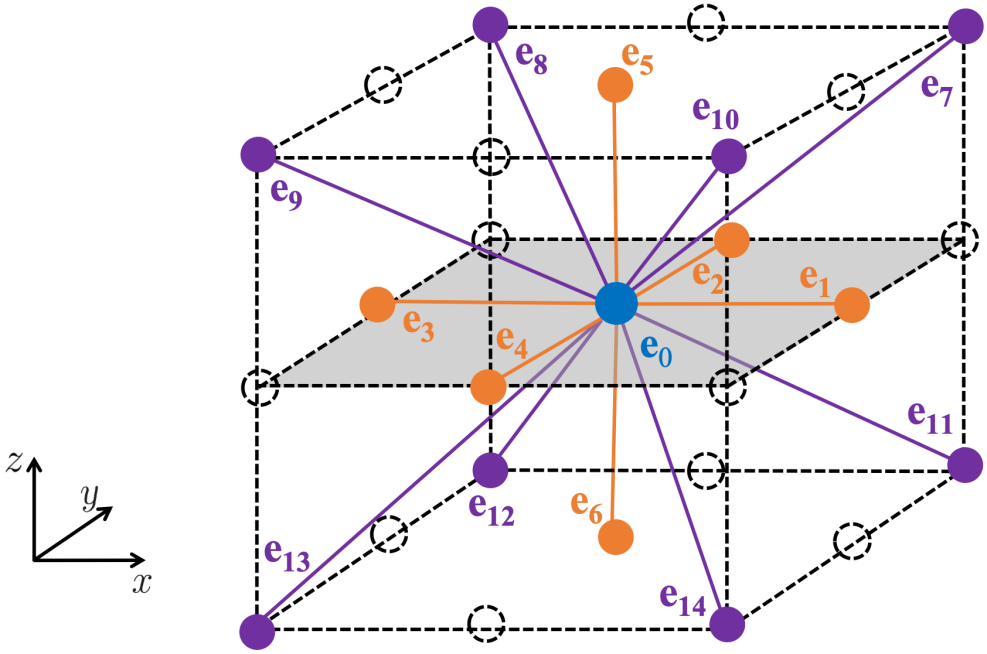

Figure 3.1 *Discrete lattice Boltzmann velocities* $\{e_i^{(s)}\}$ *in a 3D lattice. Groups with different absolute values correspond to different colours:* $s = 0, |e_i| = 0$ *is representend in blue,* $s = 1, |e_i| = c$ *corresponds to orange, and* $s = 2, |e_i| = \sqrt{3}c$ *to purple. The 15 vectors shown* $\{\boldsymbol{e}_0, ..., \boldsymbol{e}_{14}\}$ *correspond to the D3Q15 scheme used in this thesis. (Figure adapted from [9]).*

To simplify the notation, we refer to $f(\mathbf{x}, \mathbf{e}_i, t)$ as $f_i(\mathbf{x}, t)$, with the subscript i labelling the lattice velocities. It is also customary to set the lattice spacing, the time-step, and the particles' mass to unity $\Delta x = \Delta t = m = 1$. This choice defines the *simulation units* that will be used in this thesis throughout. The mapping between simulation units and physical units will be explained in more detail in the last section of the Chapter.

The physical observables can be derived from the discrete distribution functions by summing over all possible velocity vectors. In particular, the fluid density $\rho(\mathbf{x}, t)$ and velocity $\mathbf{u}(\mathbf{x}, t)$ are given by

$$\rho(\mathbf{x}, t) = \sum_i f_i(\mathbf{x}, t), \tag{3.3}$$

$$\mathbf{u}(\mathbf{x}, t) = \frac{1}{\rho(\mathbf{x}, t)} \sum_i f_i(\mathbf{x}, t)\, \mathbf{e}_i \ . \tag{3.4}$$

We are now able to write down the evolution of the distribution functions for a time-step Δt:

$$\underbrace{f_i\left(\mathbf{x}+\mathbf{e}_i\Delta t, t+\Delta t\right)=f_i\left(\mathbf{x},t\right)}_{streaming}+\Delta t F_i+\underbrace{\Delta t\ \mathcal{C}_{f_i}}_{collision}\ . \tag{3.5}$$

This represents free streaming with velocity $\mathbf{e}_i$ followed by a collision step, where the operator $\mathcal{C}_{f_i}$ allows the distribution to relax to equilibrium.

The simplest choice for the collision operator is a single relaxation time form (BGK approximation [58]):

$$\mathcal{C}_{f_i}=-\frac{f_i\left(\mathbf{x},t\right)-f_i^{eq}\left(\mathbf{x},t\right)}{\tau}\ . \tag{3.6}$$

The collision operator is approximated as a difference between the distribution function f_i and its equilibrium value f_i^{eq}, with τ being the relaxation time-scale to reach equilibrium. Incidentally, τ is also related to the macroscopic viscosity η. For the predictor-corrector scheme used in this thesis (see Eq. (3.9) below) we have $\eta=\frac{\tau\rho}{3}$. In the continuous Boltzmann equation, the equilibrium distribution $f_i^{eq}\left(\mathbf{x},t\right)$ is given by the Maxwell-Boltzmann equation:

$$f^{eq}\left(\mathbf{u}\right)=\frac{\rho}{\left(2\pi T\right)^{2/3}}e^{-(u-v)^2/2T}\ , \tag{3.7}$$

where T is the system's temperature and $\mathbf{u}$ is continuous. In the LB method, since the velocities are discretized, we use a polynomial expansion in $\mathbf{e}_i$ and $\mathbf{u}$ to approximate (3.7). The form of the equations of motion and thermodynamic equilibrium follow from the choice of moments of the equilibrium distribution f^{eq}, which constrain the expansion coefficients. This will be the topic of the next sections.

Finally, we write the LB equation for the distribution functions f_i as:

$$f_i\left(\mathbf{x}+\mathbf{e}_i\Delta t, t+\Delta t\right)=f_i\left(\mathbf{x},t\right)+\Delta t F_i-\Delta t\left[\frac{f_i\left(\mathbf{x},t\right)-f_i^{eq}\left(\mathbf{x},t\right)}{\tau}\right]\ . \tag{3.8}$$

We can describe this process in two steps: the first is the collision where each f_i relaxes to f_i^{eq} at a rate governed by τ; the second is a moving step where each $f_i(\mathbf{x})$ is moved to $f_i\left(\mathbf{x}+\mathbf{e}_i\Delta t\right)$.

We note that the dynamics described in Eq. (3.8) is fully local. Locality is important for the efficient parallelisation of the implementation code, and

maintains near-linear scaling of the computational cost with the size of the system [54]. This means that slight fluid compressibility is allowed (the sound-speed is finite) and removes the need for having to solve each time-step for a pressure field that responds instantaneously to distant events.

In practice, we implement the evolution described in Eq. (3.8) through a predictor-corrector-like scheme [9]:

$$f_i\left(\mathbf{x}+\mathbf{e}_i\Delta t, t+\Delta t\right) = f_i\left(\mathbf{x},t\right) + \Delta t F_i + \frac{1}{2}\Delta t\left[\mathcal{C}_{f_i}\left(\mathbf{x},t,\{f_i\}\right) + \mathcal{C}_{f_i}\left(\mathbf{x}+\mathbf{e}_i\Delta t, t+\Delta t, \{f_i^*\}\right)\right] , \tag{3.9}$$

with $\mathcal{C}_{f_i}$ as defined in Eq. (3.6). f_i^* is a first order approximation to $f_i\left(\mathbf{x}+\mathbf{e}_i\Delta t, t+\Delta t\right)$, given by $f_i^* = f_i + \Delta t\mathcal{C}_{f_i}$. Discretizing in this way has the advantages that lattice viscosity terms are eliminated to second order (which we show in the next section), and that the stability of the scheme is improved.

3.2 The Chapman-Enskog expansion

The Navier-Stokes and continuity equations that govern the behaviour of the system can be formally derived from the lattice Boltzmann equation in the long wavelength limit.

We start by writing down a Taylor expansion for the distribution function $f_i\left(\mathbf{x}+\mathbf{e}_i\Delta t, t+\Delta t\right)$ and the collision operator $\mathcal{C}_{f_i}\left(\mathbf{x}+\mathbf{e}_i\Delta t, t+\Delta t, f_i^*\right)$. We expand $f_i\left(\mathbf{x}+\mathbf{e}_i\Delta t, t+\Delta t\right)$ up to second order in Δt, while we only go up to first order for $\mathcal{C}_{f_i}\left(\mathbf{x}+\mathbf{e}_i\Delta t, t+\Delta t, f_i^*\right)$ (since it appears in Eq. (3.9) already multiplied by Δt).

$$f_i\left(\mathbf{x}+\mathbf{e}_i\Delta t, t+\Delta t\right) = f_i\left(\mathbf{x},t\right) + \Delta t D f_i\left(\mathbf{x},t\right) + \frac{\Delta t^2}{2}D^2 f_i\left(\mathbf{x},t\right) + \mathcal{O}\left(\Delta t^3\right) \tag{3.10}$$

$$\mathcal{C}_{f_i}\left(\mathbf{x}+\mathbf{e}_i\Delta t, t+\Delta t, f_i + \Delta t\mathcal{C}_{f_i}\left(x,t,f_i\right)\right) = \mathcal{C}_{f_i}\left(\mathbf{x},t,f_i\right) + \Delta t D\mathcal{C}_{f_i}\left(\mathbf{x},t,f_i\right) + \mathcal{O}\left(\Delta t^2\right) \tag{3.11}$$

In the equations above, we have defined $D \equiv \partial_t + e_{i\alpha}\partial_\alpha$. Substituting the two

expanded forms back into Eq. (3.9), we find:

$$Df_i(\mathbf{x},t) = \mathcal{C}_{f_i}(\mathbf{x},t,f_i) - \frac{\Delta t}{2}\left[D^2 f_i(\mathbf{x},t) - D\mathcal{C}_{f_i}(\mathbf{x},t,f_i)\right] + \mathcal{O}\left(\Delta t^2\right) \ . \quad (3.12)$$

So that, up to terms in Δt,

$$Df_i(\mathbf{x},t) = \mathcal{C}_{f_i}(\mathbf{x},t,f_i) + \mathcal{O}(\Delta t) \ . \quad (3.13)$$

Thus, there are no terms of order Δt back in Eq. (3.12).

$$\Delta t\left[D^2 f_i(\mathbf{x},t) - D\mathcal{C}_{f_i}(\mathbf{x},t,f_i)\right] = \mathcal{O}\left(\Delta t^2\right) \ , \quad (3.14)$$

and

$$Df_i(\mathbf{x},t) = \mathcal{C}_{f_i}(\mathbf{x},t,f_i) + \mathcal{O}\left(\Delta t^2\right) \ . \quad (3.15)$$

Terms proportional to Δt do appear in other lattice Boltzmann discretizations and can be included in the viscosity. The fact that we manage to eliminate such lattice viscosity at this stage is a consequence of the choice to discretize in a predictor-corrector fashion [9], shown in Eq. (3.9).

We now proceed with a multi-scale expansion of the distribution function

$$f = f^{(0)} + f^{(1)} + f^{(2)} + \ldots \quad (3.16)$$

so that $f^{(0)} \sim \mathcal{O}(\partial^0)$, $f^{(1)} \sim \mathcal{O}(\partial)$, $f^{(2)} \sim \mathcal{O}(\partial^2)$.

This procedure is referred to as the Chapman-Enskog expansion and the aim is to show that the lattice Boltzann equation reproduces the Navier-Stokes and continuity equations for the fluid. To that effect, we substitute the expansion (3.16) in Eq. (3.15) and, using the collision operator in Eq. (3.6), equate each order $\mathcal{O}(\partial^n)$ separately to obtain the following three conditions:

$$\begin{cases} \mathcal{O}(\partial^0): & f_i^{(0)} = f_i^{eq} \\ \mathcal{O}(\partial^1): & f_i^{(1)} = -\tau D f_i^{eq} \\ \mathcal{O}(\partial^2): & f_i^{(1)} = \tau^2 D^2 f_i^{eq} \end{cases} \quad (3.17)$$

In order to recover the physical description of the system, we now look at the observables, which we defined as moments of the distribution functions in (3.3) and (3.4). In doing so, it is important to consider the following constraints, that

ensure physical meaning:

$$\sum_i f_i^{eq} = \rho \tag{3.18}$$

$$\sum_i f_i^{eq} e_{i\alpha} = \rho u_\alpha \tag{3.19}$$

$$\sum_i f_i^{eq} e_{i\alpha} e_{i\beta} = -\sigma_{\alpha\beta} + \rho u_\alpha u_\beta \tag{3.20}$$

$$\sum_i f_i^{eq} e_{i\alpha} e_{i\beta} e_{i\gamma} = \frac{\rho}{3} \left(u_\alpha \delta_{\beta\gamma} + u_\beta \delta_{\alpha\gamma} + u_\gamma \delta_{\alpha\beta} \right) \tag{3.21}$$

The first two equations correspond to the local conservation of mass and momentum, while the last two relate to the definitions of pressure and stress.

Let us use the fluid density definition to obtain the continuity equation. Inserting the expansion (3.16) into the density (3.3) and considering only terms up to second order:

$$\begin{aligned} \rho &= \sum_i \left(f^{(0)} + f^{(1)} + f^{(2)} \right) \\ &= \sum_i f_i^{eq} - \tau \sum_i D f_i^{eq} + \tau^2 \sum_i D^2 f_i^{eq} \ . \end{aligned} \tag{3.22}$$

The second line of Eq. (3.22) is obtained with the conditions (3.17). Remembering mass conservation, we are left with:

$$\sum_i D f_i^{eq} = \tau \sum_i D^2 f_i^{eq} \ . \tag{3.23}$$

And thus, up to second order in the gradients

$$\partial_t \underbrace{\sum_i f_i^{eq}}_{\rho} + \partial_\alpha \underbrace{\sum_i f_i^{eq} e_{i\alpha}}_{\rho u_\alpha} = \mathcal{O}\left(\partial^2\right) \ . \tag{3.24}$$

Which is simply the continuity equation $\partial_t \rho + \nabla \cdot (\rho \mathbf{u}) = 0$. The very same procedure can be applied to the momentum equation $\sum_i f_i e_{i\alpha} = \rho u_\alpha$, resulting in the Navier-Stokes equation.

3.3 Polynomial expansion for the equilibrium distribution

We have now shown how, with the right choice of constraints, the lattice Boltzmann equation can lead to the full description of the system's dynamics. However, we have still not given an explicit form to the equilibrium distribution f_i^{eq}. A suitable form, that satisfies the constraints (3.18)-(3.21) is the following polynomial of the velocities [9]

$$f_i^{eq} = A_s + B_s u_\alpha e_{i\alpha} + C_s u^2 + D_s u_\alpha u_\beta e_{i\alpha} e_{i\beta} + E_{s\alpha\beta} e_{i\alpha} e_{i\beta} \tag{3.25}$$

The coefficients are determined by evaluating (3.18)-(3.21) and matching the corresponding terms. In doing so, the following symmetry relations for the lattice velocity vectors are important:

$$\sum_{i=1}^{6} e_{i\alpha}^{(1)} = \sum_{i=7}^{14} e_{i\alpha}^{(2)} = 0, \ \alpha = x, y, z \tag{3.26}$$

$$\sum_{i=1}^{6} e_{i\alpha}^{(1)} e_{i\beta}^{(1)} = 2\delta_{\alpha\beta}, \ \sum_{i=7}^{14} e_{i\alpha}^{(2)} e_{i\beta}^{(2)} = 8\delta_{\alpha\beta} \tag{3.27}$$

$$\sum_{i=1}^{6} e_{i\alpha}^{(1)} e_{i\beta}^{(1)} e_{i\gamma}^{(1)} = \sum_{i=7}^{14} e_{i\alpha}^{(2)} e_{i\beta}^{(2)} e_{i\gamma}^{(2)} = 0 \tag{3.28}$$

$$\sum_{i=1}^{6} e_{i\alpha}^{(1)} e_{i\beta}^{(1)} e_{i\gamma}^{(1)} e_{\epsilon}^{(1)} = 2\delta_{\alpha\beta}\delta_{\beta\gamma}\delta_{\gamma\epsilon} \tag{3.29}$$

$$\sum_{i=7}^{14} e_{i\alpha}^{(2)} e_{i\beta}^{(2)} e_{i\gamma}^{(2)} e_{\epsilon}^{(2)} = 8\Delta_{\alpha\beta\gamma\epsilon} - 16\delta_{\alpha\beta}\delta_{\beta\gamma}\delta_{\gamma\epsilon} \tag{3.30}$$

where $\Delta_{\alpha\beta\gamma\epsilon} = \delta_{\alpha\beta}\delta_{\gamma\epsilon} + \delta_{\alpha\gamma}\delta_{\beta\epsilon} + \delta_{\alpha\epsilon}\delta_{\beta\gamma}$.

The resulting coefficients are then determined to be:

$$A_2 = \frac{\rho T}{10}, \ A_1 = A_2, \ A_0 = \rho - 14A_2 \tag{3.31}$$

$$B_2 = \frac{\rho}{24}, \ B_1 = 8B_2 \tag{3.32}$$

$$C_2 = -\frac{\rho}{24}, \ C_1 = 2C_2, \ C_0 = -\frac{2}{3}\rho \tag{3.33}$$

$$D_2 = \frac{\rho}{16}, \ D_1 = 8D_2 \tag{3.34}$$

$$E_{2\alpha\beta} = \sigma_{\alpha\beta}, \ E_{1\alpha\beta} = 8E_{2\alpha\beta} \tag{3.35}$$

3.4 Spurious velocities

One typical problem with both lattice Boltzmann and finite difference simulations of multiphasic systems is the appearance of spurious, non-zero velocities in interfacial regions [10, 55] - see Fig.3.2. This undesired effect, that leads to unphysical flows near interfaces, is due to discretization errors. The spurious velocities are generated when the continuous operators in the Navier-Stokes equation are replaced by their discrete approximations. In other words, spurious velocities correspond to the contribution from the higher order terms that were not included in the expansion used to discretize the derivatives.

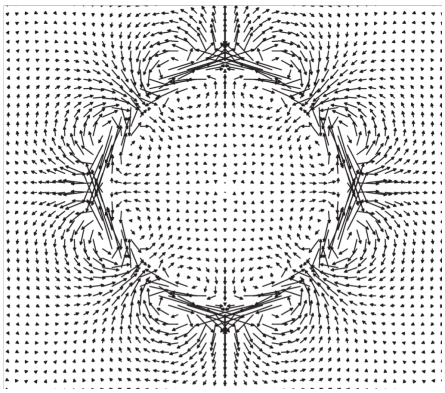

Figure 3.2 *Spurious velocities around a liquid droplet in a gas phase.(Figure taken from [10]).*

By finding the best way to numerically calculate derivatives, spurious velocities can be reduced by an order of magnitude with respect to standard discretization procedure. In our simulations, we used the 3D "stencil" found in [10].

$$\partial_x = \frac{1}{12\ \Delta x}\left(\begin{bmatrix} 0 & 0 & 0 \\ -1 & 0 & 1 \\ 0 & 0 & 0 \end{bmatrix}, \begin{bmatrix} -1 & 0 & 1 \\ -2 & 0 & 2 \\ -1 & 0 & 1 \end{bmatrix}, \begin{bmatrix} 0 & 0 & 0 \\ -1 & 0 & 1 \\ 0 & 0 & 0 \end{bmatrix}\right) \tag{3.36}$$

$$\partial_x^2 = \frac{1}{6\ \Delta x^2}\left(\begin{bmatrix} 0 & 1 & 0 \\ 1 & 2 & 1 \\ 0 & 1 & 0 \end{bmatrix}, \begin{bmatrix} 1 & 2 & 1 \\ 2 & -24 & 2 \\ 1 & 2 & 1 \end{bmatrix}, \begin{bmatrix} 0 & 1 & 0 \\ 1 & 2 & 1 \\ 0 & 1 & 0 \end{bmatrix}\right) \tag{3.37}$$

In (3.36) and (3.37), the matrix positions refer to the lattice vectors (3.2) such that for the left, middle, and right matrices $e_{iz} = c, 0,$ and $-c$, respectively. The same applies within each matrix for the x and y components of $\mathbf{e}_i$. Thus, and referring back to the lattice in Fig. 3.1 with $\Delta x = \Delta y = \Delta z = 1$, we have

$$\partial_x\, g(x_0,y_0,z_0) = \frac{1}{12}\{\; g(x_0+1,y_0,z_0+1) - g(x_0-1,y_0,z_0+1) \\ + 2g(x_0+1,y_0,z_0) + g(x_0+1,y_0+1,z_0) + g(x_0+1,y_0-1,z_0) \\ - 2g(x_0-1,y_0,z_0) - g(x_0-1,y_0+1,z_0) - g(x_0-1,y_0-1,z_0) \\ + g(x_0+1,y_0,z_0-1) - g(x_0-1,y_0,z_0-1)\;\} \quad (3.38)$$

for a generic function $g(\mathbf{x})$ at $\mathbf{x}_0 = (x_0, y_0, z_0)$.

3.5 Boundary conditions

We typically perform lattice Boltzmann simulations in a box of dimensions $L_x \times L_y \times L_z$. For the quasi-2D and quasi-1D simulations presented in the following chapters, we simply set one or two of the dimensions L_α to one. The simplest type of boundary is one with periodic conditions on all sides of the box. In particular, for quasi-2D and quasi-1D systems, this ensures invariance along the directions with $L_\alpha = 1$. We have used periodic boundary conditions in all simulations in this thesis.

For some physical problems it is necessary to consider a simulation box with solid walls. Appendix A details the most common boundary conditions in such cases.

3.6 Mapping simulation units to physical units

Throughout this thesis, the values of physical system parameters are quoted in simulation units. As mentioned before in the text, simulation units result from the choice to set the time, length, and mass scales to 1 in the simulation. Here we illustrate how to obtain the simulation parameters from the physical ones, and *vice-versa*.

In order to do the conversion, we need to choose the appropriate physical scales and express all the quantities as a function of those. We shall take the example of bacteria. Typical bacterium size is $\Delta x = 4\mu m$, typical mass is $m = 0.1\mu g$. We choose $\Delta t = 0.1s$, the duration of a bacterial tumble event. We now want to express a swimming speed of $v_p = 2\mu m/s$ in simulation units. We start by

writing the speed in terms of the chosen scales:

$$\begin{aligned} v_p &= 2\mu m/s \\ &= 0.05\ \frac{4\mu m}{0.1s} \\ &= 0.05\ \frac{\Delta x}{\Delta t} \end{aligned} \tag{3.39}$$

Since in the simulations all the scales are set to one, the speed in simulation units is simply $v_s = 0.05$. To return to physical units, all that is needed is to reintroduce the chosen scales. For the speed example above: $v_p = v_s \frac{\Delta x}{\Delta t}$.

The choice of scales considered in the simulations and corresponding physical units are quoted in the text of the results Chapters, whenever necessary.

Chapter 4

Anchoring-driven spontaneous rotations in active gel droplets

In Chapter 2, we introduced the hydrodynamic theory of active gels. Within this framework, swimming active particles are approximated by force dipoles that push (extensile stress) or pull (contractile stress) on the surrounding fluid. One known consequence of active stresses is the existence of a generic instability in which the system switches from a rest state to one where the active fluid flows coherently. Spontaneously flowing states are always associated with a non-uniform orientation profile. This non-equilibrium transition can be understood through the interplay between elasticity, which favours the alignment of the active particles parallel to each other, and activity. If the activity is small when compared to the elasticity, the particles tend to be aligned. In an aligned state, active forces balance and there is no flow. Above a certain activity threshold, the force imbalance associated with a small elastic deformation is enough to set up a flow, which in turn causes further deformation. Hence, the system becomes unstable and it starts to flow spontaneously (*i.e.* due only to internal forces). The transition depends on the type of activity, extensile gels are unstable to bend deformations, while contractile gels are unstable to splay. (For further details see Section 2.4.)

We now focus on the effects of active stresses under confinement. In fact, most instances of biological active fluids are found in confined geometries (*e.g.* biofilms, bacterial colonies, bacterial carpets, cells, and tissues). In particular, we are concerned with the case of active droplets. To this effect, we perform simulations

in a binary system where a droplet of active gel is embedded in an isotropic, and Newtonian, aqueous solvent. Active droplets can be used as a simplified mechanical model to address the dynamics of bacterial colonies and cells. The geometry, previously considered in [4, 11, 59], can be realised in the lab through actomyosin droplets or cell extracts, and it could also be made by encapsulating kinesin-microtubule gels into oil-water emulsions, as done in [60].

In an active droplet, besides the elastic alignment and active stirring, there are two other important factors to consider: the surface tension and the anchoring. The surface tension controls the droplet shape by minimizing the interfacial area, while the anchoring refers to the particle orientation at the interface.

Previous work has shown that, in the absence of any anchoring, the above mentioned generic instability can set an active droplet into motion. The onset of motility is linked to the set-up of force multipoles [61, 62], as in other examples of active droplets which are not based on active gels [63–66].

Tjhung *et al.* showed that activity alone can drive the droplet to become self-motile in both 2D and 3D [4]. Under confinement, the spontaneous flow found in high activity states is realised as a pair of fluid vortices (recall that there can be no fluid sources or sinks due to the incompressibility condition) which propel the droplet forward – see Fig. 4.1(e).

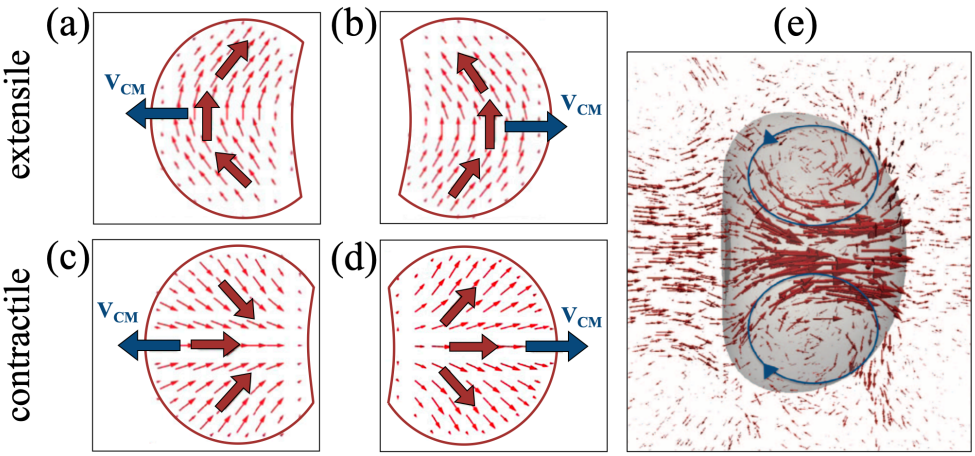

Figure 4.1 *Self-motile active gel droplets in 2 and 3 dimensions. (a)-(b) Extensile droplets translating in different directions, due to bend deformations. (c)-(d) Splayed configurations power motility in contractile droplets. (e) Flow field for a contractile droplet moving in 3D.*
Figure based on [4].

The key control parameter in the simulations of [4] was the dimensionless activity

parameter $\Theta = \zeta R^2/K$, where ζ is the active stress parameter as defined in Eq. 2.14, R is the droplet radius, and K is the elastic constant of the active gel (which penalises deformations from the aligned state - see Eq. 2.4). If Θ is small, the droplet deforms due to activity but it is stationary; instead, if Θ exceeds a critical threshold, then elastic deformations (splay for contractile droplets – see Fig. 4.1(a)-(b), or bend for extensile ones – see Fig. 4.1(c)-(d)) create an imbalance in internal active forces which leads to motion. The transition between quiescent and self-motile phases requires the spontaneous breaking of the polarity inversion symmetry, and provides a mechanism through which cell extracts (viewed as actomyosin droplets with a surface tension) could, in principle, move solely by virtue of myosin contractility, and in the absence of actin treadmilling, which instead regulates standard cell crawling on a substrate [59].

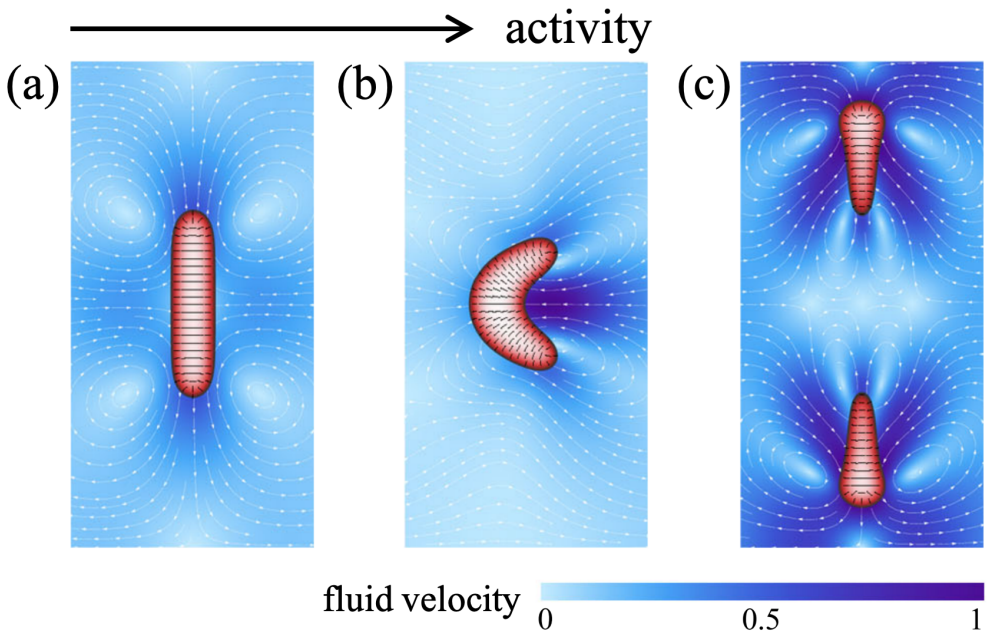

Figure 4.2 *Active contractile droplet for increasing activity. (a) The droplet elongates, while remaining static. (b) The droplet deforms and translates. (c) The droplet divides into 2 daughter droplets that swim away from each other.*
Figure produced from [11].

Further work in [11] has shown that a droplet of contractile active nematic can even spontaneously split at large values of the activity, mimicking cell division. In that case, the prime competition is between the surface tension and the activity. This is captured by a second important dimensionless number, the "active capillary number" Φ, measuring the ratio between active forces and surface tension $\tilde{\sigma}$, $\Phi = \zeta R/\tilde{\sigma}$. When the active forces are sufficiently larger than

the surface tension, the droplet is able to deform significantly and even break apart (see Fig. 4.2).

In both the self-motility and division examples, there was no anchoring present (or only a very weak one). The active stirring promotes states that include deformations and spontaneous flows, and is opposed only by elasticity and surface tension. As a result of this interplay, there is a clear non-equilibrium transition between static and motile droplet states.

In the present Chapter, we discuss the dynamics of an active droplet in the presence of an imposed (e.g., thermodynamic) anchoring, which favours either normal or planar alignment of the polarisation field at the droplet's interface. Anchoring can arise in nature and in the lab due to the fluid's chemical composition or to the interaction with surfaces.

As we will detail in the results below, if the strength of the anchoring is large enough, we find that an increase in activity leads to spontaneously rotating, rather than self-motile, droplets. Spontaneous rotations are also powered by elastic deformations and are typically accompanied by a change in droplet shape (droplets often attain a bean-shaped morphology). The nature of the transition between the quiescent and rotating phases depends on whether the droplet is contractile or extensile: hysteresis is found in the former case, but not in the latter one. Apart from a large enough dimensionless activity Θ (and possibly capillary number), we find that spontaneous rotations of the kind we observe require a sufficiently strong anchoring.

Our simulations further suggest that rotations require the anchoring to be of a particular nature: normal for extensile droplets and planar for contractile ones. A sufficiently strong anchoring of this kind is necessary to stabilise a pair of elastic deformations within the droplet: this polarisation pattern is associated with a pair of non-collinear active forces, which then creates a non-zero torque.

4.1 Modelling an active gel droplet

In order to model an active droplet, we use a binary liquid representation. To that effect, we write the ϕ dependant part of the free energy (2.4) as:

$$V_{droplet}\left(\phi, \nabla\phi\right) = \frac{\alpha}{4\phi_{cr}^2}\phi^2(\phi-\phi_0)^2 + \frac{\kappa}{2}|\nabla\phi|^2 + W\left(\mathbf{p}\cdot\nabla\phi\right)^2 \tag{4.1}$$

The first two terms stem from the binary fluid theory and allow for the formation of a droplet, which is stabilised by interfacial tension. The term proportional to α creates a double well potential with two minima states: a polar active phase inside the droplet ($\phi = \phi_0$, $\mathbf{p} \neq 0$), and a passive isotropic phase outside it ($\phi = 0$, $\mathbf{p} = 0$). ϕ_{cr} is the critical concentration for which the system becomes polar (see Eq. 2.4). Across the droplet interface, the values of the concentration and polarisation fields vary smoothly from a finite value to zero. In general, the width of this diffuse interface depends on the full form of the free energy, including the transition parameter A, elastic constant K, and the surface tension constant κ (see Eqs. 2.4 and 4.1). In our simulations, the interfacial width is typically much smaller than the size of the droplet: the interface spans around $2-3$ lattice sites, while the droplet radius is $R = 30$. The term proportional to $|\nabla\phi|^2$ describes an interfacial energy with proportionality constant $\kappa > 0$ related to the surface tension. This surface tension (which is positive) is then the energy cost of increasing the droplet's surface area.

The last term represents the anchoring of $\mathbf{p}$ to the droplet interface. W is the parameter that controls the anchoring strength and the type of anchoring. To construct this energy, we take advantage of the fact that $\nabla\phi$ defines the direction perpendicular to the interface (pointing inwards) and is non-zero only at the interface. Thus, for $W > 0$ the energy is minimised if $\mathbf{p}\cdot\nabla\phi = 0$, meaning $\mathbf{p}$ should be parallel to the interface. This results in planar anchoring. In turn, if $W < 0$ then $|\mathbf{p}\cdot\nabla\phi| = 1$ is required for energy minimization and $\mathbf{p}$ must be perpendicular to the interface, yielding normal anchoring. Because, the dependence in $\mathbf{p}\cdot\nabla\phi$ is quadratic, the anchoring is degenerate in both cases. Under normal anchoring, the polarisation can point in or out, while for planar anchoring any direction parallel to the interface is equally favoured. We should note here that both W and κ in Eq. (4.1) have units of N, whereas the quantities they are linked to, the experimentally measured strength of anchoring, which we call w, and the surface

tension, $\tilde{\sigma}$, have units of N/m.

A schematic representation of planar and normal anchoring is shown in Fig. 4.3. For simpler visualisation, the interface is represented in blue, while the interior of the droplet is coloured red. The same convention was chosen for the simulation results.

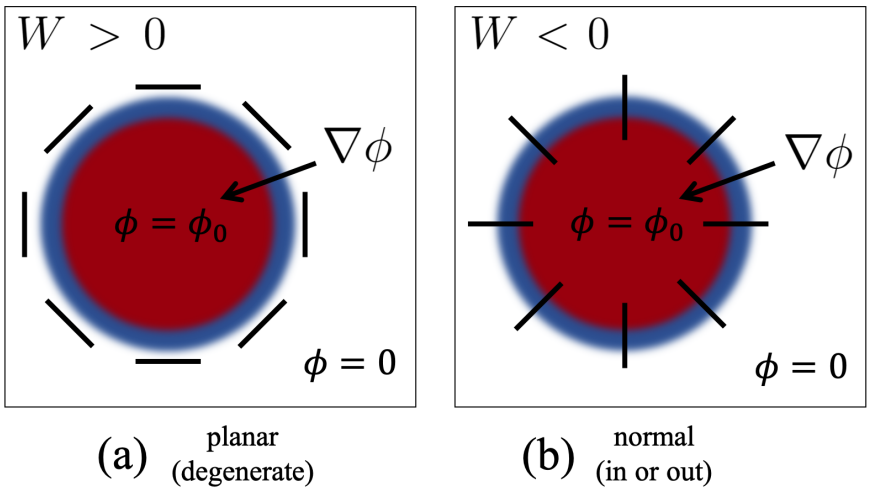

Figure 4.3 *Thermodynamic anchoring at the droplet interface. (a) For $W > 0$, $\boldsymbol{p}$ is perpendicular to $\nabla\phi$ and parallel to the interface – planar anchoring. (b) For $W < 0$, $\boldsymbol{p}$ is parallel to $\nabla\phi$ and perpendicular to the interface – normal anchoring.*

We should mention that the alignment at the surface is also affected by activity, as observed in previous simulations, in the absence of any thermodynamic forcing. These simulations have shown that active flows generated at the interface can lead to a dominant type of interfacial alignment [67] (the simulations were of nematic-isotropic interfaces, but the same effect occurs with polar order). Disregarding flow alignment effects, the interfacial alignment is planar for extensile activity and normal for contractile activity. This so-called "active anchoring" is produced by the combination of active normal stresses which deform the droplet, and active shear flows which turn the active dipole direction (see [67] for more details). Since active anchoring results from active stresses that extend into the bulk of the active fluid, its effective anchoring strength is $\sim \zeta l$, where l is the typical lengthscale of distortions in the nematic phase [68].

Quite remarkably, for the cases we present here, we only observe droplet rotations when the nature of the thermodynamically imposed anchoring (i.e., whether planar or normal to the surface) conflicts with the nature of the effective anchoring that arises due to activity.

Finally, the presence of an interface is also responsible for an extra stress term in the Navier-Stokes equation:

$$\sigma_{\alpha\beta}^{interface} = \left(f - \phi \frac{\delta F}{\delta \phi} \right) \delta_{\alpha\beta} - \frac{\partial f}{\partial \left(\partial_\beta \phi \right)} \partial_\alpha \phi. \tag{4.2}$$

We simulate the active droplets, using the hybrid lattice Boltzmann method outlined in Chapter 3, in two dimensions on a square lattice of size $L_x = L_y = 120$ lattice units.

To characterise the dynamics of our droplets we compute the average of the rotational velocity in the active phase as:

$$\omega = \frac{\int d\mathbf{r}\ \mathbf{r} \times \mathbf{u}(\mathbf{r})}{\int d\mathbf{r}\ \phi(\mathbf{r})}. \tag{4.3}$$

We also measure the translational speed of the droplet as

$$v = \frac{\int d\mathbf{r}\ \phi(\mathbf{r})\ \mathbf{u}(\mathbf{r})}{\int d\mathbf{r}\ \phi(\mathbf{r})}. \tag{4.4}$$

Unless explicitly stated, the parameters used for the simulations are: $R = 30$, $\phi_0 = 2$, $\phi_{cr} = 1$, $A = 0.04$, $\kappa = 0.25$ for extensile droplets and $\kappa = 0.06$ for contractile droplets, $\alpha = 0.1$, $K = 0.04$, $\xi = 1.1$ for flow aligning and $\xi = 0.5$ for flow tumbling, $\eta = 1$, $W = 0.1$ for planar anchoring and $W = -0.05$ for normal anchoring.

All the parameter values are quoted throughout in simulation units. A mapping to physical units can be obtained, as explained in Chapter 3, by choosing appropriate scales for length, time and force. For concreteness, we chose $L = 1\mu m$, $\tau = 10ms$, and $F = 100nN$. These values correspond to actomyosin (a contractile active gel). Table 4.1 lists the correspondence for the range of parameters used

It is also useful to summarise here the key dimensionless numbers in our model, which will be referred to when discussing the results. First, $\Theta = \frac{\zeta R^2}{K}$ measures the relative importance of active and elastic stresses; in our case, it controls the onset of active spontaneous flow within the droplet. Second, there is an active capillary number, $\Phi = \frac{\zeta R}{\tilde{\sigma}}$, where $\tilde{\sigma}$ is the surface tension of the droplet: this captures the

Model variables and parameters (actomyosin)	Simulation units	Physical units
Effective shear viscosity, η	1	$1\,\mathrm{kPa}\cdot\mathrm{s}$
Effective elastic constant, K	$0.02 - 0.08$	$2 - 8\,\mathrm{nN}$
Shape factor, ξ	1.1, 0.5	dimensionless
Effective diffusion constant, $D = Ma$	0.004	$0.4\,\mu\mathrm{m}^2/\mathrm{s}$
Rotational viscosity, Γ	1	$1\,\mathrm{kPa}\cdot\mathrm{s}$
Activity, ζ	$0 - 0.01$	$0 - 1\,\mathrm{kPa}$
Anchoring strength, W	$0 - 0.1$	$0 - 10\,\mathrm{nN}$

Table 4.1 *Model parameters in simulation units and the correspondent physical units (for an actomyosin gel: $L = 1\mu m$, $\tau = 10ms$, and $F = 100nN$).*

relative importance of active and interfacial forces, and, in our case, it controls the extent of droplet deformation. A third dimensionless number is the ratio between the strength of the thermodynamic and active anchoring. Dimensional analysis suggests that the strength of the thermodynamic anchoring, w_t, can be estimated as W/l_i, where l_i is an interfacial lengthscale. If the bulk energy density scale A and α are comparable (as in our simulations), we expect $l_i \sim \sqrt{\kappa/A}$ for $W \ll K$, and $l_i \sim \sqrt{WA}$ for $W \gg K$. On the other hand, as mentioned above, previous work has shown that the active anchoring can be estimated as $\sim \zeta l$, with l the lengthscale of elastic distortions in the polarisation field.

4.2 Anchoring-driven spontaneous rotation of extensile droplets

We begin by studying spontaneous rotations in a droplet of extensile active gel. In practice, the extensile case is relevant for bacterial colonies and for the "hierarchically assembled active matter" (made up of microtubules and molecular motors) in Ref. [60].

For the results in this section, we initialise the system with a circular extensile droplet in the centre of the simulation domain. The polarisation inside the droplet is uniform $|\mathbf{p}| = 1$, pointing vertically up along the y-direction: we refer to this as the "aligned initial condition". For extensile droplets, we also consider strong normal anchoring of the active dipole orientation at the droplet boundary (with anchoring strength $W = -0.05$). As we will briefly discuss below, we do not observe spontaneous rotations for extensile gel droplets with planar anchoring.

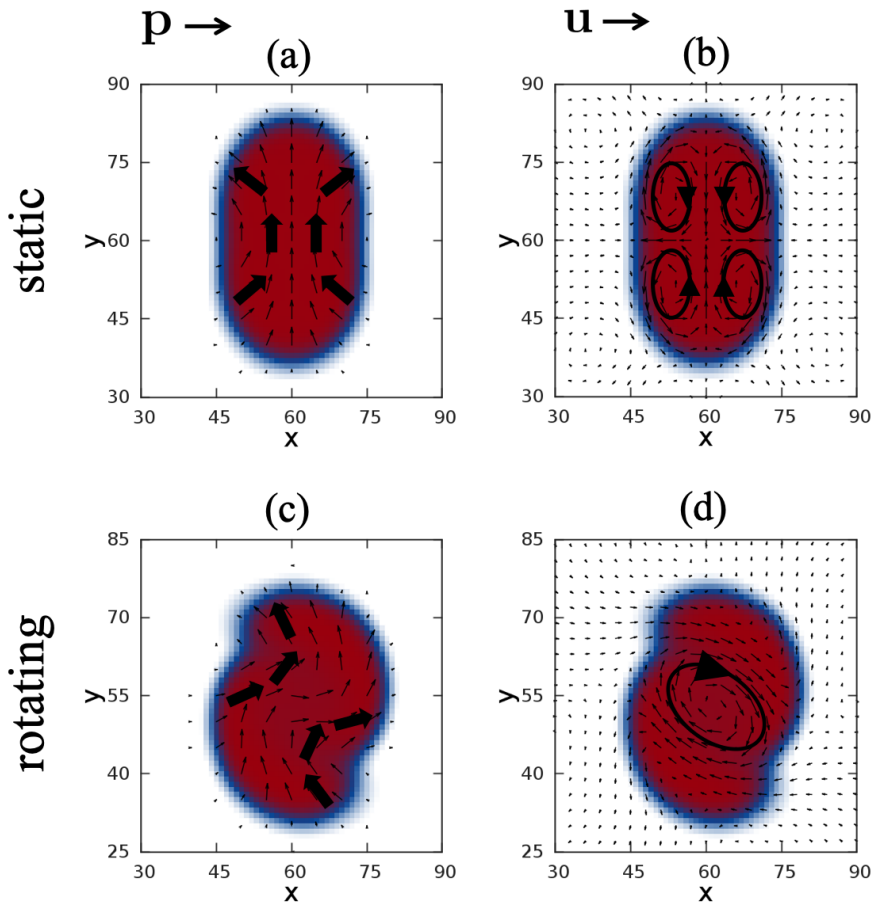

Figure 4.4 *Droplet polarisation and underlying flow field for an extensile droplet with strong normal anchoring and aligned initial condition. (a) and (b) show snapshots of $\boldsymbol{p}(x, y)$ and $\boldsymbol{u}(x, y)$, respectively, for a quiescent droplet with small value of the activity. (c) and (d) are snapshots of $\boldsymbol{p}(x, y)$ and $\boldsymbol{u}(x, y)$ for a spontaneously rotating droplet, corresponding to a large activity value.*

Figure 4.4 shows the steady state polarisation $\mathbf{p}(x, y)$ and corresponding flow field $\mathbf{u}(x, y)$ for an extensile droplet in different activity regimes. For small values of the activity, the droplet elongates slightly and becomes elliptical, with long axis along the direction of polarisation (Fig. 4.4(a)). While the droplet is static, there is an internal flow with the shape of four symmetric vortices (Fig. 4.4(b)): these flows are driven by the bend elastic deformations, present to accommodate the strong normal anchoring at the interface. For large enough activity, we find that the droplet substantially deforms (Fig. 4.4(c)) and can rotate spontaneously (Fig. 4.4(d), Suppl. Movie 4.1 [1]). In the spontaneously rotating phase, the

[1] All the movies referred to in this Chapter can be found in the Supplementary Materials on DataSync (`https://datasync.ed.ac.uk/index.php/s/AjP4ZfSEl07uHiV?path=%2F`), together with the online pdf version of this thesis. Appendix B contains a short description of all the Chapter 4 Suppl. Movies.

internal flow field has the topology of a single vortex (Fig. 4.4(d)). The sense of rotation of the droplet can be understood by looking at the patterns of bend deformation in the polarisation (Fig. 4.4(c)): these distortions lead to active forces which push the droplet in different directions, therefore creating an active torque which is responsible for the rotation (see also Fig. 4.15).

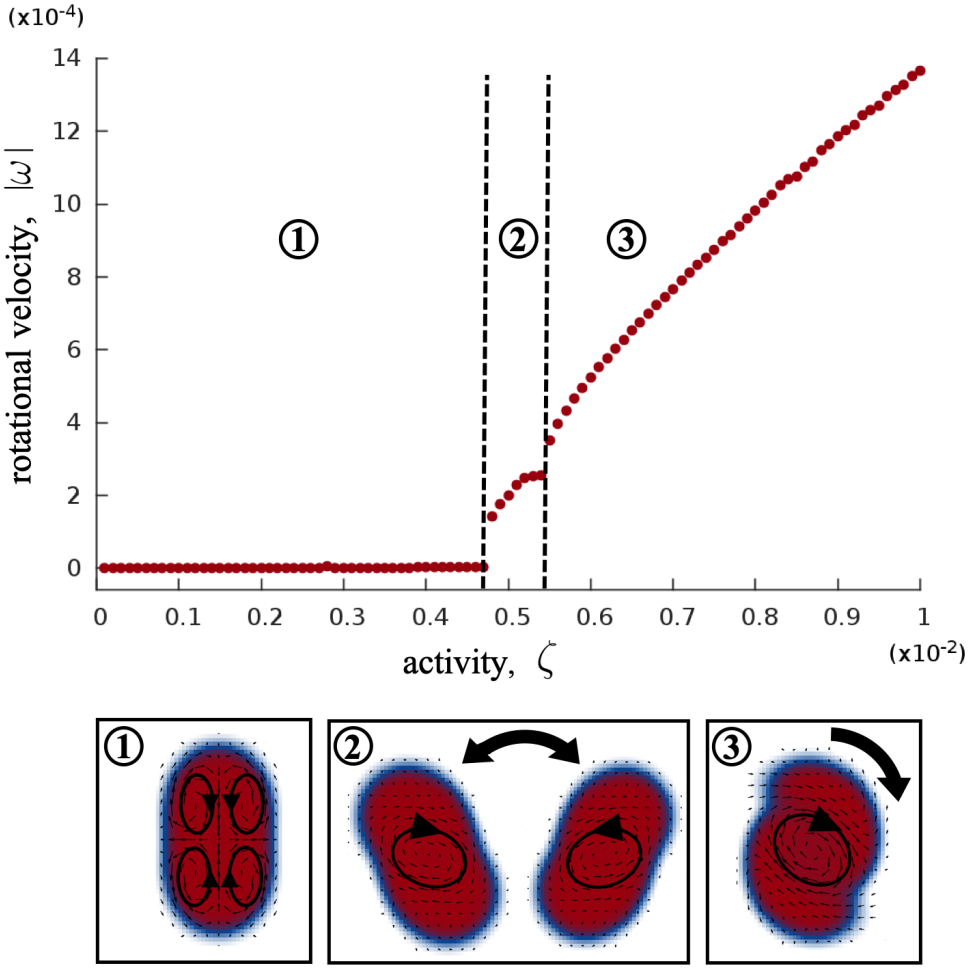

Figure 4.5 *Transition from a quiescent state with $\omega = 0$ to a spontaneously rotating state with $\omega \neq 0$ with increasing activity ζ, for an extensile active droplet with strong normal anchoring. 3 different regimes are shown: static (**1**), oscillation (**2**), and steady rotation (**3**).*

The transition between the elongated static phase and the rotating phase is depicted in Fig. 4.5. In the figure, we see see the rotational velocity ω of the droplet going from zero to a finite value, upon the increase of the activity parameter ζ. While we also monitor the average translational velocity, we find it is always zero (within numerical accuracy) in the whole range of activity explored.

Zooming in close to the transition between the quiescent and the steadily rotating phases, we find evidence of an intermediate regime (between $\zeta = 0.48 \times 10^{-2}$

and $\zeta = 0.53 \times 10^{-2}$ included) where the droplet oscillates, constantly switching between clockwise and anti-clockwise rotation (Fig. 4.5: area and cartoon **2**). This behaviour is reminiscent of oscillations found in bulk active fluids close to non-equilibrium phase transitions [48], and leads to regular and large oscillations in the rotational velocity (Fig. 4.6(a), Suppl. Movie 4.2). When switching between the two senses of rotation, the droplet is maximally elongated and minimally bent. While our simulations suggest that this switching may persist indefinitely, we cannot exclude the possibility that a strong enough fluctuation may drive the system into the spontaneously rotating phase. We do observe that sometimes droplet switching precedes steady rotation for larger ζ. Our results show that a large enough activity can spontaneously break symmetry to select a given sense of rotation. Even so, as ζ increases, we first observe a "stop-and-go" motion (e.g., for $\zeta = 0.054 \times 10^{-2}$, Suppl. Movie 4.3), and then a steadier motion where the amplitude of oscillations decreases with ζ (Fig. 4.6(b)).

Thus, extensile active droplets with strong normal anchoring can exist in one of three regimes: quiescent, oscillating, or steadily rotating, the intermediate oscillatory regime being stable for a small but finite range of activities. Both the transition between quiescent and oscillating states, and that between oscillations and steady rotations are signalled by a singularity in the rotational velocity plot (Fig. 4.5).

The onset of spontaneous rotation in active droplets appears to be qualitatively different from that of motility studied in Ref. [4]. For self-motile (translating) droplets, the transition is also associated with spontaneous symmetry breaking, yet it occurs without any intermediate regime in between the quiescent and spontaneously moving phases. Another important difference, of course, is that the self-motile droplets in Ref. [4] had no, or small, anchoring. Here anchoring is important: for small anchoring, we do not see any rotation. We will, therefore, refer to the observed spontaneous rotations as "anchoring-driven". Furthermore, normal anchoring is required for extensile droplets to rotate. Indeed, we find no spontaneous rotations when we impose planar anchoring of the active dipole polarisation at the droplet surface. Instead, we find that an extensile droplet with planar anchoring spontaneously translates as in Ref. [4]. It is important to note that the required combination of normal thermodynamic anchoring and extensile activity leads to a conflict between thermodynamic and active anchoring (as the latter is planar in this case [67]).

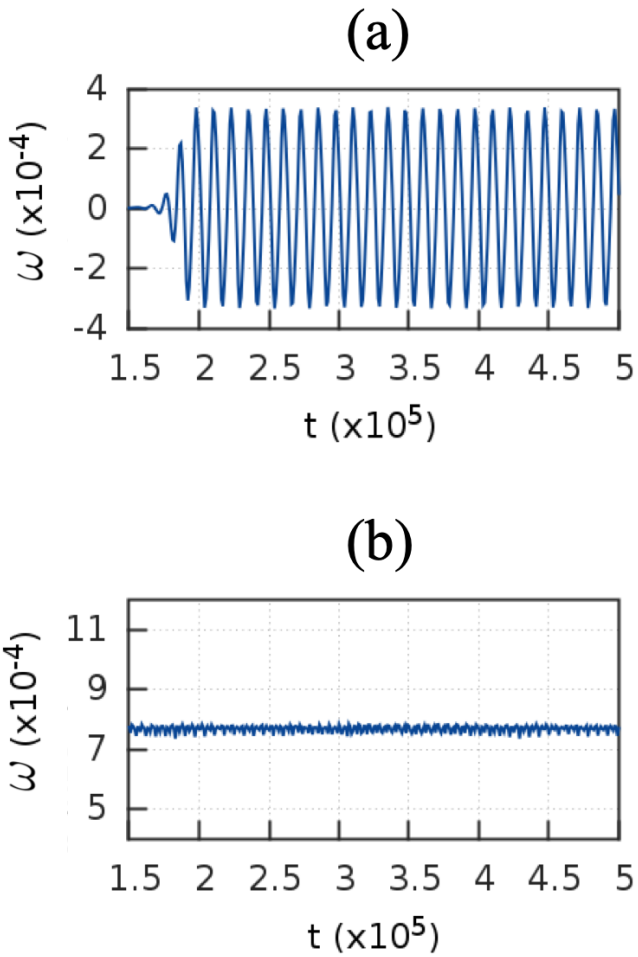

Figure 4.6 *Time dependence of the rotational velocity ω for $\zeta = 0.5 \times 10^{-2}$ (a), and $\zeta = 0.7 \times 10^{-2}$ (b). The first exhibits large oscillations in between positive and negative values which correspond to the oscillating regime (see Fig. 4.5 (2)). The second shows small variations around a higher value of ω, corresponding to the steadily rotating regime (see Fig. 4.5 (3)).*

4.3 Spontaneous rotation of contractile droplets

We next examine the case of a contractile droplet. Recall that this is a simple model for an actomyosin droplet, or cell extract. Contractile droplets can also display spontaneous anchoring-driven rotations. Interestingly, this time the required anchoring is planar. Once again, we highlight that this anchoring is required to contrast the active-induced anchoring, which for contractile gels is normal [67].

As in the previous section, we initialise the system with a uniformly aligned ($\mathbf{p}$ along the positive y-direction) circular active droplet.

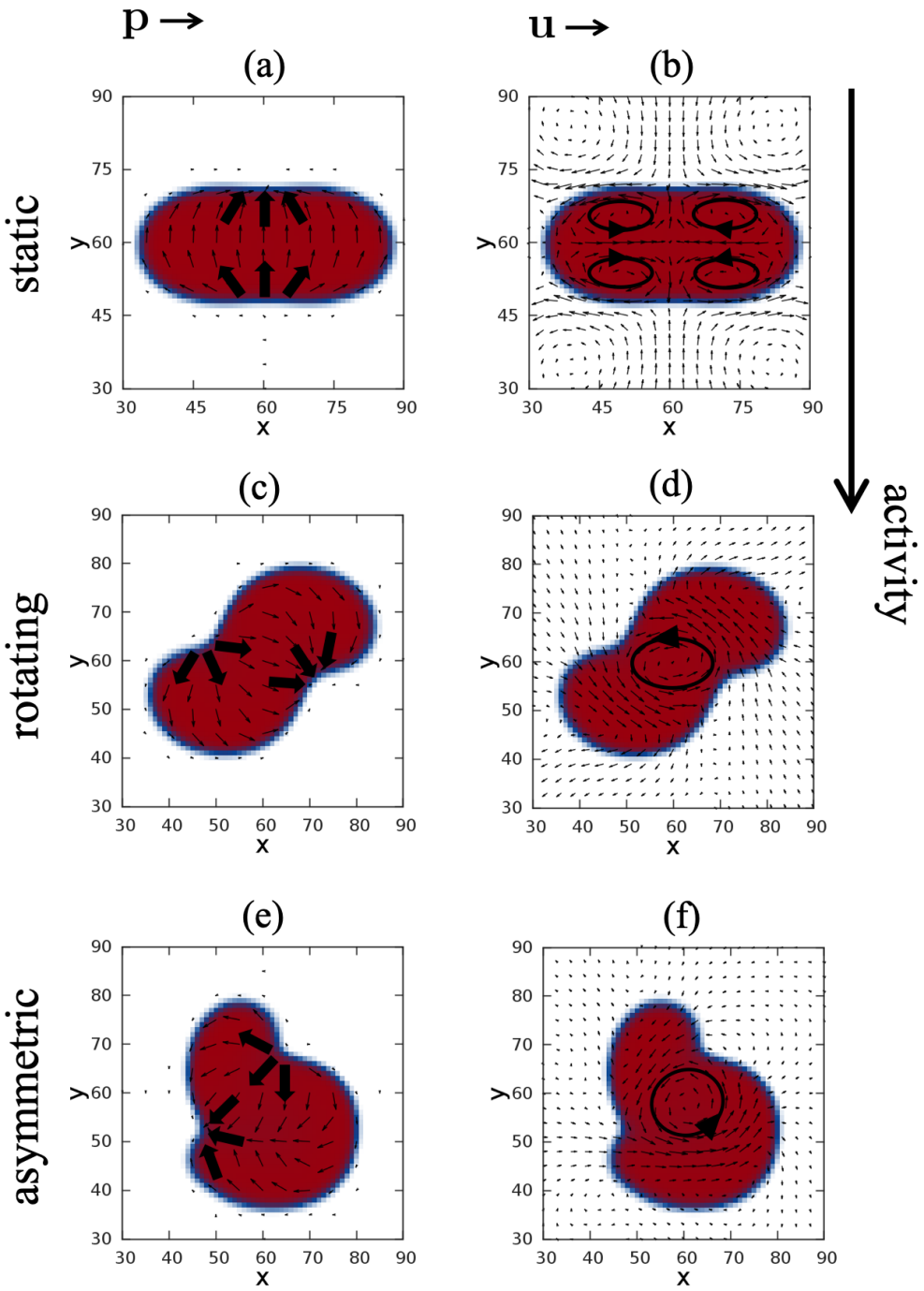

Figure 4.7 *Snapshots of droplet shape, polarisation* $\boldsymbol{p}(x, y)$*, and underlying flow field* $\boldsymbol{u}(x, y)$ *for a contractile droplet with strong planar anchoring. With the increase of activity, the droplet goes through a static (a)-(b), a spontaneously rotating (c)-(d), and an asymmetrically rotating (e)-(f) phase.*

Figure 4.7 shows the droplet orientational configuration and the flow field for three different steady state scenarios, upon increasing activity. For small activity, there is a quiescent phase, where the droplet is stationary, even if there is active flow inside (Fig. 4.7(b)). This is the analogue of the quiescent phase in the extensile case. Note that a contractile droplet extends perpendicular, rather than parallel, to the direction of polarisation (Fig. 4.7(a)). Second, for large enough activity, the droplet deforms into an "S" or "bean-shape" (Fig. 4.7(c)). In this regime, the droplet spontaneously rotates. The shape of the deformed droplet resembles that observed in the extensile case – this is therefore the contractile analogue of the anchoring-driven rotating regime (Suppl. Movie 4.4). In this regime, the internal flow has a vortex-like shape (Fig. 4.7(d)), again in analogy with the extensile case. However, now the active torque is provided by splay, rather than bend, deformation patterns (Fig.4.7(c)). Finally, for even larger activity, we observe an asymmetric droplet which is revolving around a point distinct from its centre of mass (Fig. 4.7(e)-(f), Suppl. Movie 4.5). The mechanism for the rotation in the asymmetric phase is the same as for the symmetric one: an internal vortex flow powered by two splay deformations. The asymmetry arises when the activity is large enough in comparison to the surface tension, allowing for further shape deformations as the observed in Fig. 4.7(e)-(f).

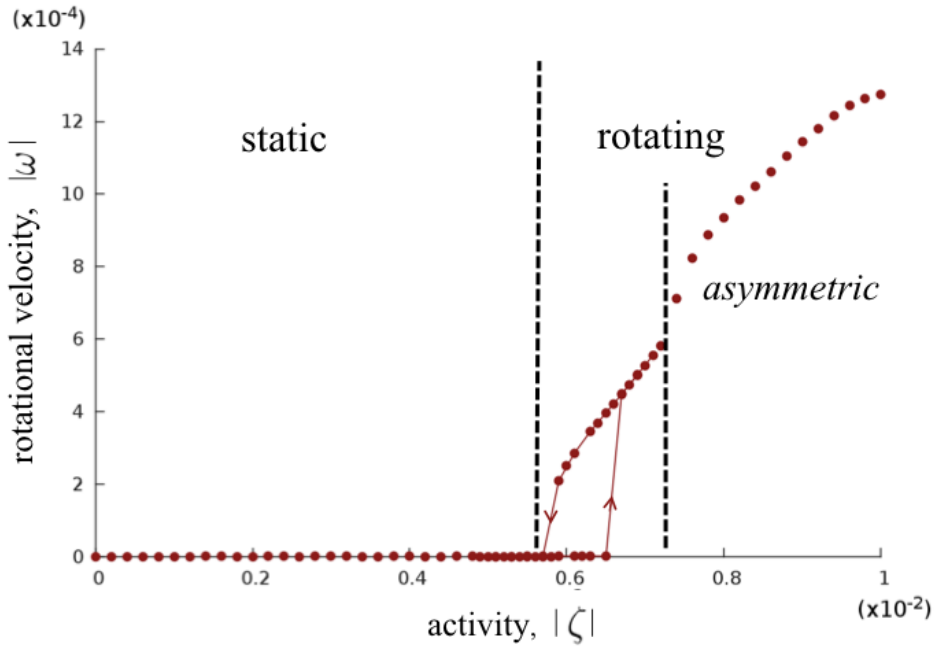

Figure 4.8 *Transition between static and rotating regimes for a contractile droplet with strong planar anchoring. The rotational velocity exhibits hysteresis with the contractile activity, characteristic of a discontinuous non-equilibrium transition.*

The transition between quiescent and spontaneously rotating phases is characterised quantitatively in Fig. 4.8. As in Fig. 4.5 for extensile droplets, we show the variation of the rotational velocity $|\omega|$ with contractile activity $|\zeta|$ (note that within our formalism ζ is negative for contractile active gels). To generate the rotational velocity curve shown in Figure 4.8, we simulated a hysteresis loop whereby the activity is first ramped up and then turned down. (In practice, each simulation is initialised with the steady state conformation obtained in the run with the neighbouring value of the activity.) The fact that there is hysteresis suggests that the transition between the quiescent and rotating phases is discontinuous, or first-order-like. With respect to the extensile case, there is no oscillatory droplet regime, but instead a window of activities where the droplet either steadily rotates (top branch) or does so only transiently and is static at later times (bottom branch). Therefore, in both contractile and extensile droplets there is an intermediate regime characteristic of proximity to a non-equilibrium transition, however these regimes are different for the two types of activities. This might seem surprising at first glance, but there is actually no reason to expect the two systems to behave in the same way as there is no exact mapping between them. The additional singularity at larger ζ corresponds to the transition between the symmetric and asymmetric rotating states (Figs. 4.7(c) and 4.7(e) respectively).

Previous work in quasi-1D active nematics [69] showed that extensile and contractile systems can be exactly mapped into each other by a simultaneous change in sign of ζ and ξ, accompanied by a rotation of the polarisation field by $\pi/2$. In this work contractile and extensile droplets behave differently as we study rodlike systems ($\xi > 0$) in both cases. Still, there is an approximate mapping between extensile droplets with normal anchoring and contractile droplets with planar anchoring. The same is true between extensile droplets with planar anchoring and contractile ones with normal anchoring (as discussed in Fig. 4.15 below).

4.4 Anchoring-driven rotations are associated with shape deformation

Our observations of spontaneous active droplet rotation are not the first to be reported in the literature. Kruse *et al.* discuss a mechanism leading to

spontaneously rotating spiral and aster defects [70, 71]. It is then relevant to ask whether the mechanism leading to the rotation of extensile and contractile droplets in sections 4.2 and 4.3 is related to these previous reports.

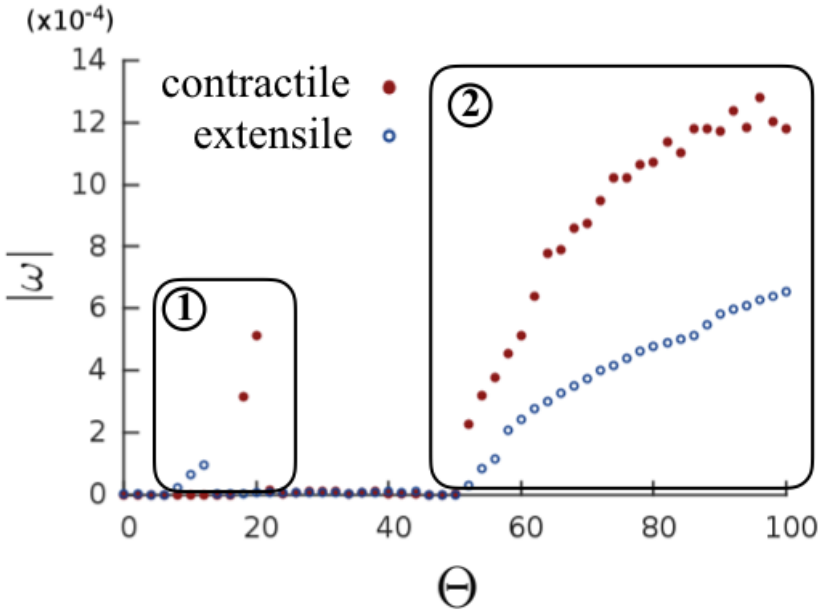

Figure 4.9 *Rotational velocity for contractile and extensile droplets as a function of the dimensionless parameter* $\Theta = \zeta R^2/K$. *For both types of droplets, there are two branches with* $|\omega| \neq 0$. *The first branch (**1**) corresponds to circular rotating spirals (for extensile droplets - see Fig. 4.10(a)) and asters (for contractile droplets - see Fig. 4.10(b)); the second branch (**2**) corresponds to anchoring-driven rotations of bean-shaped droplets (see Figs. 4.5 and 4.7).*

In the case of spirals and asters, rotations occur within a circular domain – i.e., the surface tension is effectively infinite; also, again, there is no intermediate regime between the quiescent and the spontaneously rotating phases. Another important difference is that the theory in Ref. [70] does not include any anchoring: spontaneous rotation of these spirals is therefore triggered by activity alone, and hindered by elasticity. Correspondingly, the key dimensionless parameter was identified as $\Theta = \zeta R^2/K$, which also regulates the transition between quiescent and self-motile droplets in Ref. [4].

In our work, we looked for rotating spiral states and found them to be present for values of ζ below the critical threshold for rotation in bean-shaped droplets. Figure 4.9 shows a plot of the rotational velocity $|\omega|$ for both contractile and extensile droplets, as a function of the dimensionless parameter Θ. In Fig. 4.9 we explore the same systems as in Figs. 4.5 and 4.8, but we initialise the droplets

with a spiral (extensile) or an aster (contractile) configuration to ascertain if those states are stable. For both activity types, there is a first branch where $|\omega| \neq 0$ for low Θ. That first branch corresponds to spiral and aster rotating states. Spirals occur for extensile droplets (see Fig. 4.10(a)) and asters occur for contractile droplets (see Fig. 4.10(b)). A second branch exists for higher Θ which corresponds to the anchoring-driven rotations described above (in these rotations, the droplet shape is non-circular, see Figs. 4.5 and 4.7). Because we simulated droplets with a finite surface tension, when the activity is high enough, the droplet shape becomes unstable to deformations and starts to follow the contours of the internal elastic deformations. The result is a bean-shaped droplet that rotates due to the imposed anchoring. For high values of the activity, the bean-shaped droplet is the observed steady state.

Figure 4.10 depicts the spiral rotating droplets in steady state. Extensile droplets rotate due to bend deformations, generating a spiral configuration (Fig.4.10(a)), while contractile droplets are driven by splay deformations and have an aster polarisation profile (Fig.4.10(b)). The fluid flow is, in both cases, a single internal vortex (Fig.4.10(c)).

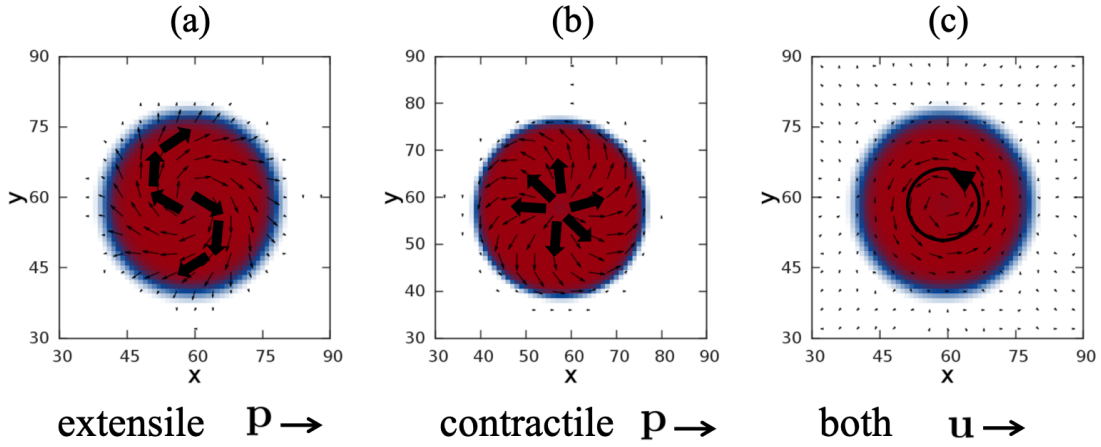

Figure 4.10 *Rotating circular droplets. (a) Spiral extensile droplet (with strong normal anchoring). (b) Aster contractile droplet (with strong planar anchoring). (c) Vortex flow for both extensile and contractile circular rotating droplets. In (a) and (b), the arrows represent the polarisation inside the droplet (with larger arrows for easier visualisation). In (c) the arrows represent the fluid flow in the anti-clockwise direction (see larger arrow).*

Since the type of anchoring does not seem to affect rotating spirals and asters (the internal deformation can remain the same whether planar or normal orientations are imposed), we chose to maintain the strong anchoring of the previous sections: normal for extensile droplets and planar for contractile droplets.

As mentioned above, for finite surface tension and high activity, spiral states become unstable to droplet deformations. To study spiral states in more detail for a wide activity range, we initialised our droplets as a spiral (extensile droplets) or an aster (contractile droplets) and slowly ramped up activity. As expected, we found that the threshold for rotation scales with the elastic constant K linearly. This was verified for both extensile spirals and contractile asters. Furthermore, we observe the collapse of the curves for different values of K when we plot the scaled quantities: $|\omega|/K$ as a function of Θ (see Fig. 4.11).

This scaling is *not* obeyed for the case of aligned initial condition and bean-shaped droplet rotation. In Fig. 4.12 we show the corresponding plot for an extensile droplet. The same conclusion is reached for contractile droplets which are difficult to visualise due to their hysteresis. The threshold beyond which we observe spontaneous rotations does not simply scale with K in a linear fashion (i.e., the transition points do not coincide when plotted versus Θ). The deviation is especially visible for the larger values of K ($K = 0.06$ and $K = 0.08$). In these cases, the oscillating droplet regime is found for a larger range of activities; for $K = 0.08$, in particular, the stop-and-go rotation is also more prominent and leaves a signature in the rotational velocity curve so that there are three, rather than two, discontinuities. For the larger activities there are also less internal elastic deformations, and a much stronger active interfacial flow in the steadily rotating phase with respect to the cases of $K = 0.02, 0.04$.

Therefore, the mechanism leading to spontaneous rotation of our droplets is qualitatively different from that analysed in Ref. [70], although they both require spontaneous symmetry breaking. Two main factors explain the difference. First, unlike the rotating spirals, our rotations are also typically associated with significant deformations of the droplet shape. Bean-shaped rotating droplets are the observed state for systems with finite surface tension and high enough activity. Secondly, a specific type of anchoring is required. The anchoring needs to be strong enough to oppose the active effect on the interface. The latter is behind our choice of naming such rotations "anchoring-driven rotations".

In summary, our rotating droplets depend on a non-trivial combination of all four factors: activity ζ, elasticity K, surface tension κ, and anchoring strength W. The competition between activity and elasticity controls the onset of the bend and splay instabilities responsible for spontaneous flows. However, this is not the full picture. The competition between activity and surface tension determines the droplet shape. Anchoring-driven rotations occur only with significant shape

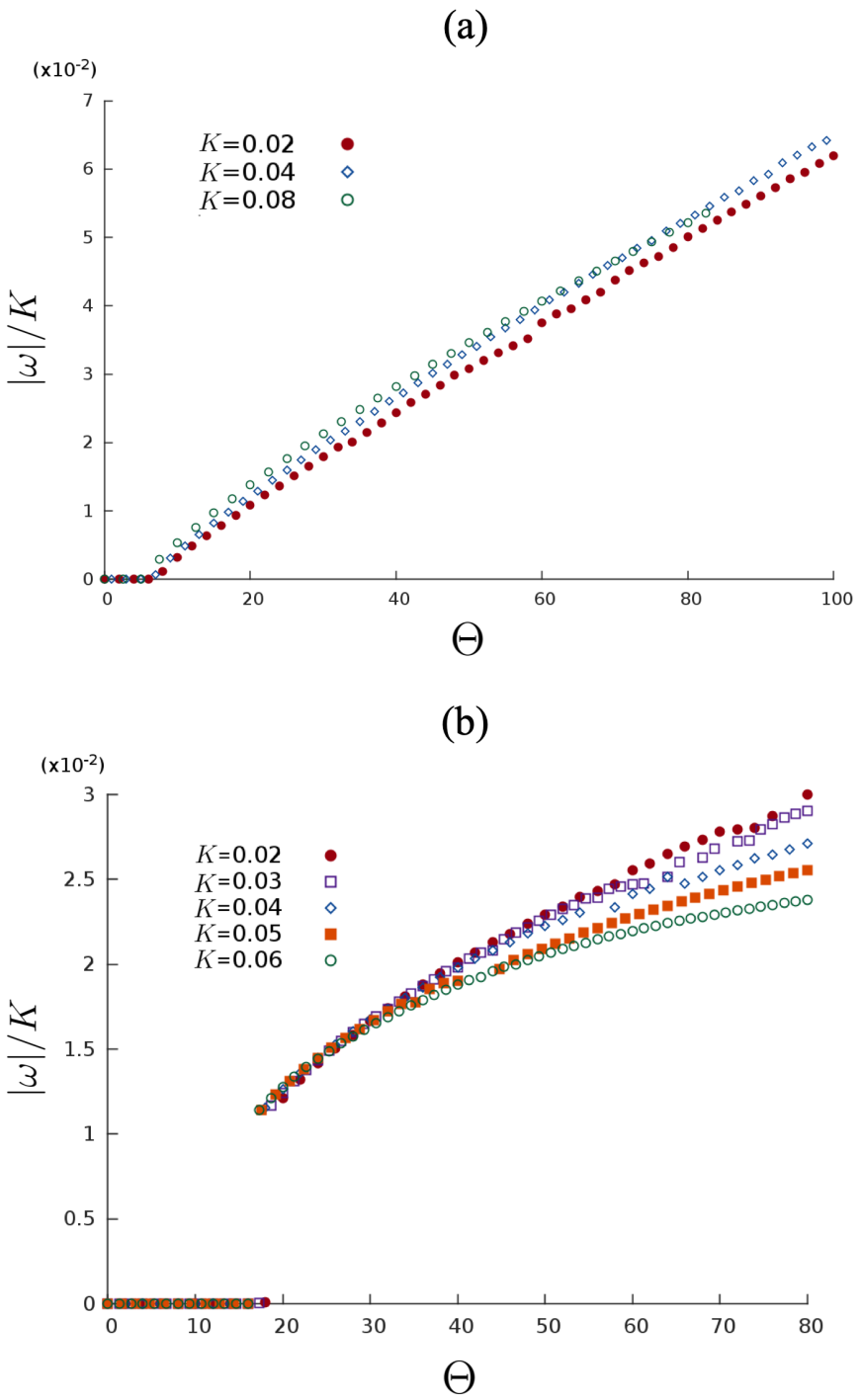

Figure 4.11 *(a) Transition to a spiral rotating state for an extensile droplet with different elasticity constants. (b) Transition to an aster rotating state for a contractile droplet with different elasticity constants. For both types of droplets, the transition curves collapse when plotted against the dimensionless parameter* $\Theta = \zeta R^2/K$. *This indicates that the transition depends only on the competition between activity and elasticity. These figures were produced by the same method as Fig. 4.8: slowly ramping up the activity from the previous configuration. Here, unlike in Fig. 4.8, we used a spiral (extensile droplets) and an aster (contractile droplets) as initial configurations.*

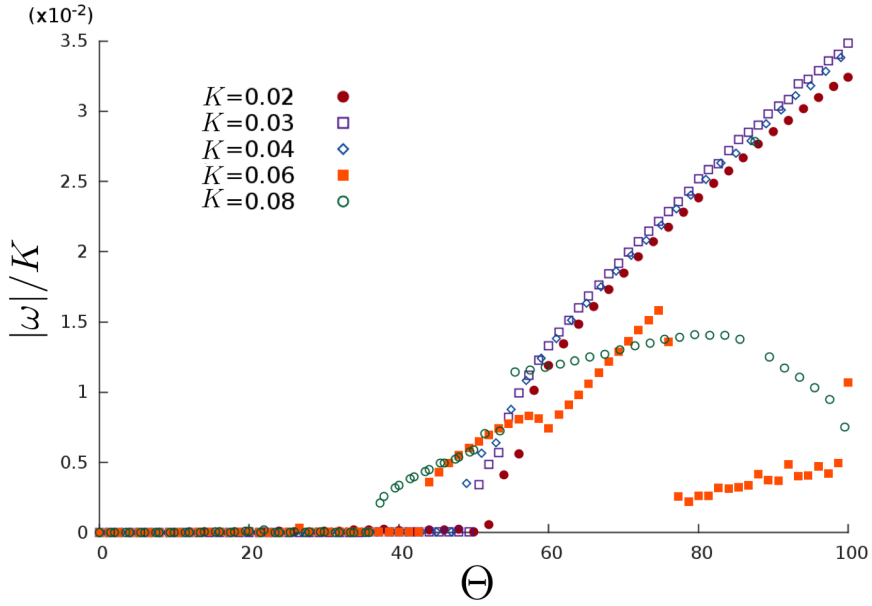

Figure 4.12 *Scaling of the transition to a bean-shaped rotating state for different values of the elasticity constant. The transition does not depend only on the activity and elasticity parameters. Surface tension and anchoring strength also play a role in the transition.*

deformation. Also, the thermodynamic anchoring is required to be higher than the active one. In the next section we study the anchoring dependence of the rotations.

4.5 The significance of the anchoring: switching between translation and rotation

As highlighted above, our spontaneous rotations are anchoring-driven: extensile rotations require normal anchoring, contractile rotations require planar anchoring. Besides the nature of the anchoring, it is important to characterise the dependence on its strength, and that is what we do in this section.

We first consider the case of extensile droplets. Figure 4.13 plots the rotational and translational velocities as a function of the strength of normal anchoring, W, for a fixed value of the extensile activity (large enough to create spontaneous rotations in Fig.4.5). If W is small, we observe little or no rotation: in this regime there is still motion, but in the form of translations. This is the regime of self-motile droplets studied in Ref. [4], where bend deformations drive active flows which power the motion of the droplet. Activity drives an effective planar

anchoring at the surface (see left snapshot **1** in Fig. 4.13). If W increases past a critical threshold, translatory motion arrests and we enter the previously studied spontaneously rotating regime (snapshot **2** in Fig. 4.13).

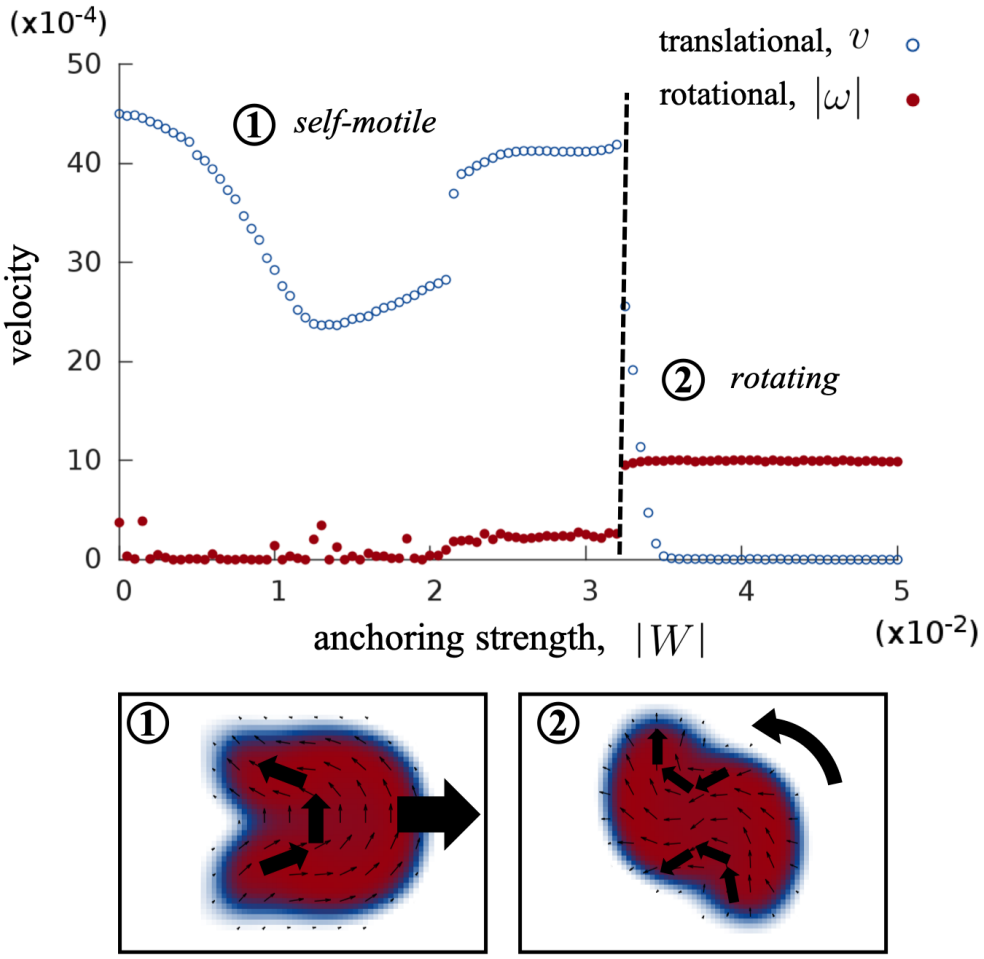

Figure 4.13 *Plot of the rotational and translational velocities for an extensile droplet with variable W, strength of normal anchoring. For small W, the droplet mainly translates (**1**), whereas it mainly rotates for large W (**2**).*

These results therefore suggest that in order to observe anchoring-driven rotations we need a large enough value of both Θ and W. This is in contrast to both the self-motile translating droplets of Ref. [4] and the rotating spirals of Ref. [70] which solely require a large value of Θ.

Next, we analyse contractile droplets with planar anchoring (Fig. 4.14). These simulations confirm the qualitative trend found in the extensile case, as rotations only occur for a sufficiently large value of W. However, here the picture is more complex. First, in the rotating regime, as previously discussed, the droplet may develop a shape asymmetry (Fig. 4.7(e)), which leads to a non-zero value of the

translational velocity of the centre of mass. Second, in the non-rotating phase, we observe irregular motion, rather than steady translation as for the extensile case. This is possibly due to the smaller value of the surface tension used (with respect to extensile droplets). As a result of this choice, which is due to reasons of numerical stability, the droplet largely deforms in the low W regime, and can accomodate multiple splay elastic deformations which are likely to be responsible for the more complex dynamics. The contractile results also highlight a large variability in the observed rotational and translational velocity, due to different random noise in the initial condition.

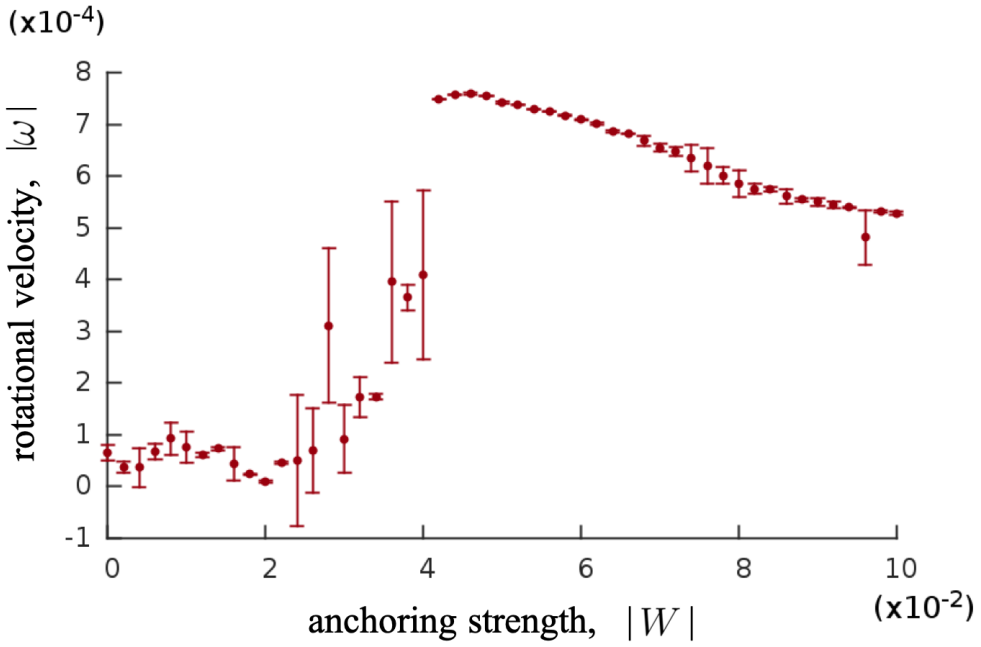

Figure 4.14 *Plot of the rotational velocity for a contractile droplet with planar anchoring. In this case fluctuations are larger, hence we have averaged over 10 realisations (each initialised with a different random polarisation pattern). Error bars represent the standard deviation associated with each average calculation.*

A possible explanation of these results is that, as previously hinted, droplet rotations require a thermodynamic anchoring which conflicts with the active anchoring (see cartoon in Fig. 4.15). Consider for concreteness the case of an extensile droplet. In the absence of any conflict, or when active anchoring wins, the droplet can settle into a structure consisting of a single bend deformation, whose geometry is similar to that of the droplets in Ref. [4] and consistent with steady translation (but no rotation, see Fig. 6(a)). Instead, in the presence of a conflict, the anchoring can stabilise a different pattern of polarisation inside the droplet, with two bend deformations of opposing sense: this in turn can create

the torque required for the active rotation (Fig. 4.15(b)). Flipping the sign of ζ, and replacing bend with splay, a similar reasoning explains the behaviour of contractile droplets (Figs. 4.15(c),(d)).

Consequently, we speculate that an important dimensionless number to describe rotations should be the ratio between the effective thermodynamic and active anchoring. The effective thermodynamic anchoring can be estimated as $w_t = W/l_i$, where W is the anchoring strength entering in our free energy density (which has units of N), and l_i is the interfacial thickness. The active anchoring can instead be estimated as $w_a \sim \zeta l_a$, where l_a is an active lengthscale characterising the size of splay-bend distortion within an active nematic [11]. A more quantitative test of this expectation is here hampered by the fact that the droplet behaviour does not only depend on $w_t/_a$, but also on Θ and the active capillary number.

4.6 Concluding remarks

In summary, we have shown here that active droplets with sufficiently strong thermodynamic anchoring show a transition between a quiescent phase and one where droplets rotate spontaneously. This behaviour contrasts with that of active droplets without thermodynamic anchoring, where the transition is instead between a quiescent and a self-motile (and non-rotating) phase [4, 11]. Our spontaneously rotating droplets are fundamentally distinct from the rotating spirals of [19, 70], as the latter arise even with no anchoring at all, and infinite surface tension.

A schematic representation of the mechanism leading to the anchoring-driven rotations we observe is drawn in Figure 4.15. For instance, in extensile droplets normal anchoring stabilises two regions of bend distortions: these are associated with two local active forces with opposing direction. When the two forces are not collinear, for instance due to a fluctuation, they create an active torque which rotates the droplet. The elastic distortions are accompanied by deformations in the surface. Importantly, the anchoring is required to maintain two symmetric regions of bend: when it is absent, there is only one deformation in steady state, and the droplet translates (Fig. 4.15(b)). Similar reasoning explains qualitatively why contractile droplets with planar anchoring also rotate (Fig. 4.15).

The morphology and kinetics of our spontaneously rotating droplets is very varied,

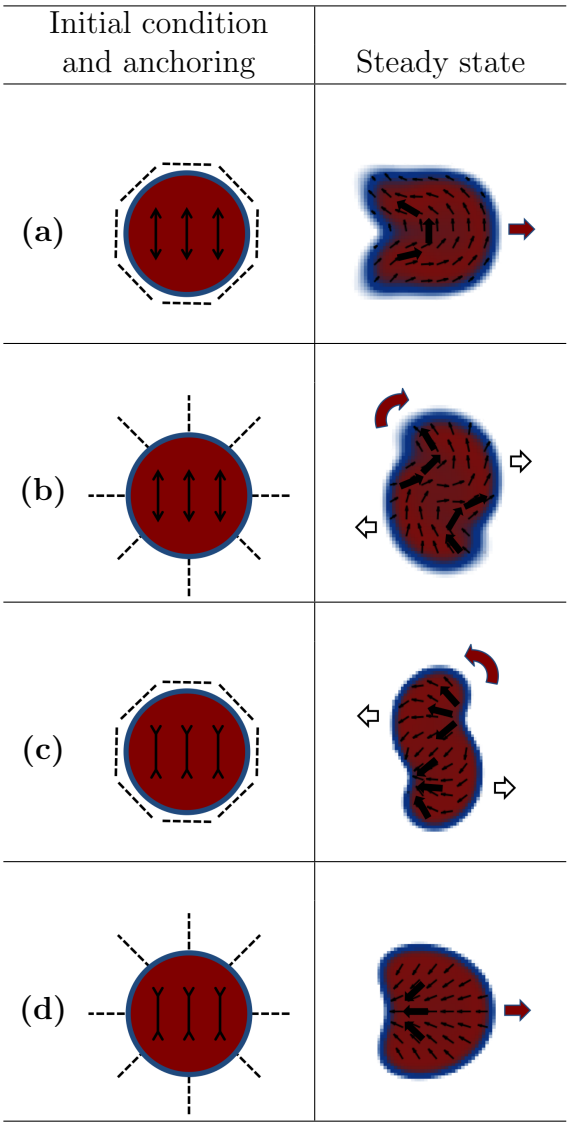

Figure 4.15 *This cartoon illustrates the interplay between anchoring and activity to determine the dynamics of our active gel droplets. Extensile droplets (a) and (b)) rotate with normal anchoring (b), because this anchoring stabilises a pair of bend deformations which creates a sustained active torque (here leading to clockwise rotation). Instead, planar anchoring or no anchoring (represented as dashed lines in (a)) leads to a single bend deformation, a pattern compatible with translational motility. Similar considerations apply to contractile activity (rows (c) and (d), see text). Red arrows represent the overall sense of movement while black and white arrows represent flows generated by each deformation.*

and can be controlled by a number of parameters. For instance, we can slow down or arrest rotation by decreasing anchoring strength. Close to the transition between rotating and motile droplets, we also find more exotic dynamics: an example is given in Suppl. Movie 4.6 where the droplet alternates between motile spells and partial rotations. Surface tension and elasticity have a further important effect, as they control the pattern of the active flow, which can be maximal in the droplet interior or at the surface.

An important question is what a suitable system to recreate these results in the lab might be. We suggest that a good candidate may be an emulsion incorporating the hierarchically assembled active matter described in [60]. This system is made up by oil-water emulsions where the water component contains suspensions of microtubule, polyethylene glycol (PEG) and kinesin motors. Due to the presence of PEG, there are depletion interactions which cause microtubules to stick to each other to form bundles, and motor activity causes such bundles to slide antiparallel to each other, creating extensile active dipolar forces. A difference with our model is that in the experimental system the order is nematic (*i.e.*, active particles are invariant under a $\mathbf{p} \rightarrow \mathbf{-p}$ inversion), rather than polar. However, by carrying out simulations of an active droplet where the active phase is nematic (the simulation method is the same which was discussed in Ref. [67]), we have found that such spontaneous rotations occur in that case as well, with only minor differences to the case reported here (see Suppl. Movies 7 and 8). Therefore, the physics we observe here in two-dimensional droplets should in principle apply to the apolar material described in Ref. [60]. We should note, however that the same might not be true in a fully three-dimensional system. While the physics describing the elastic deformations and stresses they generate is the same, in nematic systems half-integer defects are possible. In three-dimensional contractile droplets this plays an important role since the Poincare-Hopf theorem determines that the topological charge for a vectorial field on the surface of a sphere must be +2. Such topological charge is distributed in two +1 defects for a polar droplet, but can be distributed, for instance, either into two +1 or into four $+\frac{1}{2}$ defects for a nematic one. This means that polar and nematic three-dimensional contractile droplets are easily distinguished. It will be of interest to study 3D droplets in the future to find what the consequences of the different defect topologies are.

We also highlight that some more practical challenges would need to be addressed before spontaneously rotating droplets can be self-assembled in the lab, as experimental studies in the literature report the formation of an active

microtubule-kinesin shell, rather than a uniformly filled droplet, and the natural anchoring in those extensile systems normally is planar – this is favoured as a consequence of the microtubule rigidity. Notwithstanding these issues, we hope that our results will stimulate experiments on the self-assembly of active soft rotators in the future, based on either active gels or alternative designs.

Chapter 5

Emergence of a nonequilibrium cholesteric phase in active torque systems

In chapter 4, we showed that active gel droplets with strong interfacial anchoring undergo a transition into a rotating dynamical regime. The transition is a manifestation of the known hydrodynamic instabilities for active gels. When the active stresses on the fluid are strong enough, bend and splay deformations generate macroscopic directional flows capable of pushing the entire droplet into a variety of motile states. The anchoring acts as a constraint to stabilise two deformations opposed in direction, powering the torque responsible for droplet rotation (see Fig. 4.15). The droplet can rotate either clockwise or anticlockwise, since the sense of rotation is selected randomly via spontaneous symmetry breaking.

Further cases of spontaneous rotational or chiral symmetry breaking have been reported in the literature in diffusiophoretic nematic droplets [72], active nematic shells [73], and swimmer aggregates [74], to name only a few. Note that, in all the examples above, the systems lack any microscopic chirality and start rotating due to collective aggregation and orientational effects.

However, the vast majority of biomolecules - and the structures they form - are chiral. Thus, most biological active systems are, in fact, intrinsically chiral at the micro-scale. This is the case of both actomyosin networks and bacterial

suspensions, as we describe below.

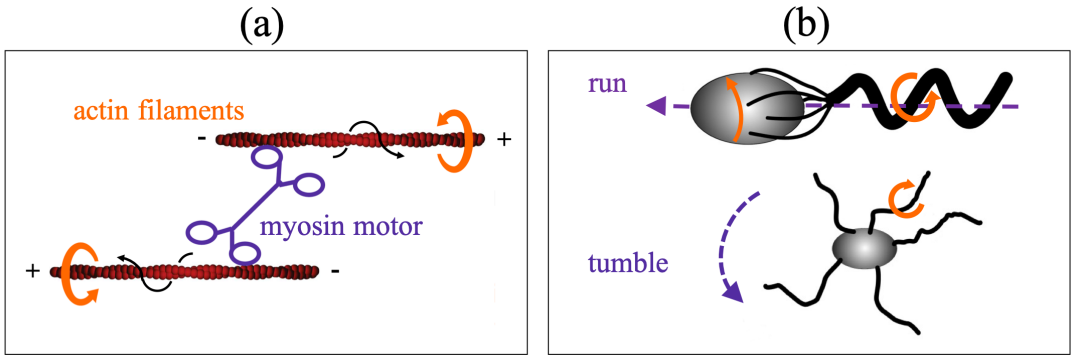

Figure 5.1 *Active torque dipole generation in actomyosin (a), and swimming E. coli (b). (a) Since actin is a right-handed helix, the myosin motor describes a helical path when translocating along the chiral filaments. As a result, the actin filaments counter-rotate relative to each other and generate a torque dipole. Figure adapted from [12]. (b) "Run" (top) and "tumble" (bottom) motion modes in E. coli bacteria. During a "run", the left-handed flagella rotate coherently anticlockwise, while the body rotates in the opposite direction. This gives rise to a torque dipole. In the "tumble" mode, each flagellum rotates incoherently clockwise, causing the cell body to spin. Figure adapted from [13].*

In the cytoskeleton, both microtubules and actin filaments possess an intrinsic handedness. Therefore, their interaction with motors (e.g. dyenin, myosin) is chiral and must generically result in active rotation [12, 75]. Let us revisit the case of actomyosin, which we have already used as a paradigm for contractile activity. As we have seen in chapter 1, contractile stresses are generated when a myosin motor attaches to a pair of anti-parallel actin filaments and "walks" towards the positive ends, pulling the filaments inwards. Since actin is structurally a right-handed helix [76], the motor describes a helical path while translocating along it (see Fig. 5.1(a)). This causes the filaments to rotate, as well as translate. During this movement, the two filaments rotate in opposite directions because they have opposite orientations. It is the counter-rotation of the actin filaments that leads to the presence of a torque dipole. This is in addition to the contractile force dipole, which results from the filaments being pulled in by the myosin.

The self-organisation of the chiral actomyosin cortex has been linked to the intriguing phenomenon of left-right symmetry breaking in developmental biology [75, 77–79]. Plenty of instances of left-right asymmetry can be found in the animal world including the internal organs (heart, lungs, etc.) of vertebrates, the human brain, *C. elegans* intestine [80], and mollusc shells (such as snails).

Henley [81] uses symmetry arguments to propose that a microscopic chiral bias is necessary, whatever the mechanism responsible for the symmetry breaking. Cytoskeletal filaments are obvious candidates for initiating left-right asymmetry as they have a defined polarity and handedness. Yet, the specific process by which microscopic chirality translates to the cellular level, and to the entire organism, remains elusive.

Other examples of active chiral systems are provided by suspensions of microswimmers, such as *E.coli*, which move through the fluid using the helical shaped flagella located at their rear [13]. As discussed in chapter 1, *E.coli* has a "run-and-tumble" type of motion. During the "run" mode, the motors embedded in the cell membrane rotate the flagella anticlockwise. Since each of the flagellum filaments is a left-handed helix, they bundle together and screw through the medium producing a more or less straight movement. While the flagella rotate in one direction, the cell body rotates more slowly in the opposite sense to balance the torque produced. Thus, a torque dipole is generated. Note that swimming *E. coli* also pushes the fluid outwards along the swimming direction, which results in an extensile force dipole. The motors can also randomly switch to clockwise motion, causing the bundle to separate and each isolated flagellum to rotate in an uncoordinated way. This is know as a "tumble", during which the cell randomly switches direction. The two modes of movement, and the corresponding rotation of the flagella and cell body, are depicted in Fig. 5.1(b).

In both biological examples presented above, the chiral microscopic structure has implications for the overall organic function. In actomyosin it affects the intracellular organisation (and is linked to left-right asymmetry), while in flagellated bacteria it allows space exploration during chemotaxis (through spells of straight motion intercalated by random changes in direction). Thus, it becomes abundantly clear that a complete hydrodynamic theory of biological active fluids must include such chiral effects.

That is the topic of the present chapter. We introduce chirality through the torque dipole approximation and show, via coarse graining, that the resultant active stress on the fluid is chiral. Through a combination of linear stability analysis and computational simulations, we investigate the effect of the active chiral stress. For simplicity, we concentrate only on chiral activity and set the achiral active stresses to zero. Our results show that, above a critical threshold of the chiral activity, the active fluid starts to twist spontaneously into a helical pattern, resembling cholesteric liquid crystals. Because there

is no cholesteric or chiral contribution in the equilibrium free energy, we call the twisted phase "self-assembled nonequilibrium cholesteric". We characterise the non-equilibrium transition and the twisted steady states in both quasi-1D and quasi-2D configurations of active torque dipoles. In quasi-2D systems we find, in addition to purely twisted configurations, fingering patterns and even a turbulent regime. Finally, we compare our twisted phase with a "dry" system of torque dipoles, *i.e.* without momentum conservation, to address the role of the underlying fluid in the transition.

5.1 Derivation of the chiral active stress

We will now derive the form of the active stress exerted on the fluid due to chiral active effects.

We choose to approximate each active particle by a torque dipole. The torque dipole is the lowest order chiral contribution in the hydrodynamic multipolar expansion for a neutrally buoyant particle [82]. A torque dipole is also effectively a force quadrupole [83], meaning that its far-field flow decays with distance as $u \sim 1/r^3$, while that of a force dipole decays as $u \sim 1/r^2$.

The method we use here for the derivation is the same we used in section 2.3 for the force dipole approximation. We take an ensemble of N torque dipoles and proceed by coarse graining the local torque density.

Figure 5.2 represents left and right handed dipoles schematically. We can use the opening and closing of a bottle cap as an analogy for the flows around these particles: a left-handed dipole corresponds to the opening of the bottle (Fig. 5.2 (a)), and a right-handed dipole to the bottle closing (Fig. 5.2 (b)).

Following the representation of Fig. 5.2, we can write down the torque exerted by particle i:

$$\boldsymbol{\tau}\left(\mathbf{r}\right) = \pm\left[\tau\hat{\nu}_i\delta\left(\mathbf{r}-\mathbf{r}_i-\frac{l}{2}\hat{\nu}_i\right)-\tau\hat{\nu}_i\delta\left(\mathbf{r}-\mathbf{r}_i+\frac{l}{2}\hat{\nu}_i\right)\right] . \tag{5.1}$$

In Eq. (5.1) we take particle i to have center of mass positioned at $\mathbf{r}_i$, the half-way point along its length l (homogeneous particle), orientation $\hat{\nu}_i$, and torque dipolar strength τ. The + sign corresponds to a left-handed dipole (Fig. 5.2 (a)), and

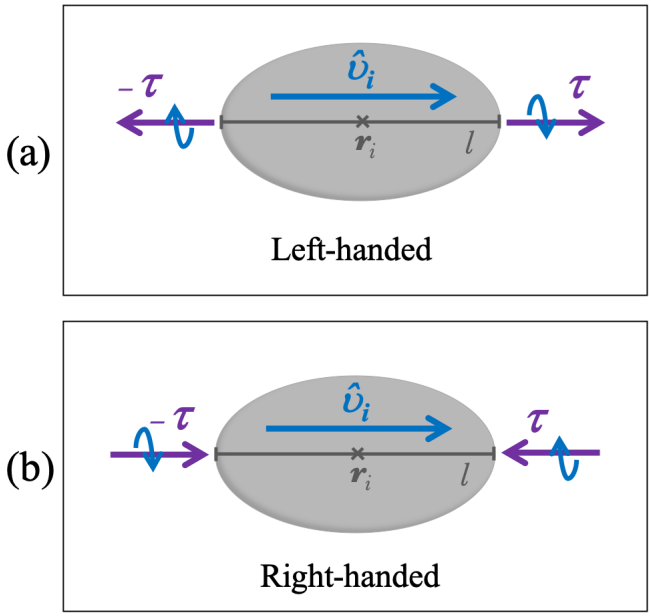

Figure 5.2 *Schematic representation of a left-handed (a), and a right-handed (b) torque dipoles. The direction of the torque dipole coincides with the orientation of the active particle. The two torques are represented in purple and the generated fluid flows in blue.*

the $-$ sign to a right-handed one (Fig. 5.2 (b)). We consider only the situation where the torque dipole is parallel or anti-parallel to the orientation $\hat{\nu}$. Although a more generic derivation would consider cases where the torque dipole is not collinear with $\hat{\nu}$ [12], these are not relevant to the biological examples mentioned in the previous section.

We then expand the δ function in Eq. (5.1) ($\delta\left(\mathbf{r}-\mathbf{r}_i \pm \frac{l}{2}\hat{\nu}_i\right) = \delta\left(\mathbf{r}-\mathbf{r}_i\right) \pm \frac{l}{2}\hat{\nu}_i \nabla\delta\left(\mathbf{r}-\mathbf{r}_i\right) + \mathcal{O}\left(\nabla^2\right)$) and keep only linear terms in the gradient:

$$\boldsymbol{\tau}_i\left(\mathbf{r}\right) = \mp\, \tau\, l\, \hat{\nu}_i\hat{\nu}_i \cdot \nabla\delta\left(\mathbf{r}-\mathbf{r}_i\right)\ . \tag{5.2}$$

Summing over all N particles, and taking the ensemble average $\left\langle \sum_i^N \delta\left(\mathbf{r}-\mathbf{r}_i\right)\hat{\nu}_{i,\alpha}\hat{\nu}_{i,\beta} \right\rangle = \phi\left(\mathbf{r}\right)p_\alpha p_\beta$, the torque density becomes:

$$\tau_\alpha\left(\mathbf{r}\right) = \mp\, \tau\, l\, \partial_\beta\left(\phi\, p_\alpha p_\beta\right)\ . \tag{5.3}$$

Our goal is to find the active stress, whose divergence is the force density associated with the torque dipoles ($f^\tau_\alpha = \partial_\beta \sigma^\tau_{\alpha\beta}$). To that end, we recall the definition of torque $\tau_\alpha = \varepsilon_{\alpha\beta\gamma} r_\beta f_\gamma$ (and the property $\varepsilon_{ijk}\varepsilon_{imn} = \delta_{jm}\delta_{kn} - \delta_{jn}\delta_{km}$)

and recover the following equality:

$$f^{\tau}_{\beta} = -\partial_{\alpha}\left(\tau l\ \varepsilon_{\alpha\beta\mu}\partial_{\nu}\left(\phi p_{\mu}p_{\nu}\right)\right)\ . \tag{5.4}$$

Thus, we find the active stress due to an ensemble of torque dipoles to be:

$$\sigma^{\tau}_{\alpha\beta} = \zeta_{\tau}\varepsilon_{\alpha\beta\mu}\partial_{\nu}(\phi p_{\mu}p_{\nu})\ . \tag{5.5}$$

ζ_{τ} is the chiral activity parameter, with intensity proportional to both the torque strength τ and the length l of the particle, $|\zeta_{\tau}| = \tau l$. $\zeta_{\tau} > 0$ corresponds to right-handed particles, such as actomyosin, and $\zeta_{\tau} < 0$ to left-handed ones, like the case of *E. coli*. In this chapter, we will only focus on right-handed activity $\zeta_{\tau} > 0$ since the results for $\zeta_{\tau} < 0$ are related by a simple mirror image. Note that the stress (5.5) is chiral and contains an extra divergence when compared with the active stress for force dipoles. This will determine the scaling of the critical activity with system size, which is discussed in the following sections.

5.2 Linear stability analysis

To address the consequences of active chirality, we introduce the chiral stress of Eq. (5.5) in the hydrodynamic model presented in chapter 2. For simplicity, we also set the achiral active stress to zero, isolating the chiral effects. We highlight that the active stress is the only chiral contribution in the model as there is no cholesteric or chirality favouring term in the free energy. The fact that the chiral term is a nonequilibrium one distinguishes this system from active cholesteric liquid crystals [14].

The hydrodynamic model with chiral active stress is linearly unstable to perturbations of the uniformly aligned state when ζ_{τ} is larger than a given critical activity. This can be shown by linear stability analysis.

In order to facilitate our analysis, we look at a quasi-1D geometry with translational invariance in the $x \perp y$ plane, *i.e.* $\mathbf{p}$ and $\mathbf{u}$ depending only on z. We also consider the fluid confined between two plates at $z = 0$ and $z = L$. At these plates, the boundary conditions for the polarisation and velocity are

periodic, such that:

$$\mathbf{p}\left(z+L,t\right) = \mathbf{p}\left(z,t\right) \tag{5.6}$$
$$\mathbf{u}\left(z+L,t\right) = \mathbf{u}\left(z,t\right) \ . \tag{5.7}$$

The ground state solution for this system is homogeneously aligned, with null velocity field:

$$\mathbf{p}_0 = (0,0,1) \tag{5.8}$$
$$\mathbf{u}_0 = (0,0,0) \ . \tag{5.9}$$

We now introduce a small perturbation of $\mathbf{p}$ and $\mathbf{u}$, with the form:

$$\mathbf{p}\left(z,t\right) = \mathbf{p}_0 + \delta\mathbf{p}\left(z,t\right) = \begin{pmatrix} \delta p_x\left(z,t\right) \\ \delta p_y\left(z,t\right) \\ 1 \end{pmatrix} \tag{5.10}$$

$$\mathbf{u}\left(z,t\right) = \mathbf{u}_0 + \delta\mathbf{u}\left(z,t\right) = \begin{pmatrix} \delta u_x\left(z,t\right) \\ \delta u_y\left(z,t\right) \\ 0 \end{pmatrix} \ . \tag{5.11}$$

Note that the condition $|\mathbf{p}| = 1$ results in $\delta p_z = 0$ (up to first order in $\delta\mathbf{p}$). We also have $\delta u_z = 0$ due to incompressibility.

We use (5.10) and (5.11) to linearise the hydrodynamic equations and obtain the system:

$$\frac{\partial}{\partial t}\begin{pmatrix} \delta p_x \\ \delta p_y \end{pmatrix} = \begin{pmatrix} \frac{\xi+1}{2}\,\partial_z\,\delta u_x + \frac{K}{\Gamma}\,\partial_z^2\,\delta p_x \\ \frac{\xi+1}{2}\,\partial_z\,\delta u_y + \frac{K}{\Gamma}\,\partial_z^2\,\delta p_y \end{pmatrix} \tag{5.12}$$

$$\eta\,\partial_z^2\begin{pmatrix} \delta u_x \\ \delta u_y \end{pmatrix} = \begin{pmatrix} \frac{K(\xi+1)}{2}\,\partial_z^3 & \zeta_\tau\phi\,\partial_z^2 \\ -\zeta_\tau\phi\,\partial_z^2 & \frac{K(\xi+1)}{2}\,\partial_z^3 \end{pmatrix}\begin{pmatrix} \delta p_x \\ \delta p_y \end{pmatrix} \ . \tag{5.13}$$

In order to move forward, we re-write the perturbations as a Fourier expansion,

respecting the periodic boundary conditions:

$$\delta p_x(z,t) = \sum_{n=1}^{\infty} \tilde{p}_{xn}(t) \cos\left(\tfrac{2n\pi z}{L}\right) \tag{5.14}$$

$$\delta p_y(z,t) = \sum_{n=1}^{\infty} \tilde{p}_{yn}(t) \sin\left(\tfrac{2n\pi z}{L}\right) \tag{5.15}$$

$$\delta u_x(z,t) = \sum_{n=1}^{\infty} \tilde{u}_{xn}(t) \sin\left(\tfrac{2n\pi z}{L}\right) \tag{5.16}$$

$$\delta u_y(z,t) = \sum_{n=1}^{\infty} \tilde{u}_{yn}(t) \cos\left(\tfrac{2n\pi z}{L}\right) \ . \tag{5.17}$$

Note that the twist deformations of the polarisation **p** result in a velocity profile **u** that is perpendicular to **p**.

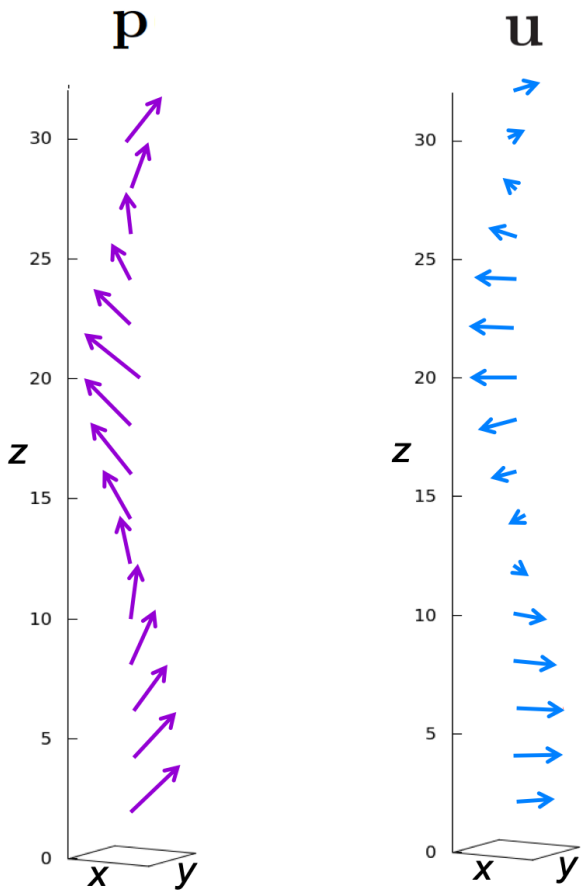

Figure 5.3 *Mode $n = 1$ of the steady state solution for $\zeta_\tau > \zeta_\tau^c$. **p** forms a helix along z. **u** is confined to the $x \perp y$ plane and rotates in a sinusoidal way around the z direction.*

Eqs. (5.14-5.17) resemble twisted configurations in helical nematics. For example, mode $n = 1$ is shown in Fig. 5.3. Substituting the Fourier expansion in Eqs. (5.12)

and (5.13), we obtain a linear differential equation for $\tilde{\mathbf{p}}(t)$:

$$\frac{\partial}{\partial t}\begin{pmatrix}\tilde{p}_{xn}(t)\\ \tilde{p}_{yn}(t)\end{pmatrix} = \begin{pmatrix} -\frac{4n^2\pi^2}{L^2}K\left(\frac{1}{\Gamma}+\frac{(\xi+1)^2}{4\eta}\right) & \frac{2n\pi}{L}\frac{\zeta_\tau\phi}{\eta}\frac{(\xi+1)}{2} \\ \frac{2n\pi}{L}\frac{\zeta_\tau\phi}{\eta}\frac{(\xi+1)}{2} & -\frac{4n^2\pi^2}{L^2}K\left(\frac{1}{\Gamma}+\frac{(\xi+1)^2}{4\eta}\right)\end{pmatrix}\begin{pmatrix}\tilde{p}_{xn}(t)\\ \tilde{p}_{yn}(t)\end{pmatrix}, \tag{5.18}$$

with solution:

$$\begin{pmatrix}\tilde{p}_{xn}(t)\\ \tilde{p}_{yn}(t)\end{pmatrix} = \mathbf{A}e^{\lambda_n^+ t} + \mathbf{B}e^{\lambda_n^- t} \tag{5.19}$$

for some given constants $\mathbf{A}$ and $\mathbf{B}$. The growth rates for this perturbation are:

$$\lambda_n^{\pm} = \frac{n\pi}{L}\frac{\xi+1}{\eta}\left\{\pm\zeta_\tau\phi - \frac{2n\pi}{L}\frac{2\eta K}{\xi+1}\left(\frac{1}{\Gamma}+\frac{(\xi+1)^2}{4\eta}\right)\right\} \tag{5.20}$$

The aligned state becomes unstable when $\lambda_n^+ > 0$ or $\lambda_n^- < 0$ which causes the linear perturbations to grow exponentially. This is equivalent to the condition that the activity magnitude is larger then some critical threshold $|\zeta_\tau| > \zeta_\tau^c$, which we calculate to be:

$$\zeta_\tau^c = \frac{1}{\phi}\frac{2n\pi}{L}\frac{2\eta K}{\xi+1}\left(\frac{1}{\Gamma}+\frac{(\xi+1)^2}{4\eta}\right) \tag{5.21}$$

The steady states for $|\zeta_\tau| > \zeta_\tau^c$ exhibit a helical pattern for the polarisation accompanied by a velocity profile in the plane perpendicular to the helical axis (see Fig. 5.3). In Eq. (5.21), n represents the mode of the sinusoidal twist. All the other constants are phenomenological parameters that define the system and were introduced in chapter 2. Note that the critical chiral activity scales as $1/L$, in contrast to the extensile or contractile instabilities whose critical activity scales as $1/L^2$. In our simulations, we shall only vary the size of the system L and the elasticity K, keeping the other physical quantities constant. Thus, and in analogy with the previous chapter, we choose the dimensionless chiral activity parameter to be:

$$\Theta_\tau = \frac{\zeta_\tau L}{K}\ . \tag{5.22}$$

5.3 Twist order parameter

We study the twist instability presented above through numerical simulations by using, as for the case of the rotating droplets, the hybrid lattice Boltzmann scheme detailed in chapter 3. We also use all the same physical constants as detailed in Table 4.1, for the case of flow aligning particles. The activity ζ_τ is taken to be in the range $0 - 0.05$.

To characterise the nonequilibrium transition into twisted states, we need to define an order parameter. We choose the twist parameter (5.23)

$$q_\tau = \varepsilon_{ijk} p_i \frac{\partial p_k}{\partial x_j} \tag{5.23}$$

that quantifies twist deformations in liquid crystal-like systems.

Let us take a simple helicoidal polarisation profile along the z direction to exemplify the meaning of q_τ:

$$\begin{aligned} p_x &= A_{tw}\ sin\left(\frac{2\pi}{P_{tw}} z\right) \\ p_y &= A_{tw}\ cos\left(\frac{2\pi}{P_{tw}} z\right) \\ p_z &= \mathrm{c}^{\mathrm{te}}\ . \end{aligned} \tag{5.24}$$

Here, $A_{tw} = \mathrm{c}^{\mathrm{te}}$ is the amplitude of the twist and P_{tw} is the pitch, *i.e.*the length necessary for a full 2π twist of the polarisation.

For the profile in (5.24), we obtain

$$q_\tau = A_{tw}^2 \frac{2\pi}{P_{tw}}. \tag{5.25}$$

We conclude from (5.25) that the amount of twist deformation in the system can increase either due to the sinusoidal amplitude A_{tw}, or to the pitch P_{tw}. Changes in the amplitude A_{tw} are continuous. However, the pitch depends on the number of full twists that "fit" in the length of the system and, consequently, on the type of boundary conditions imposed. For the case of periodic boundary conditions, the number of full turns must be an integer. Thus, variations in q_τ

due to changes in the pitch correspond to discontinuous jumps. We would like to note that the same discontinuity would be observed for any type of non-free boundary conditions. If $\mathbf{p}$ is anchored to have a particular value at the boundary, then the number of full twists must belong to a discrete set.

We can also write the amplitude A_{tw} in terms of p_z, the polarization component along the twist axis which is also a constant. This is a result from the constraint that the polarisation must be a unit vector $|\mathbf{p}| = 1$. The amplitude takes the form $A_{tw} = \sqrt{1 - p_z^2}$. Therefore, when the amplitude is maximum $A_{tw} = 1$, the polarisation profile is a pure helix with $p_z = 0$. When $A_{tw} < 1$, then $p_z \neq 0$, and the observed states are conical.

5.4 Spontaneous cholesteric twist in a quasi-1D system

We start by analysing the simulation results for the simplest configuration of torque dipoles. More specifically, we look at a one-dimensional string of torque dipoles located along the z direction. As required for the existence of twist deformations, we allow the polarisation field and the velocity of the underlying fluid to rotate in all 3 dimensions. Therefore, we refer to the system as "quasi-1D". We also impose periodic boundary conditions in x, y, and z. These ensure invariance along x and y, while forcing periodicity along z. The initial configuration is aligned, with $\mathbf{p}$ pointing perpendicularly to the z axis (either $p_x \simeq 1$ or $p_y \simeq 1$ since all directions on the plane $x \perp y$ are equivalent). We also include a 1% random variation of the polarisation components in the initial state. We then allow the system to reach steady state for different (and increasing) values of the chiral activity ζ_τ.

As predicted by linear stability analysis, when the activity reaches a critical threshold, we observe a non-equilibrium transition to a spontaneously twisted state. In order to plot the transition, we make use of dimensionless parameters. The onset of the transition is controlled by $\Theta_\tau = \zeta_\tau \frac{L}{K}$, as discussed in section 5.2. The twisted states are characterised by having $q_\tau \neq 0$. To better interpret the

twist in the system, we multiply the order parameter q_τ by $\frac{L}{2\pi}$ (see Eq. 5.23):

$$q_\tau \frac{L}{2\pi} = A_{tw}^2 \underbrace{\frac{L}{P_{tw}}}_{n_{tw}} \quad . \tag{5.26}$$

By using (5.26) to visualise the transition, we have a clear decomposition into the continuous and discontinuous contributions: the number of full twists n_{tw} must take integer values because of the periodic boundary conditions, while A_{tw} can vary continuously.

The transition is plotted in Fig. 5.4 for 9 systems with different lengths ($L = 90, 180, 360$) and elasticities ($K = 0.02, 0.04, 0.08$).

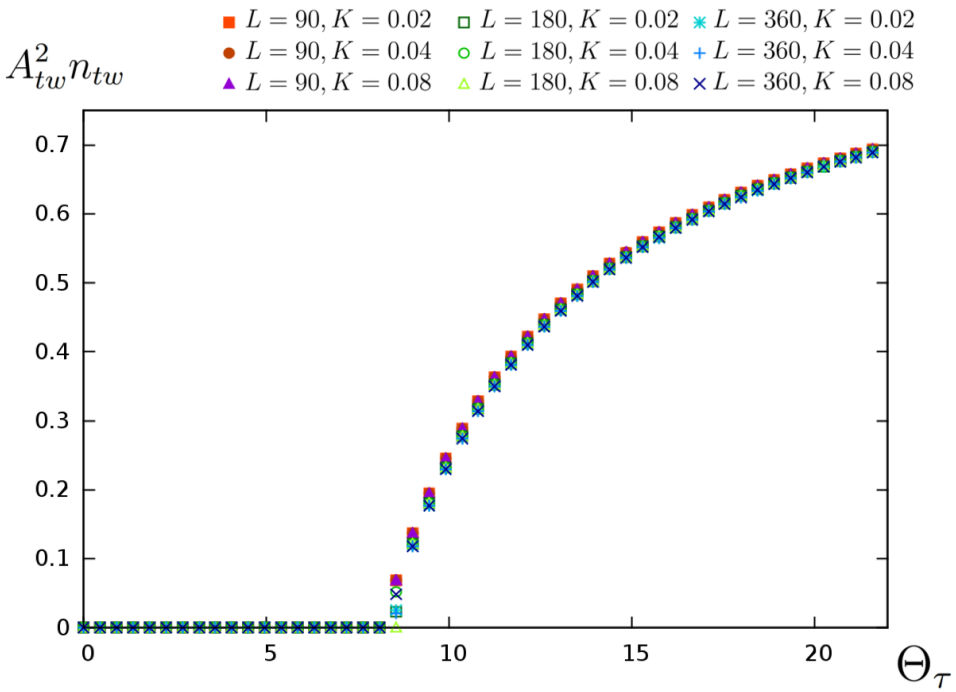

Figure 5.4 *Non-equilibrium transition to a spontaneously twisted state. Upon the increase of the chiral activity, the system undergoes a continuous transition from an aligned state ($A_{tw}^2 n_{tw} = 0$) to a spontaneously twisted state with finite pitch P_{tw} and amplitude A_{tw}. The scaling of the transition is controlled by the parameter Θ_τ so that the curves for different system dimensions L and elasticities K all collapse into one.*

With our choice of dimensionless parameters, we see the collapse of the curves for different systems. Therefore, we verify that the critical value of the chiral activity parameter scales linearly with K and inversely with L. This can be understood

since the active chiral stress injects a certain amount of chiral deformations in the system. These deformations are easier to accommodate for larger systems, and are hindered by the elasticity.

Our results also show that the nonequilibrium transition to spontaneously twisted states is continuous, as the order parameter $A_{tw}^2 n_{tw}$ increases smoothly from zero when the chiral activity threshold is reached. This is because, for the chiral activity range in Fig. 5.4, all the twisted configurations have $n_{tw} = 1$ and the transition is being driven by a continuous increase in A_{tw}.

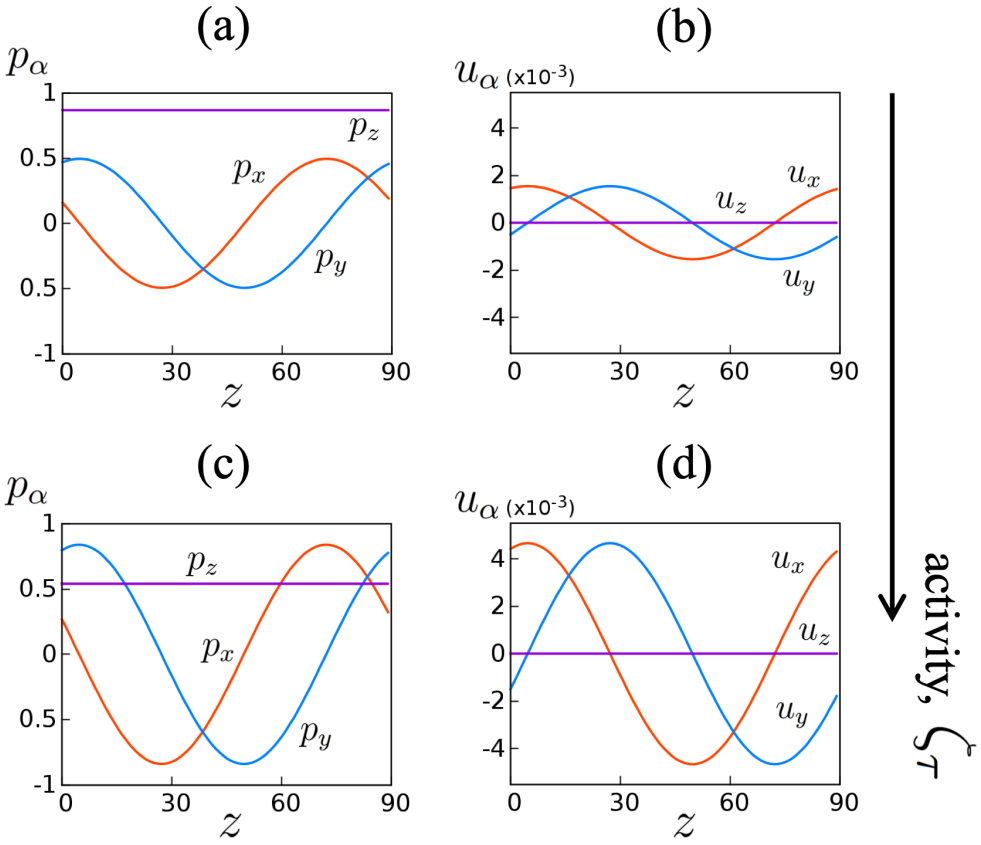

Figure 5.5 *Polarisation and velocity profiles for a quasi-1D system with* $L = 90$ *and* $K = 0.04$. *(a) and (b) correspond to* $\zeta_\tau = 4.4 \times 10^{-3}$, *while (c) and (d) correspond to* $\zeta_\tau = 10 \times 10^{-3}$, *both above the critical threshold of transition to twisted states. The two polarisation states are conical: while the* p_x *and* p_y *components vary sinusoidally, there is a constant non-zero* p_z *along the helical direction. The twist amplitude* A_{tw} *increases with the activity, almost doubling from (a) to (c). Higher twist amplitude corresponds to a higher magnitude of the fluid velocity: (b) and (d).*

In Fig. 5.5, we show two spontaneously twisted states. Figs. 5.5 (a) and (c) depict the polarisation $\mathbf{p}$ rotating sinusoidally on the plane $x \perp y$, in a helix-like pattern. However, there is also a non-zero component of the polarisation

along the helical axis, $p_z \neq 0$. This means that the resultant twisted states are conical instead of purely helical. We also observe that the twist in the polarisation induces a non-zero velocity field. Due to the sinusoidal variation of p_x and p_y, the corresponding components of the velocity $\mathbf{u}$ also vary sinusoidally (see Fig. 5.5 (b) and (d)). Unlike the polarisation, the velocity $\mathbf{u}$ is contained in the plane perpendicular to the helical axis, with $u_z = 0$ as a result of p_z being constant.

By comparing Figs. 5.5(a) and (c), we also note that the amplitude of the twist increases with the chiral activity. As a result, p_z must decrease (see Fig. 5.5(d)). This means that, as the chiral activity goes up, the resultant twisted states go from being more conical (low activity) to more helical (high activity).

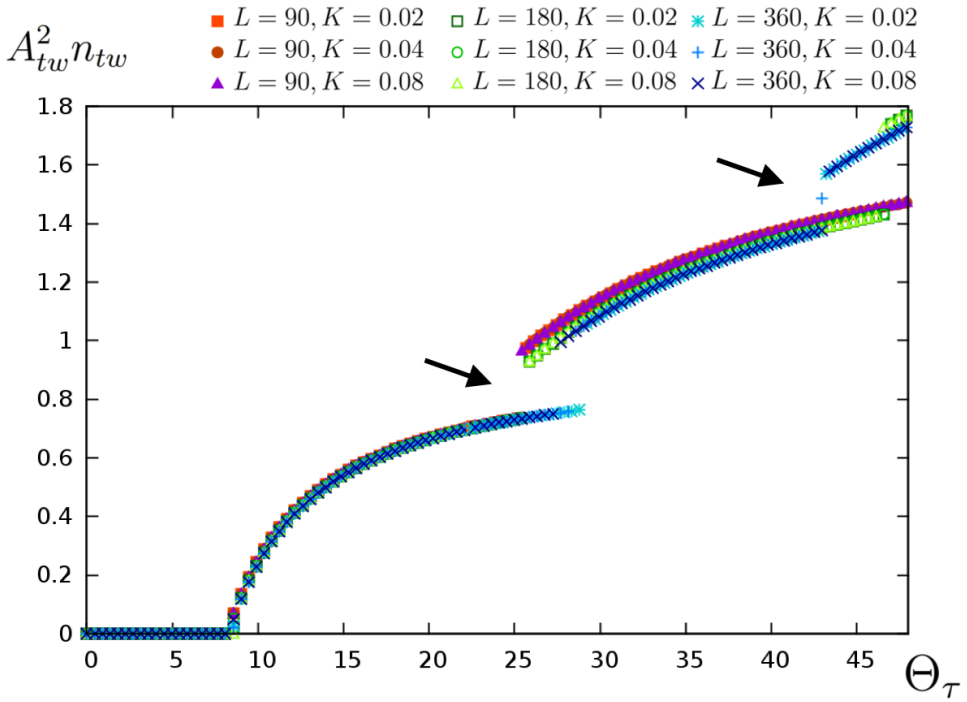

Figure 5.6 *Non-equilibrium transition to spontaneously twisted states with* $n_{tw} = 1, 2, 3$. *(Note that this figure is an extension of Fig. 5.4 into a range of larger* Θ_τ*.) As the chiral activity increases, we first encounter a state with* $P_{tw} = L$*, then states with* $P_{tw} = \frac{L}{2}$ *and* $P_{tw} = \frac{L}{3}$*. The points at which the number of turns changes from 1 to 2 and 2 to 3 correspond to discontinuous jumps in the order parameter and are signalled by black arrows. Within the domains of* $n_{tw} = const$*, the order parameter increases continuously with* Θ_τ*, indicating an increasing twist amplitude.*

Visualising the twisted states with $n_{tw} = 1$ helps describe the transition depicted in Fig. 5.4. Above the critical threshold of the chiral activity, the aligned state becomes unstable and is replaced by a twisted state with $P_{tw} = L$. The transition

is continuous because it is equivalent to going from a state with $A_{tw} = 0$ and $P_{tw} = \infty$ to a state with finite A_{tw} and P_{tw}. This is possible through the smooth increase of A_{tw}. As the activity is increased, the twist goes up until it saturates at $A_{tw} < 1$. The fact that the twist amplitude never reaches its maximum value $A_{tw} = 1$ means that all observed states are conical. If the chiral activity continues to increase past this point, the only way to introduce further twist into the system is to increase the number of twists. This implies discontinuous jumps in the order parameter, as we can see in Fig. 5.6 (marked by the black arrows).

Figure 5.7 contains the polarisation and velocity configurations for states with $n_{tw} = 2, 3$. Just like before, we observe that the polarisation describes a conical helix with $p_z \neq 0$ and $A_{tw} < 1$.

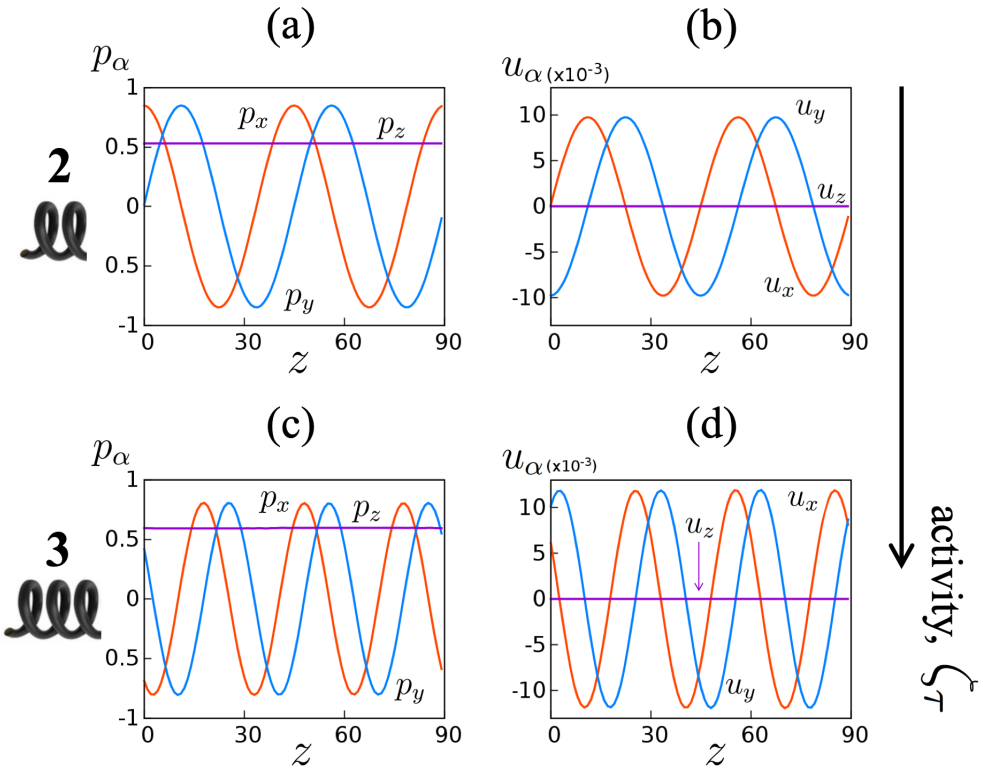

Figure 5.7 *Polarisation* $\boldsymbol{p}$ *and fluid velocity* $\boldsymbol{u}$ *for spontaneously twisted states with* $n_{tw} = 2$*: (a) and (b), and* $n_{tw} = 3$*: (c) and (d). The respective chiral activity values are* $\zeta_\tau = 2.0 \times 10^{-2}$ *and* $\zeta_\tau = 2.2 \times 10^{-2}$.

Our simulation results for a quasi-1D system reveal that the chiral active stress leads to spontaneously twisted states, which are similar to equilibrium cholesterics. However, we note that there is no thermodynamic chirality in the free energy and that the system's twist is purely a nonequilibrium phenomena.

5.5 Self-assembled cholesteric patterns in a quasi-2D system

We now look at the correspondent "quasi-2D system" which consists of a $L \times L$ layer of torque dipoles. We choose to work in the $y \perp z$ plane. Just as in the quasi-1D case, the polarisation and velocity are allowed to escape into the third dimension (x in this case) so that we can observe twisting. We proceed in the same way as before: initialise the system with an aligned configuration and let it reach steady state for increasing values of the chiral activity ζ_τ.

Once again, we find nonequilibrium transitions into spontaneously twisted states. In the quasi-2D geometry we can also observe a greater variety of dynamical steady states, which are akin to layer formation and fingering patterns in cholesteric liquid crystals.

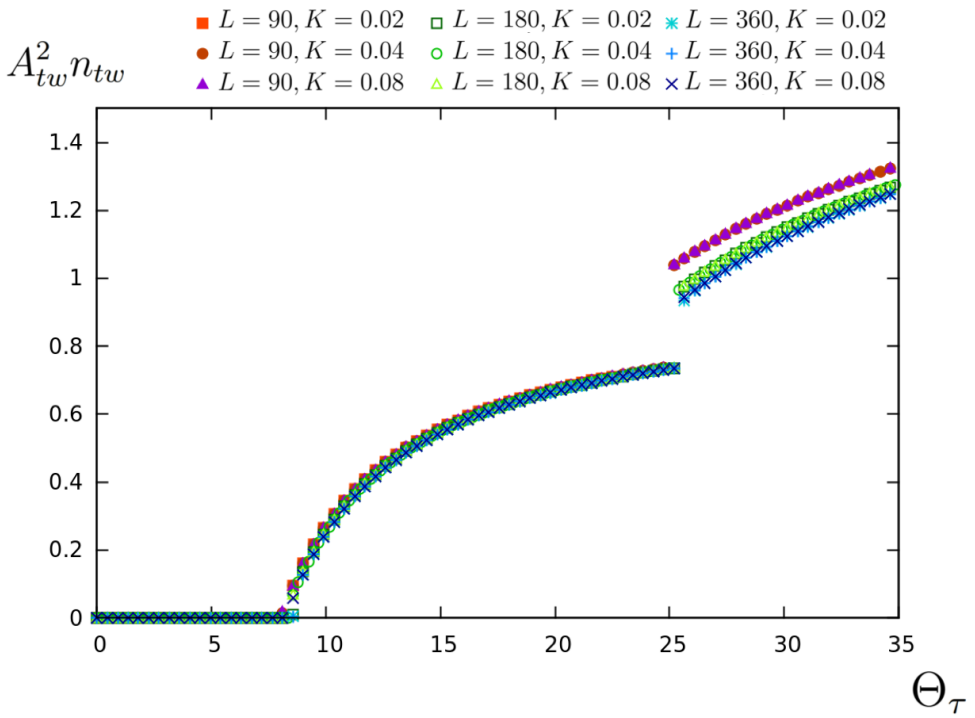

Figure 5.8 *Nonequilibrium transition into spontaneously twisted states in a quasi-2D system of torque dipoles. Upon the increase of the chiral activity, we observe a continuous transition into states where the polarisation performs one full twist (with increasing amplitude) followed by a discontinuous jump into states where the polarisation twists twice in the length of the system.*

Figure 5.8 depicts the nonequilibrium transition for the quasi-2D geometry. We

calculated the transition for the system sizes $L = 90, 180, 360$ and elasticity values $K = 0.02, 0.04, 0.08$. The transition and its scaling are identical to the quasi-1D case. First, a continuous increase in the twist parameter leading to states with $P_{tw} = L$. In these configurations, the twist amplitude increases continuously with Θ_τ. This is followed by a discontinuous jump into states with $P_{tw} = \frac{L}{2}$. Note that the transition was calculated by choosing the initial conditions so that the direction of twist is either y or z. As in the quasi-1D case, the amplitude is always < 1 and the orientation describes a conical, rather than a cylindrical, helical shape.

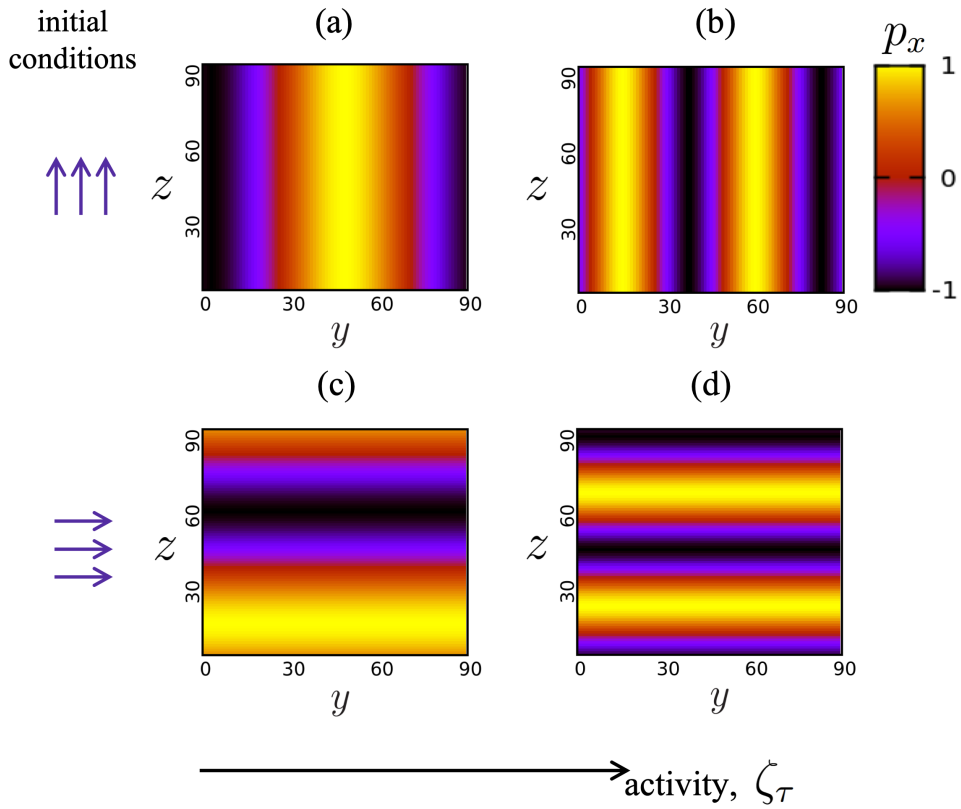

Figure 5.9 *Cholesteric-like layers for a quasi-2D system of torque dipoles. Different patterns can be obtained depending on the initial conditions and chiral activity. For aligned initial conditions with $p_z = 1$, the twist axis is y and the layers form "vertically": (a) and (b). For initial conditions with $p_y = 1$ the helical axis is now z and the layers form "horizontally" instead: (c) and (d). In both cases, when the chiral activity ζ_τ increases, we can see the number of layers go from one: (a), (c); to two:(b), (d).*

The twisted phase in quasi-2D corresponds to the formation of "layers", as in equilibrium cholesteric liquid crystals. These layered configurations are shown in Fig.5.9.

The direction of the layers formed is influenced by the choice of initial conditions. If we initialise the system with $p_z = 1$, the polarisation starts to describe a helical pattern along y, and we observe "vertical" layers (Fig. 5.9(a) and (b)). In turn, if we initialise the system with $p_y = 1$, the helical axis is now along z and we observe "horizontal" layers (Fig. 5.9(c) and (d)). In both cases, we can see an increasing number of layers with activity. In Fig. 5.9 we show configurations with one ((a), (c)) and two layers ((b), (d)), which correspond to the activity regimes of Fig. 5.8.

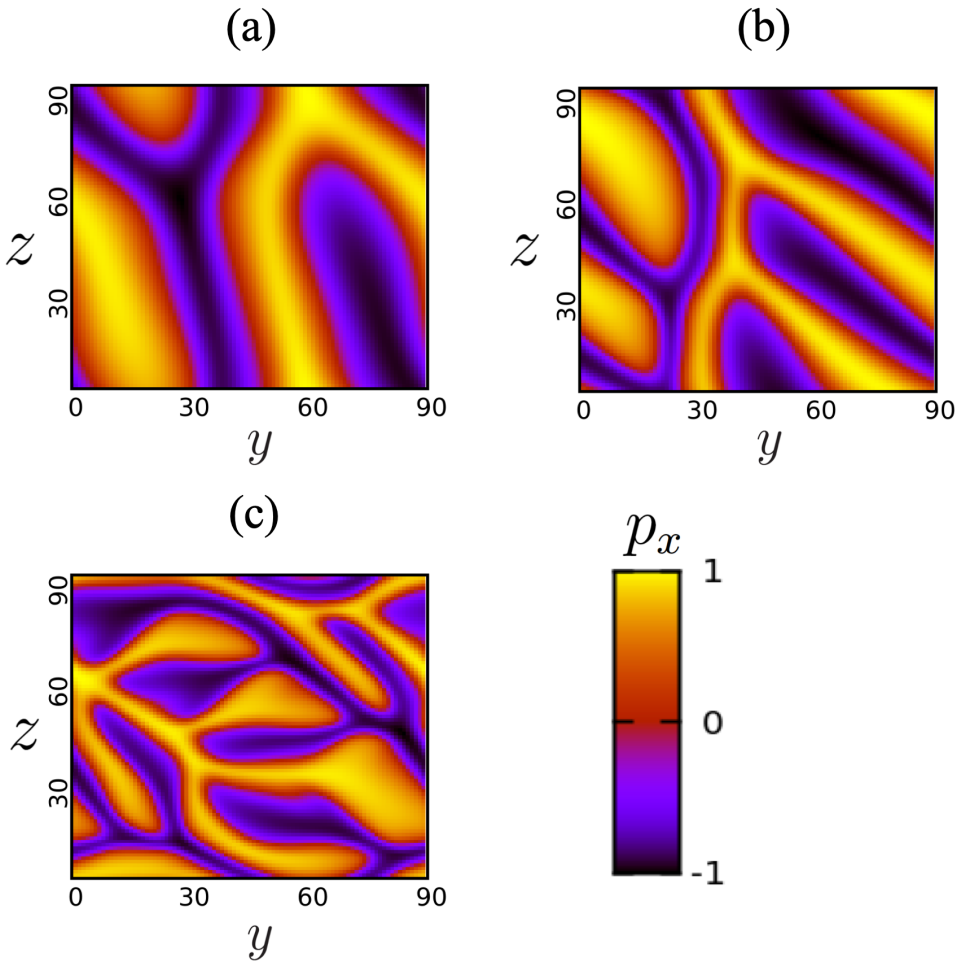

Figure 5.10 *Formation of cholesteric-like patterns for a system of active torque dipoles. For high values of the chiral activity, the system starts to rotate locally in different directions, giving rise to "fingering" patterns of incomplete layers. These patterns are static in steady state. (a): $\zeta_\tau = 1.5 \times 10^{-2}$. (b): $\zeta_\tau = 2.0 \times 10^{-2}$. (c): $\zeta_\tau = 2.5 \times 10^{-2}$.*

Figures 5.8 and 5.9 show a straightforward generalisation from the quasi-1D geometry, without any significant changes in the transition or observed steady states. However, in a quasi-2D geometry, we expect the system to be free to twist

along any direction on the plane. The layered configurations of Fig. 5.9 were, in fact, procured with a careful choice of initial conditions in a regime of moderate chiral activity. The choice of the twist axis in the system is actually a result of spontaneous symmetry breaking and we do observe layered patterns forming with other planar orientations. Moreover, upon the increase of the chiral activity, the system can develop domains that twist locally around different directions, resulting in different "fingering" patterns as seen in Fig. 5.10. These irregular patterns are static in steady state. The formation of such structures is also a common phenomenon in equilibrium cholesterics.

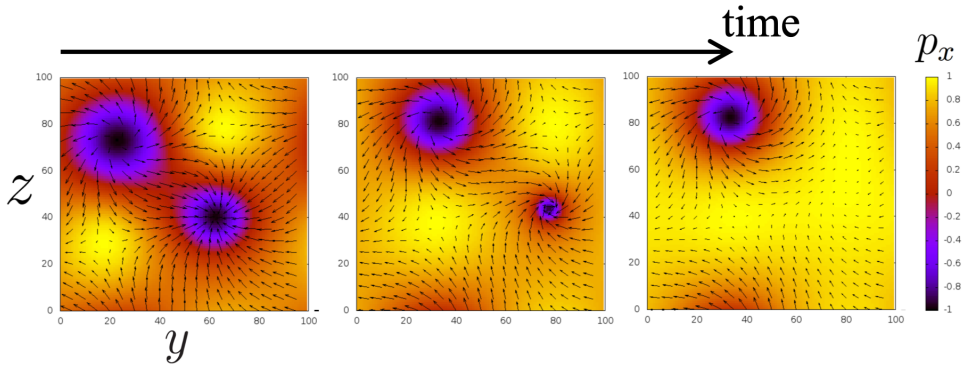

Figure 5.11 *Formation of non-singular topological defects. For values of the chiral activity below the transition threshold we observe a transient state where a pairs of defects (+1 and −1) are formed. The defects are non-singular, as is characteristic of cholesteric phases. After being created, the defects drift along the system and then annihilate with each other. The arrows represent the polarisation in-plane, and the colour scale refers to the polarisation component perpendicular to the plane (p_x).*

Extreme values of the chiral activity harbour interesting active behaviour, too. For low activities (below the transition threshold) we find a transient state in which +1 and −1 topological defects are formed (see Fig. 5.11). As is typical in cholesteric liquid crystals, the order does not fall to zero at the defect core. This is because the polarisation $\mathbf{p}$ can escape into the x direction (perpendicular to the plane). The defects are created, drift for some time in the system, and are then annihilated (See Suppl. Movie 5.1[1]).

On the other end of the spectrum, for high values of ζ_τ, we observe a seemingly chaotic dynamics where the cholesteric layers are formed, destroyed, and rearranged continuously over time. Figure 5.12 shows two stills of the same

[1] All the movies referred to in this Chapter can be found in the Supplementary Materials on DataSync (https://datasync.ed.ac.uk/index.php/s/AjP4ZfSEl07uHiV?path=%2F). Appendix C contains a short description of all the Chapter 5 Suppl. Movies.

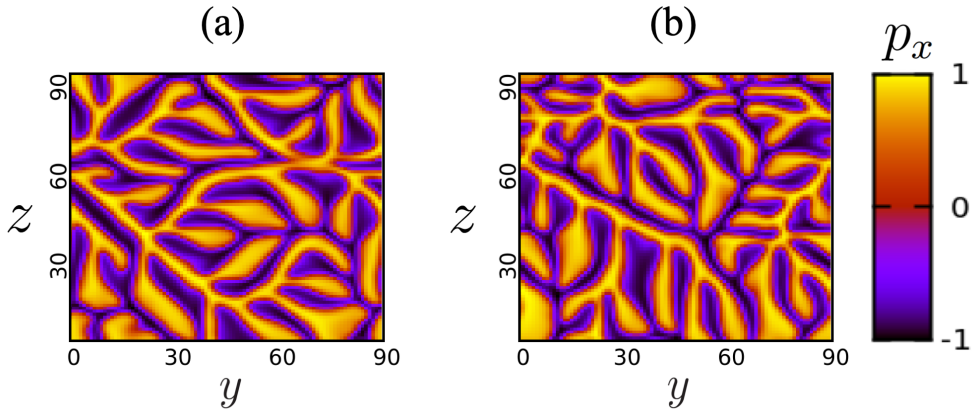

Figure 5.12 *Turbulent regime in quasi-2D chiral active fluids.* $\zeta_\tau = 4 \times 10^{-2}$. *When the chiral active stresses are strong enough, the twisted layers change dynamically in a turbulent-like flow. (a) and (b) correspond to two snapshots of the same system at different timesteps.*

turbulent system at two different time-steps (See Suppl. Movie 5.2). In active nematics, it is known that the increase of activity generically leads to "active turbulence", with the formation of vortices and of liquid crystal domains with a characteristic lengthscale [22]. We interpret the patterns in Figure 5.12 as the analogue of these turbulent states in our nonequilibrium chiral system.

5.6 Dry active chiral system

In this final section of chapter 5 we focus on a different type of system: a "dry" active system – modelling, for instance, a collection of active torque dipoles close to a substrate, which works as a momentum sink. While here we are not aiming at a profound study of chirality in dry active systems, we want to understand if the mechanism leading to the emergence of macroscopic twist is also present outside of the active fluid (wet) class. Note that while active dry and wet systems may be similar in many aspects, including orientational order and local energy transduction, there is one main distinction: momentum is not conserved in dry systems.

With this in mind, we choose to model a simple dry active system through a continuous formulation. We consider a system of N active particles with local

orientation $\mathbf{p}$, which evolves according to the following dynamical equation:

$$\frac{\partial \mathbf{p}}{\partial t} = \frac{\mathbf{h}}{\Gamma'} + N\tau \times \mathbf{p} \ . \tag{5.27}$$

In Eq. (5.27), $\mathbf{h} = \frac{\delta \mathcal{F}}{\delta \mathbf{p}}$ is the molecular field calculated as the derivative of the free energy. We draw from our model in chapter 2 and use the Landau free energy density (2.4) to describe the particles' tendency to align, and assume $\mathcal{F} = \int d\mathbf{r} \left\{ \frac{A}{4}|\mathbf{p}|^4 - \frac{A}{2}|\mathbf{p}|^2 + \frac{K}{2}|\nabla \mathbf{p}|^2 \right\}$. $\Gamma' > 0$ is the rotational relaxation constant, and τ is the torque density, which for active torque dipoles is equal to:

$$\tau_\alpha = \zeta_\tau \partial_\beta (p_\alpha p_\beta) \ . \tag{5.28}$$

ζ_τ is the already defined the activity parameter. We have once more introduced chirality through the torque dipole approximation to facilitate the comparison with the results for active fluids.

Since there is no solvent, we only need to follow the evolution of $\mathbf{p}(\mathbf{r}, t)$.

In analogy with the "wet" active fluid case, the model above exhibits a twist instability when ζ_τ is larger than a critical value ζ_τ^c:

$$\zeta_\tau^c = \frac{2n\pi}{L} \frac{K}{N\Gamma'}. \tag{5.29}$$

We note that the scaling of the critical activity is the same as for active fluids, $\zeta_\tau^c \sim \frac{K}{L}$, so that we can continue to use the dimensionless activity parameter Θ_τ.

Figure 5.13 depicts this nonequilibrium transition for a quasi-1D geometry with periodic boundary conditions. This is the same system set up that we used in section 5.4. We have also performed simulations in quasi-2D but the results in this case are a trivial generalisation of the quasi-1D ones.

Although the critical activity scales in the same way as in the wet system with respect to system size and elasticity, the nature of the transition is radically different. In the dry case, the transition is discontinuous. For the range of activities depicted in Fig. 5.13, we observe four discontinuous jumps of the order parameter $A_{tw} n_{tw}$, corresponding to systems with up to 4 full twists. Moreover, for each group of states with fixed n_{tw}, the order parameter is constant so that

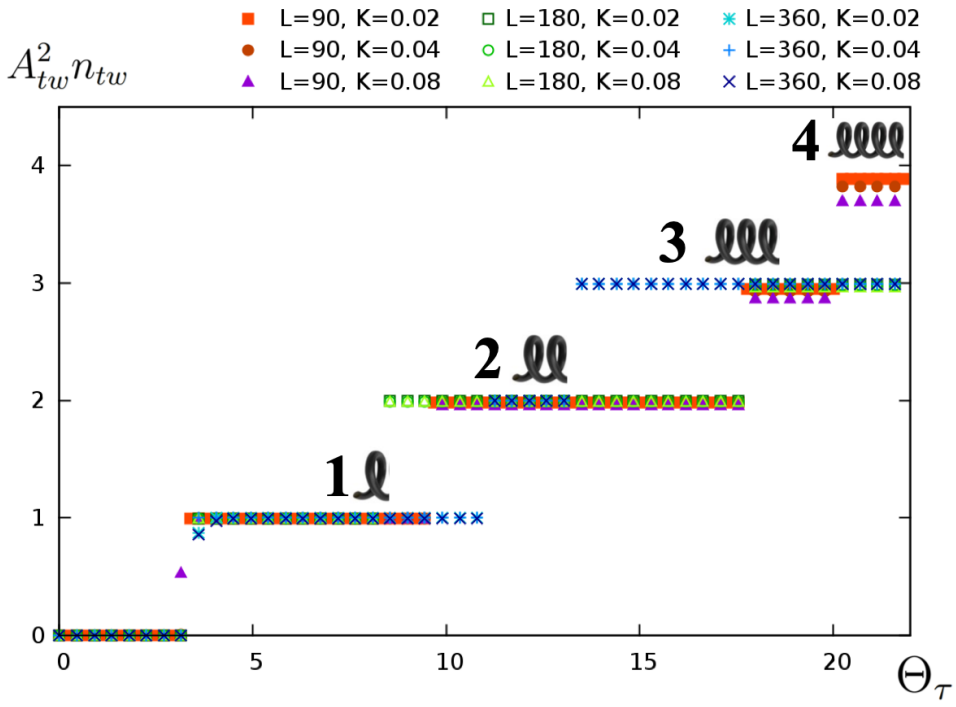

Figure 5.13 *Nonequilibrium transition into spontaneously twisted states for a quasi-1D dry system of torque dipoles. Above a certain threshold value of the activity parameter, the system twists spontaneously into a helical pattern with* $n_{tw} = 1, 2, 3, 4$. *The transition is discontinuous and the states for a given number of twists correspond to a flat plateau.*

we see four flat plateaus ($A_{tw} n_{tw} = 1, 2, 3, 4$) in the graph. Therefore we can conclude that the amplitude of the twist deformations is always maximum $A_{tw} = 1$ and all the states are cylindrical helices with $p_z = 0$. Figure 5.14 shows the polarisation for these spontaneously twisted states, confirming that for all of them the amplitude is maximum and there is no component of the polarisation along the twist axis.

We would also like to note that the different twisted states seem to be metastable for intermediate ranges of the activity. Without the presence of the underlying fluid and chiral flows, the active chirality injected in the system by the torque dipoles is all transmitted to the polarisation's twist. Therefore, $\mathbf{p}$ twists always with maximum amplitude and adjusts the deformation by changing the pitch (or twist number) when activity increases. However, the system is constrained by the periodic boundary conditions and can only twist with a discrete set of values of the pitch (which are sub-multiples of the system's length). The metastability arises from this constraint for activity values near the transition between two

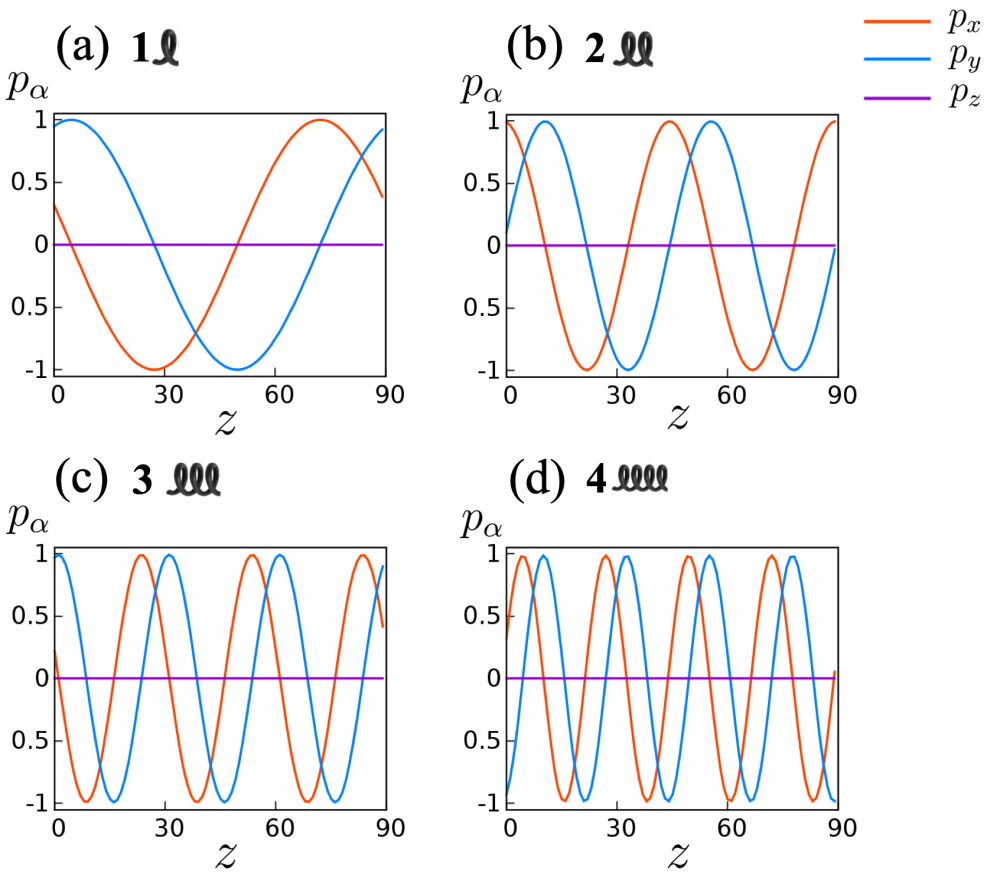

Figure 5.14 *Spontaneously twisted configurations in a quasi-1D dry active system with $L = 90$ and $K = 0.04$. The four configurations correspond to different number of twists (or, equivalently, different pitch) for increasing chiral activity parameter: (a) $n_{tw} = 1, P_{tw} = L$; (b) $n_{tw} = 2, P_{tw} = \frac{L}{2}$; (c) $n_{tw} = 3, P_{tw} = \frac{L}{3}$; (d) $n_{tw} = 4, P_{tw} = \frac{L}{4}$. In all the configurations, the polarisation describes a cylindrical helix along the z direction.*

different twisted states.

5.7 Concluding remarks

Chirality is ubiquitous in microscopic biological structures. It arises both from the shape of the constituents (cytoskeletal filaments, bacterial flagella) and from the mechanisms used for motility (helical flagellar motion). Thus, chiral stresses and torques must be included in a full description of biological activity. This is a relatively unexplored area of the study of active fluids.

In this chapter, we introduced the torque dipole approximation for active

particles. This is the lowest order chiral contribution for a neutrally buoyant particle. With this formulation, we have found that the active stress results in a chiral term in the Navier-Stokes equation.

We show, by linear stability analysis and numerical simulations, that the chiral active stress gives rise to spontaneously twisted configurations in the absence of any thermodynamic favouring. These twisted states, that resemble equilibrium cholesterics, are self assembled and appear due to purely nonequilibrium effects. We have dubbed this phase "active self-assembled cholesteric".

We find, in quasi-1D and quasi-2D active fluids, that the transition from an aligned state to an active self-assembled cholesteric is continuous. The spontaneously twisted steady states found have an amplitude that increases smoothly with the chiral activity. After the first continuous transition, the system can discontinuously jump to states with several twists. This discontinuity is due to the imposition of boundary conditions along the helical axis direction (periodic in our case). The twisted steady state configurations are conical as there is always a constant non-zero component of the polarisation along the helical axis. The associated flow fields are also chiral and contained in the plane perpendicular to the axis of twist. In quasi-2D we find many of the structures that usually arise in cholesterics: layered and fingering patterns and even non-singular moving defects. We also find an exemple of active turbulence, similar to those described by Thampi *et al.* in [22]. In this case, the permanent flows are sustained by the arranging and rearranging of local twist. The dynamics is driven by the resultant areas of deformation and moving non-singular defects.

We have also found nonequilibrium helical states in simulations of dry active systems. This case models a thought experiment where the active torque dipoles are in contact with a substrate which works as a momentum sink so that momentum is not conserved. We found that the dry and wet model are qualitatively different, as in the active phase of the former the polarisation twists into a cylindrical helix with maximum twist amplitude and the transition exhibits a series of plateaus corresponding to the number of full twists.

Nonequilibrium self-assembled cholesterics differ from both equilibrium and active cholesterics [14]. In those cases, chiral asymmetry arises solely from the molecular structure and can be included in an equilibrium free energy formulation. On the other hand, chiral active stresses depend on nonequilibrium motor processes and are linked to the active influx of energy in the system. Thus, there are still

open questions about the behaviour and rheology of such phases; for instance, equilibrium cholesterics are known to possess a permeative flow regime with significant viscosity increase [84], and it would be of interest to see whether this is the same for the nonequilibrium chiral phases which we have discussed in this chapter.

In general, active chirality is expected to affect biological motility patterns [85] and flows in such a way that can be measured experimentally [12] and we encourage further studies to attempt detection chiral and twisted macroscopic patterns. In particular, chiral effects become more prominent near walls or surfaces [86, 87], where our dry active model might be more appropriate.

Chapter 6

Chiral and achiral stresses in active fluids

In chapters 4 and 5 we have studied achiral and chiral active stresses independently. The two types of stress can be found in biological active systems since the microscopic active particles (*e.g.* actomyosin and bacteria) stir and rotate the fluid while moving. Both achiral and chiral active fluids exhibit hydrodynamic instabilities characterised by spontaneous fluid flow, which is linked to macroscopic deformations of the orientational order. Achiral extensile and contractile stresses are unstable to bend and splay deformations (respectively), while chiral stresses result in spontaneous twist deformations. The three hydrodynamic instabilities can be used to describe a wide range of motility patterns in active gels, from translating and rotating droplets [4, 88, 89] to nonequilibrium cholesteric layering, and turbulent defect dynamics [22].

However, we have not yet considered the fully generalised description of biological active fluids, where the active stress contains both chiral and achiral contributions. That is what we shall do in the final chapter of this thesis. In this situation, we expect that there will be a coupling between both types of active stress. Recall that, even when the active stresses are achiral, we can observe chiral or rotating states, with spontaneous symmetry breaking being responsible for the left-right asymmetry at the macroscopic level [89].

Indeed, recent simulations by Tjhung *et al.* [85] have shown that the macroscopic chirality of an active droplet motion is not necessarily determined by its microscopic chirality, and it depends on the overall orientation pattern when

dipolar forces are present.

On the other hand, since our results in chapter 5 show that chiral stresses give rise to nonequilibrium self-assembled cholesteric phases, this investigation will also allow a comparison with active cholesteric liquid crystals, as described by Whitfield *et al.* in [14]. Note that in the latter system, cholesteric order results from an equilibrium term in the free energy. Notwithstanding, the authors describe a variety of interesting phenomena, including a mixed pitch-splay instability involving undulation of the cholesteric layers.

Thus we divide the chapter in two parts as follows. First, we investigate the effect of chiral active stresses on a system with an equilibrium cholesteric phase. Interestingly, we find that the chiral activity is able to "untwist" the equilibrium cholesteric when there is a chirality mismatch. Secondly, we look at the competition between chiral and achiral stresses. Our results show that extensile activity enhances the spontaneous twist transition of chapter 5, while contractile stresses hinder it. We also find steady state configurations with undulated and motile cholesteric layers in the extensile case.

6.1 Untwisting cholesterics through activity

For this section, we model a chiral active fluid using the hydrodynamic description of torque dipoles presented in chapter 5. However, we also include a cholesteric term in the Landau free energy (2.4), favouring a twisted equilibrium state. The cholesteric free energy density is:

$$f_{chol} = -K\ q_0\ \mathbf{p} \cdot \nabla \times \mathbf{p}, \tag{6.1}$$

with $q_0 = \frac{2\pi}{P_0}$ being the equilibrium twist number corresponding to the equilibrium pitch P_0, and K the elastic parameter in the 1 elastic constant approximation. The resulting system is, thus, composed of active particles which are structurally chiral, and also exert chiral stresses on the surrounding fluid, *via* an active torque dipole (as in chapter 5).

We simulate the system in a quasi-1D periodic geometry, using the hybrid lattice Boltzmann scheme. For this analysis, we choose a fixed value of P_0, equal to a sub-multiple of the system size L, so as to respect the periodic boundaries. We

then introduce an increasing amount of the chiral activity ζ_τ. As in chapter 5, we use the dimensionless chiral activity parameter $\Theta_\tau = \frac{\zeta_\tau L}{K}$ (see Eq. 5.22) to plot the observed transitions.

Let us start by discussing the situation where both the equilibrium free energy and the chiral activity favour right-handed states, *i.e.* $q_0 > 0$ and $\zeta_\tau > 0$. The results are shown in Fig. 6.1 for $P_0 = L = 90$ lattice units.

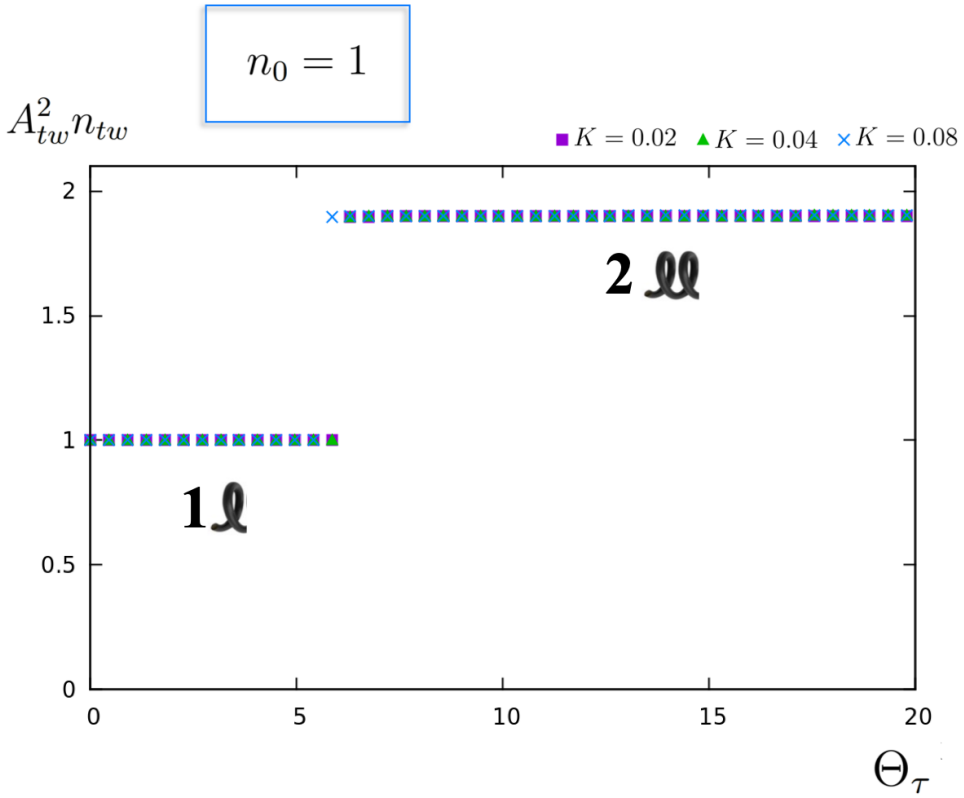

Figure 6.1 *Above a certain threshold, chiral activity doubles the twist number in a right-handed equilibrium cholesteric. For activity above the critical value, the system jumps discontinuously from the equilibrium state with $P_0 = L$, $n_0 = 1$ to a state with twice as much twist deformation $n_0 = 2$ and halved pitch $P_{tw} = \frac{L}{2}$. For this simulation, $L = 90$ and $K = 0.02, 0.04, 0.08$.*

Figure 6.1 shows that, upon the increase of the dimensionless chiral activity Θ_τ, the system transitions from the equilibrium configuration with 1 twist to a state with 2 twists, so that cholesteric pitch changes from $P_0 = L$ to $P_{tw} = \frac{L}{2}$. The dimensionless parameters that we use to describe the transition have been introduced in chapter 5 Eqs. (5.22) and (5.26) and will also be used throughout this chapter. Interestingly, the switch between twisted configurations in Fig. 6.1 is a discontinuous jump between two flat plateaus. This means that there is no continuous variation of the twist amplitude A_{tw} when the activity increases,

but rather an abrupt change in the number of turns $n_0 = 1 \to n_{tw} = 2$. The situation resembles the spontaneous twist transitions of dry active torque systems in section 5.6.

Perhaps a more curious situation arises when the equilibrium and active chiralities are opposite to each other. To investigate what happens in this case, we keep the right-handed chiral activity, but choose $P_0 = -L$ so that the equilibrium state is left-handed with one full twist $n_0 = -1$.

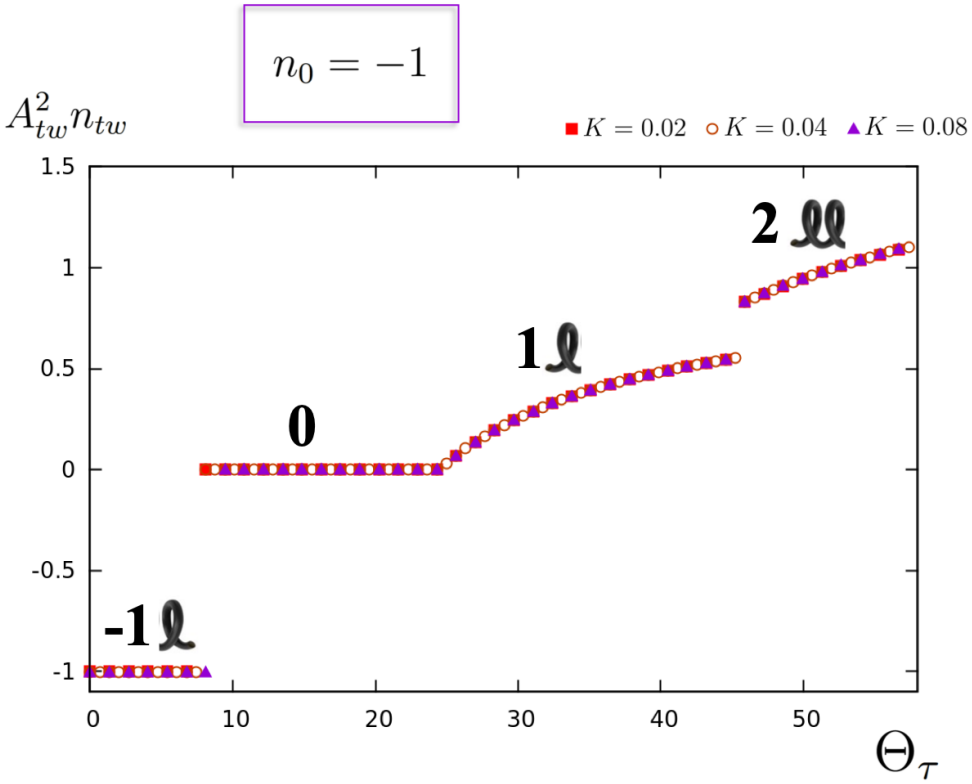

Figure 6.2 *Untwisting an equilibrium cholesteric. Simulation for an active chiral fluid with a left-handed cholesteric equilibrium state and pitch $P_0 = -L$. When the right-handed chiral activity increases, the equilibrium cholesteric state is discontinuously untwisted into an aligned configuration. As the chiral activity continues to increase, we observe the continuous twist transition into conical right-handed states of increasing twist amplitude A_{tw} and $n_{tw} = 1$, followed by a discontinuous jump to conical states with $n_{tw} = 2$*

The result in Fig. 6.2 reveals the existence of four different regimes for increasing activity in the range explored. First, we observe a left-handed twisted phase which corresponds to the equilibrium configuration, followed by an aligned phase with no twist. Effectively, this means that the opposing right-handed activity was able to "untwist" the cholesteric phase. The transition between these two

states is discontinuous. From the aligned phase, the twist amplitude increases continuously into right-handed twisted states that are conical ($A_{tw} < 1$, $n_{tw} = 1$). The graph then jumps again, signalling the transition to conical states with $n_{tw} = 2$. The second part of the transition is the same observed in Fig. 5.6. Thus, the chiral activity first overcomes the opposing equilibrium chiral term, untwisting the cholesteric, and then proceeds to spontaneously twist the polarisation as if the equilibrium term was absent. The only difference in this case is that the critical activity necessary for the onset of the spontaneous twist transition is now higher, and proportional to q_0.

Figure 6.3 (a) and (b) show the same results for systems with equilibrium number of twists $n_0 = -2$ and $n_0 = -3$, respectively (the minus sign indicates that the equilibrium configuration is left-handed).

We observe the chiral activity untwist the turns of the equilibrium configuration discontinuously one by one, and then cause the orientation to rotate in the right-handed sense. The right-handed twisted states are no longer cylindrical helices, but conical ones, where the twist amplitude can increase continuously with activity.

6.2 Active chirality coupled to contractile and extensile stresses

We now wish to investigate the competition between chiral and achiral stresses. To do so, we return to the model of active systems with a polar nematic equilibrium phase ($q_0 = 0$). Thus, we can consider only nonequilibrium chiral effects originating from the active stress.

We simulate an active gel with active stress given by two contributions:

$$\sigma_{\alpha\beta}^{active} = -\zeta_f \ \phi \ p_\alpha p_\beta + \zeta_\tau \ \varepsilon_{\alpha\beta\mu} \ \partial_\nu(\phi \ p_\mu p_\nu) \ . \tag{6.2}$$

The first term is achiral and it is the result of the force dipole approximation. ζ_f is the achiral activity parameter. $\zeta_f > 0$ corresponds to extensile forces and $\zeta_f < 0$ to contractile ones. The chiral term derives from the torque dipole approximation. The chiral activity parameter ζ_τ is positive $\zeta_\tau > 0$ for right-handed torque dipoles,

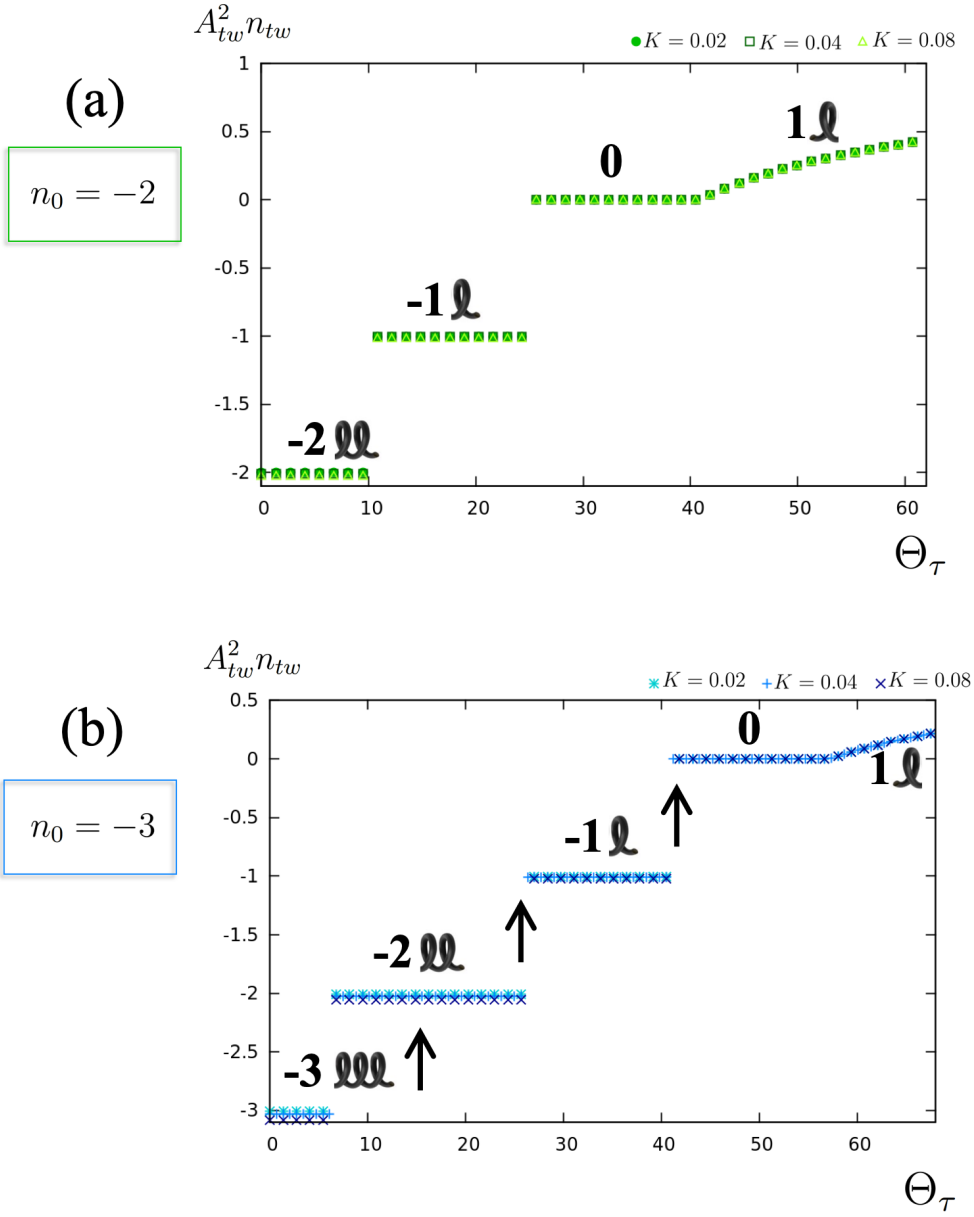

Figure 6.3 *Untwist of a left-handed equilibrium cholesteric with $P_0 = -\frac{L}{2}$ (a) and $P_0 = -\frac{L}{3}$ (b). The left-handed twists are undone discontinuously one by one until an aligned state with zero twist deformations is found. Above a certain activity threshold from the aligned state, we observe the nonequilibrium transition into right-handed twisted states, which is continuous.*

and negative $\zeta_\tau < 0$ if the dipoles are left-handed.

In this section we have not explored the full phase space of both activity types $\zeta_f - \zeta_\tau$. Instead, we focus on the nonequilibrium self-assembled cholesterics of chapter 5 and look at how contractile and extensile stresses affect the corresponding

nonequilibrium transition. For simplicity, we start with simulations of a quasi-1D system.

Let us consider contractile stresses ($\zeta_\tau < 0$) first. In Fig. 6.4 we can see the spontaneous twist transition, calculated as in chapter 5, for a sequence of increasingly high contractile stresses.

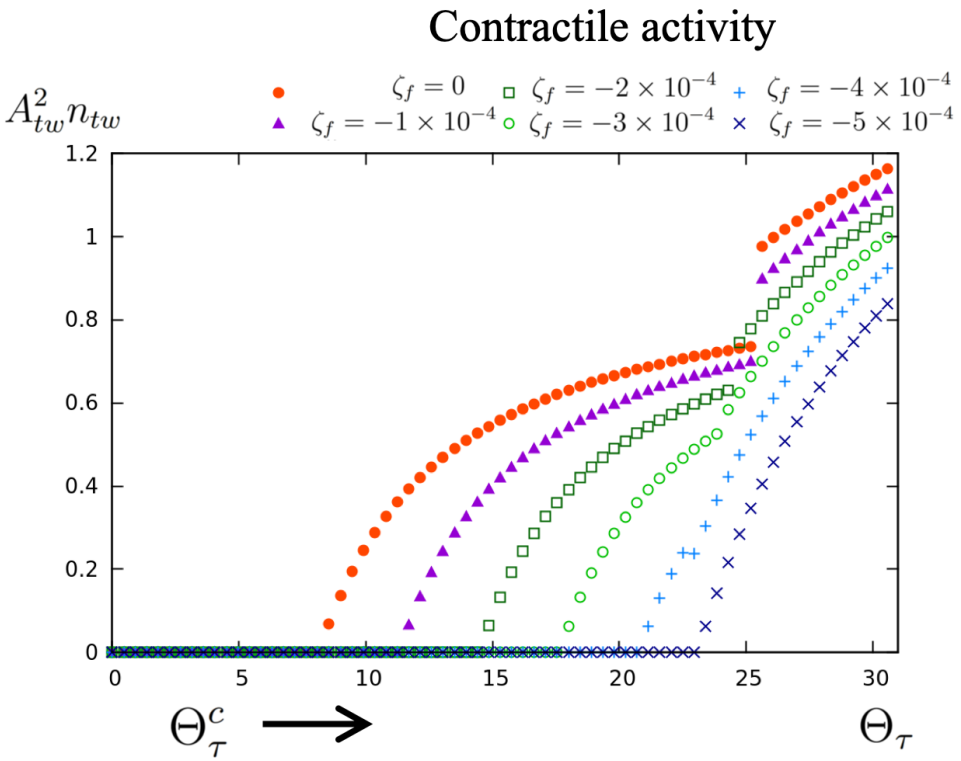

Figure 6.4 *Non equilibrium transition to spontaneously self-assembled cholesterics in the presence of contractile stresses. The critical transition parameter increases with the contractile activity, so that the spontaneously twisted phase is only accessible for higher and higher values of the chiral activity. Contractile activity is even able to suppress the transition completely.*

We observe that, as the contractile activity increases, so does the critical dimensionless chiral activity Θ_τ that controls the transition. This means that, the higher the contractile stresses, the more chiral activity is necessary to still observe spontaneously twisted states. For even stronger values of the contractile stress, the transition can be completely suppressed.

Recall that the contractile activity drives a splay hydrodynamic instability. Lubensky has shown that splay deformations are not true hydrodynamic modes of passive cholesterics and are screened at length scales comparable to the pitch [90]. In [14], the authors found that the contractile instability was suppressed by

the cholesteric phase, unless the activity was above the Kq_0^2 threshold.

In this thesis, we find that the reverse is also true and that contractile activity is able to suppress the twist deformations driven by the chiral activity. In the literature, active droplets with comparable contractile and chiral stresses can swim in a helical trajectory but with opposite helicity to that of the microscopic chiral stress [85].

On the other hand, bend deformations are true hydrodynamic modes in a cholesteric [90]. Figure 6.5 depicts the spontaneous twist transition for different fixed values of extensile activity $\zeta_f > 0$. We find that the onset of the transition changes due to the extensile activity. As a matter of fact, the critical value of the chiral activity necessary for the transition decreases as the extensile activity increases. In the presence of extensile activity, the system is also able to twist even if ζ_τ is zero. This phenomenon hints at the fact that there is an equivalence between the bend deformations of the extensile instability and the twist caused by chiral stresses.

In quasi-2D systems with extensile and chiral activities, we can also observe the cholesteric pitch-splay instability (see Fig. 6.6). In these configurations, the cholesteric layers are formed and then bend, assuming an undulating shape (see Suppl. Movies 6.1 and 6.2[1])). In Fig. 6.6 (a) and (d) we can see the layer twist through the out-of-plane component of the polarisation (p_x). The in-plane configuration (p_y, p_z) is bent (see Fig. 6.6 (b) and (e)). The fluid velocity induced by these deformations is shown in Fig. 6.6 (c) and (f). Because the layers bend back and forth, the flow profile is made of opposing vortices so that the layers are not motile.

The splay-bend deformation has been explained in [14, 90]. The mode with undulating layers can be seen as a bend deformation of the polarisation along the pitch axis or, equivalently, as a pure splay of the pitch (see Fig. 6.7). In extensile fluids, a small bend distortion of this form gives rise to active flows (blue arrows in Fig. 6.7), causing the bent areas to grow and driving the instability.

Finally, we also observe states where the bent cholesteric layers are motile (see Fig. 6.8 and Suppl. Movie 6.3). In this case, instead of an undulated pattern, we see that the layers are bent into a "U" shape. With the majority of the bend

[1] All the movies referred to in this Chapter can be found in the Supplementary Materials on DataSync (https://datasync.ed.ac.uk/index.php/s/AjP4ZfSEl07uHiV?path=%2F). Appendix D contains a short description of all the Chapter 6 Suppl. Movies.

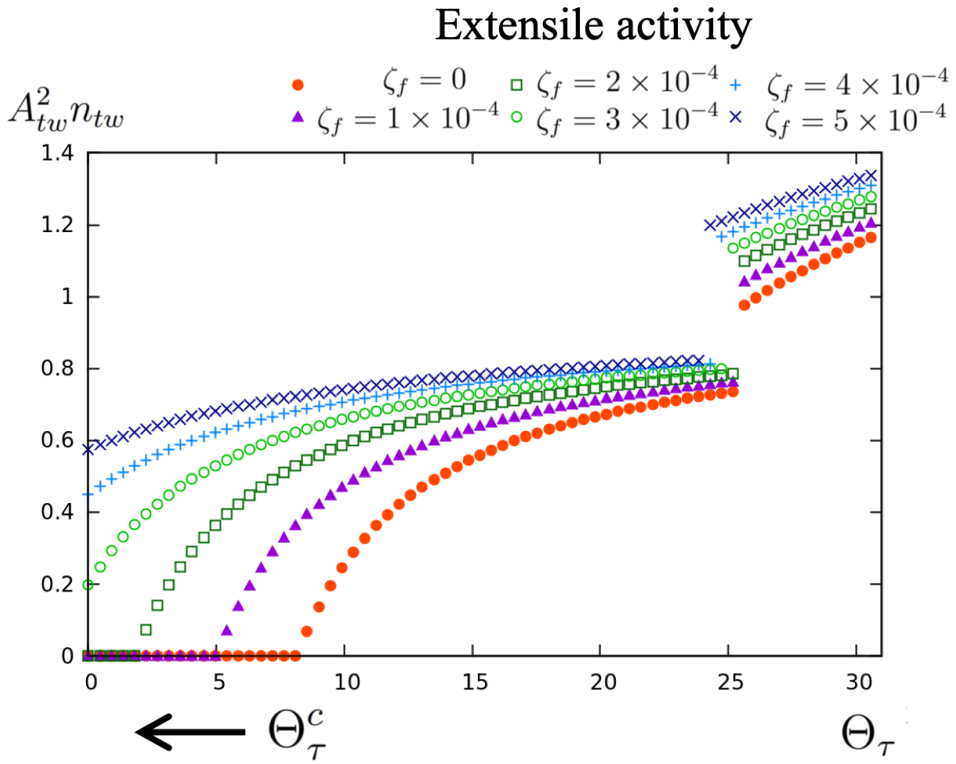

Figure 6.5 *Nonequilibrium transition to a spontaneous self-assembled cholesteric in the presence of achiral extensile stresses. The critical chiral activity necessary to observe spontaneously twisted states decreases with extensile activity. For high values of the extensile activity, we can even observe twist deformations when* $\zeta_\tau = 0$.

areas pointing in the same direction, the net velocity causes the system to drift upwards.

The patterns of undulating or bent layers, with both bend and twist instabilities, are observed when the achiral and chiral activities are comparable. When one of the active stress terms is dominant over the other, we have either only bend or only twist instabilities, corresponding to the regimes studied in chapters 4 and 5, respectively.

6.3 Concluding remarks

In a general realisation of biological active fluids, we expect that microscopic chirality may arise from the intrinsic molecule asymmetry (thermodynamic), or from the chiral trajectories of motors, filaments, and flagella (active). Earlier

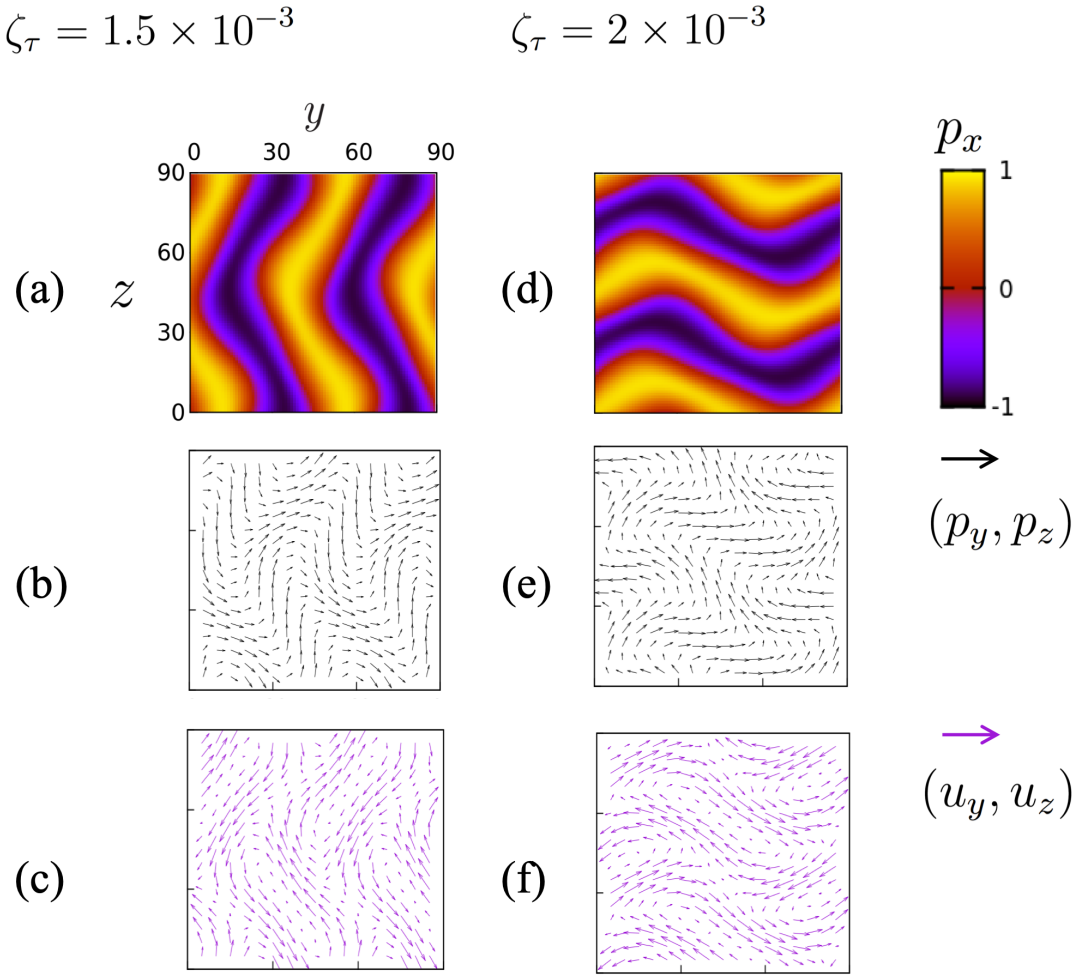

Figure 6.6 *Undulated cholesteric layers for an active quasi-2D system with extensile activity $\zeta_f = 5 \times 10^{-3}$ and chiral activity equal to: (a)-(c) $\zeta_\tau = 1.5 \times 10^{-3}$, and (c)-(f) $\zeta_\tau = 1.5 \times 10^{-3}$. The shape of the cholesteric layers can be seen in (a) and (d) thought the out-of-plane polarisation component p_x. The in-plane bending of (p_y, p_z) is shown in (b) and (e). Finally, the in-plane fluid flow (u_y, u_z) is depicted in (c) and (e). The flow exhibits several vortices with opposing directions so that the layers are non-motile.*

in this thesis, we showed that active chirality leads to the self-assembly of nonequilibrium cholesteric phases. These share many of the characteristics of typical equilibrium cholesterics.

In this chapter we have provided a comparison, albeit not an extensive one, between thermodynamic and active chirality in active fluid systems.

First, we showed that chiral active stresses can change the equilibrium twisted states of cholesterics, adding or removing cholesteric layers (or twists). When the equilibrium and active states have the same chirality (*e.g.* both are right-handed),

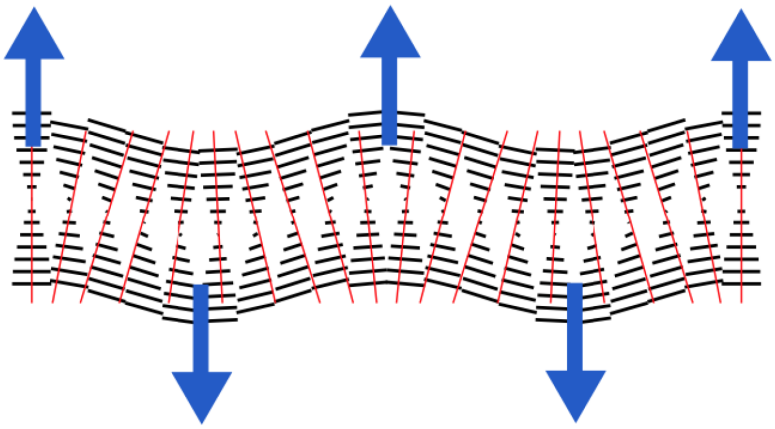

Figure 6.7 *Sketch of the pitch-splay instability (or layer undulation) in extensile cholesterics. Black lines show the projection of the orientation field while red lines represent the pitch axis and its splay. The blue arrows show the active flow direction. This flow results from the bend deformations and increases the distortion, driving the instability. Figure and description produced from [14]*

chiral stresses can increase the number of twists in the system. Conversely, when there is a chirality mismatch, the active chiral stresses are able to untwist the equilibrium cholesteric phase, one layer at a time, until an aligned state is reached. Once the system is aligned, we can observe a nonequilibrium transition to self-assembled cholesterics with twist in the opposite sense.

We have also looked at the coupling between chiral and achiral active stresses. We found that contractile activity inhibits the spontaneous twist transition to nonequilibrium cholesterics, while extensile activity enhances it. This is due to the fact that contractile splay instabilities are not true hydrodynamic modes in cholesterics, unlike the extensile bend deformations. In quasi-2D systems, we find examples of the pitch-splay instability characteristic of active cholesterics, where the twisted layers are bent due to extensile stresses. Depending on the spatial distribution of bend deformations, these states can either be motile or not.

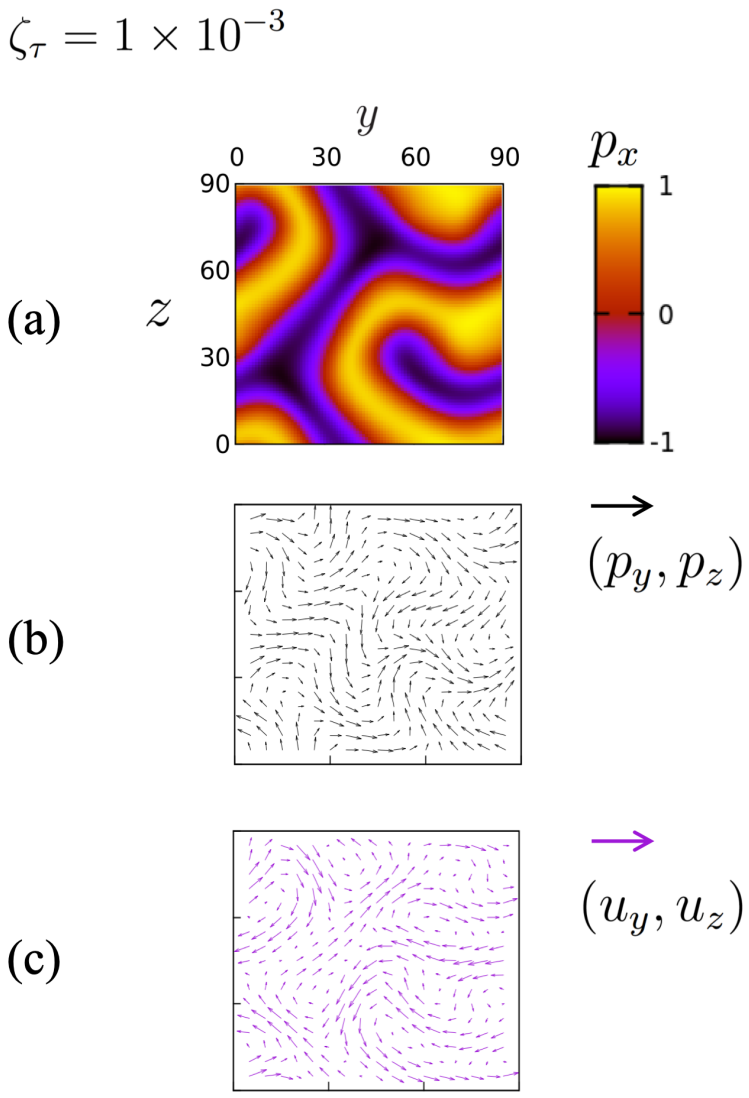

Figure 6.8 *Motile bent layers in an active quasi-2D system with extensile and chiral activities equal to* $\zeta_f = 5{\times}10^{-3}$ *and* $\zeta_\tau = 1{\times}10^{-3}$*, respectively. (a) Out-of-plane component of the orientation* (p_x) *showing the cholesteric twisting in the layers. (b)* (p_y, p_z) *showing the in-plane bent patterns in the orientation. (c) In-plane velocity field causing the layers to drift upwards.*

Chapter 7

Conclusions

In this thesis we have computationally explored a wide range of flowing or motile configurations in active fluids. Remarkably, chirality has played a role in all of our results, albeit in two very distinct ways. In the case of the rotating droplets (chapter 4), chirality emerges at the macroscopic scale in selecting the sense of rotation, whilst in our discussions of active chiral fluids (chapters 5 and 6), it is an intrinsic microscopic feature of the active particles constituting the fluid. We will now present an overview of those results, highlighting the different types of chiral processes observed.

We started, in chapter 4, by simulating an active gel droplet with strong anchoring conditions at the interface. An active gel droplet can be seen as a very simplified model for a bacterial colony or an actomyosin extract, providing valuable insight into the mechanics of living systems. Active droplets exhibit incredibly rich dynamics, including self-motile states in two and three dimensions [4]. We have found that both extensile and contractile droplets can also spontaneously rotate. The transition between quiescent and spontaneously rotating states is a nonequilibrium one, and is driven by active stresses in the fluid. The conditions leading to rotating states also depend on the nature of the anchoring (the orientation of the active force dipoles at the droplet boundary): extensile droplets rotate if the anchoring is normal to the interface, while contractile droplets do so only if the anchoring is planar. A sufficiently strong thermodynamic anchoring is also a necessary condition for rotation; without it the droplets instead translate. For that reason, we also call the rotations observed "anchoring-driven". The full mechanism can be described as follows: when the activity is sufficiently high to

trigger hydrodynamic instabilities, regions of bend (extensile stresses) or splay (contractile stresses) are formed inside the droplet; the areas of deformation are associated with locally unbalanced active forces and generate spontaneous flows; the anchoring plays a role in stabilising two of these deformations, with opposite directions; if the two forces are not collinear, for instance due to a fluctuation, they create an active torque which rotates the droplet. Rotating droplets resulting from this mechanism are also "bean" or "S" shaped, and occur for finite values of the surface tension, distinguishing them from circular rotating spirals [70, 91].

A rotating active droplet is macroscopically chiral. In the "anchoring-driven" rotations of chapter 4, chirality is a result of spontaneous symmetry breaking, so that droplets can rotate in either a clockwise or anticlockwise sense with equal probabilities. In chapters 5 and 6 we instead look at a different class of chiral system. This time we start from the consideration that in *E. coli* and actomyosin suspensions, each of the active particles constituting the system is microscopically chiral and generates an active torque, so that the resulting active fluid is generically chiral. Such chiral active systems are still relatively unexplored in the literature.

In chapter 5, we introduce the active stress needed to describe a system of active torque dipoles, and demonstrate, in quasi-1D and quasi-2D systems, the existence of a novel nonequilibrium cholesteric phase, which is self-assembled. This cholesteric phase is a consequence of active chiral stresses and exists in the absence of any thermodynamic term favouring chirality. Within this phase, we observe several patterns which resemble equilibrium cholesterics, such as the formation of cholesteric layers and fingering patterns, and the existence of non-singular topological defects. However, because the self-assembled cholesteric is active, all twisted configurations are accompanied by a spontaneous fluid flow, which is also chiral. The transition from an aligned state to a spontaneously twisted configuration upon the increase of chiral activity is continuous. In contrast, activity can also drive a discontinuous transition between twisted states with a different number of twists. For even higher values of the activity, the twisting of the layers can change dynamically, which results in turbulent-like states with seemingly chaotic dynamics. We also investigate a dry system of torque dipoles, as a model system for situations where the active particle suspension is in contact with a wall which provides a momentum sink. In this case, we again find a nonequilibrium transition into spontaneously twisted states. Yet, for the dry system, the transition is discontinuous.

We explore active chiral fluids further by considering the coupling with thermodynamic chirality (*i. e.* equilibrium cholesterics). In chapter 6, we show that chiral active stresses can change the twisted states of equilibrium cholesterics, by adding or removing cholesteric layers. Curiously, the chiral active stresses can even untwist an equilibrium cholesteric phase, one layer at a time, until an aligned state is reached – for this phenomenon to arise, we require the thermodynamic chirality to conflict with the nonequilibrium chirality emerging from the active torque stress.

Finally, we looked at a more general description of active fluids, including both chiral and achiral stresses (*i.e.*, both active torque and force dipoles). Our results show that contractile activity suppresses spontaneous chiral states, while extensile activity enhances them. This is because the contractile splayed states do not correspond to true hydrodynamic modes of a cholesteric phase. For systems with both extensile and chiral stresses we observe the pitch-splay instability reported in active cholesterics. This instability results in patterns of undulating layers, which can be motile depending on their spatial arrangement.

We would like to conclude by noting that many examples of microscopic and macroscopic chirality can be found in nature, from the swimming of microorganisms to the positions of internal organs in vertebrates. Thus, we believe that a true description of biological active systems must include active chiral processes. We hope that this study can contribute to the advance of the field and to the understanding of emergent chiral patterns in active systems.

Appendix A

Boundary conditions for the hybrid lattice Boltzmann method

In this appendix, we present the conditions necessary to impose boundary conditions with the hybrid lattice Boltzmann method of chapter 3.

A.1 Non-slip BC for fluid velocities

The most common boundary condition for the fluid velocity $\mathbf{u}$ at a solid wall is the non-slip one.

Let us take for this derivation a wall located at $z = 0$. The non-slip condition at this wall corresponds to:

$$\mathbf{u}\,(z = 0) = \mathbf{0}\ . \tag{A.1}$$

Substituting Eq. (3.4) for the fluid velocity, we find the equivalent condition for the distribution functions f_i:

$$\sum_i f_i \mathbf{e}_i = 0,\ \text{at}\ z = 0\ . \tag{A.2}$$

We now equate the x-th, y-th and z-th components to obtain:

$$f_1 + f_7 + f_8 + f_{10} + f_{14} - f_3 - f_8 - f_9 - f_{12} - f_{13} = 0 \tag{A.3}$$

$$f_2 + f_7 + f_8 + f_{11} + f_{12} - f_4 - f_9 - f_{10} - f_{13} - f_{14} = 0 \tag{A.4}$$

$$f_5 + f_7 + f_8 + f_9 + f_{10} - f_6 - f_{11} - f_{12} - f_{13} - f_{14} = 0 \tag{A.5}$$

At the wall $z = 0$, (and referring back to Fig. 3.1) we have five unknown distributions: f_5, f_7, f_8, f_9, and f_{10}. Therefore, we need two more equations in this system to uniquely define the unknown distributions. These can be chosen arbitrarily. One possible choice is to use symmetry arguments as in [9]:

$$f_7 - f_8 = f_{10} - f_9 \tag{A.6}$$

$$f_5 = f_6 \tag{A.7}$$

The solution to the 5-equation system above results in the explicit non-slip conditions for the distributions f_i at $z = 0$.

$$\begin{cases} f_5 &= f_6 \\ f_7 &= \frac{1}{4}\left(-f_1 - f_2 + f_3 + f_4 - f_{11} + f_{12} + 3f_{13} + f_{14}\right) \\ f_8 &= \frac{1}{4}\left(f_1 - f_2 - f_3 + f_4 + f_{11} - f_{12} + f_{13} + 3f_{14}\right) \\ f_9 &= \frac{1}{4}\left(f_1 + f_2 - f_3 - f_4 + 3f_{11} + f_{12} - f_{13} + f_{14}\right) \\ f_{10} &= \frac{1}{4}\left(-f_1 + f_2 + f_3 - f_4 + f_{11} + 3f_{12} + f_{13} - f_{14}\right) \end{cases} \tag{A.8}$$

The equivalent treatment for $z = L_z$ yields the result:

$$\begin{cases} f_6 &= f_5 \\ f_{11} &= \frac{1}{4}\left(-f_1 - f_2 + f_3 + f_4 - f_7 + f_8 + 3f_9 + f_{10}\right) \\ f_{12} &= \frac{1}{4}\left(f_1 - f_2 - f_3 + f_4 + f_7 - f_8 + f_9 + 3f_{10}\right) \\ f_{13} &= \frac{1}{4}\left(f_1 + f_2 - f_3 - f_4 + 3f_7 + f_8 - f_9 + f_{10}\right) \\ f_{14} &= \frac{1}{4}\left(-f_1 + f_2 + f_3 - f_4 + f_7 + 3f_8 + f_9 - f_{10}\right) \end{cases} \tag{A.9}$$

These boundary conditions are implemented at the walls by changing the values of f_5, f_7, f_8, f_9, and f_{10} at $z = 0$, and the values of f_6, f_{11}, f_{12}, f_{13}, and f_{14} at $z = L_z$, after each updating step.

A.2 Boundary conditions for the order parameters

Our system has two order parameters, the hydrodynamic fields introduced in chapter 2: one scalar – the concentration ϕ (see Eq. 2.1); and one vectorial – the polarisation $\mathbf{p}$ (see Eq. 2.2). For the concentration, the simplest boundary condition is the no-flux condition, where the current across the wall is set to zero:

$$j_z(z=0) = -M\frac{\partial \mu}{\partial z}(z=0) = 0 \ . \tag{A.10}$$

We add to this a neutral wetting condition (wetting angle 90^o):

$$\frac{\partial \phi}{\partial z}(z=0) = \frac{\partial^2 \phi}{\partial z^2}(z=0) = 0 \ . \tag{A.11}$$

For the polarization vector $\mathbf{p}$, one can choose to have it anchored to the wall (typically planar) or simply free. The following conditions model the two situations:

$$\begin{cases} \text{free} & : \frac{\partial p_{x,y,z}}{\partial z}(z=0) = 0; \\ \text{planar degenerate} & : \frac{\partial p_{x,y}}{\partial z}(z=0) = 0, \text{ and } p_z(z=0) = 0 \ . \end{cases} \tag{A.12}$$

Appendix B

Chapter 4 Supplementary Movies

The supplementary movies for chapter 4 can be found in the following link on DataSync: https://datasync.ed.ac.uk/index.php/s/AjP4ZfSEl07uHiV?path=%2FSupplementary_Materials%2FSupplementary_Movies_Chapter4. The directory is password protected, please contact the author if you do not have the password.

All the movies represent the time evolution (t in simulation units) of a two-dimensional active gel droplet, illustrating different types of movement. The entire system (a square box of side 120 lattice units, with periodic boundary conditions) is represented. The colours refer to the concentration of active material: red is the concentration $\phi = 2$ inside the droplet, and white represents concentration $\phi = 0$ outside; the transition values have been coloured in blue to facilitate the visualisation of the interface. The arrows (or rods – in movies 7 and 8 for the nematic case) represent the average particle orientation inside the droplet.

Supplementary Movie 4.1: *Rotating Extensile Droplet (normal anchoring)*

For high enough activity ($\zeta = 0.007$ in the system represented) extensile active droplets with imposed normal anchoring spontaneously rotate. First, the droplet elongates in the direction of the polarisation, while remaining static. Then, the droplet deforms to assume a "bean-shape" and starts to rotate (anti-clockwise in the movie). The rotation is powered by two internal bend deformations. These distortions lead to active forces that push the droplet in different directions and

cause it to rotate.

Supplementary Movie 4.2: *Oscillating Extensile Droplet (normal anchoring)*

For intermediate values of the activity ($\zeta = 0.005$ in the system represented) active droplets with imposed normal anchoring exhibit oscillatory motion. After the initial elongated, static state, the droplet starts to rotate intermittently, alternating between clockwise and counter-clockwise movements. When switching between the two senses of rotation, the droplet is maximally elongated and minimally bent.

Supplementary Movie 4.3: *Stop-and-go Rotating Extensile Droplet (normal anchoring)*

Close to the onset of steady rotation ($\zeta = 0.0054$ in the system represented) droplets rotate always in the same sense but with a stop-and-go type of movement. The shape of the droplet varies, being more elongated and aligned when the rotation slows down and more deformed and bent when the droplet rotates.

Supplementary Movie 4.4: *Rotating Contractile Droplet (planar anchoring)*

High enough contractile activity ($\zeta = -0.0065$ in the system represented) causes active droplets to spontaneously rotate for an imposed planar anchoring. The droplet starts by elongating in the direction perpendicular to the polarisation, remaining static. Then, the droplet deforms into a "S-shape" and starts to rotate (clockwise in the movie). The rotation is, this time, powered by a pair of internal splay deformations. Just like in the extensile case, the distortions lead to active forces that push the droplet in different directions, causing it to rotate.

Supplementary Movie 4.5: *Rotating Asymmetric Contractile Droplet (planar anchoring)*

For significantly high values of the contractile activity ($\zeta = -0.0080$ in the system represented) rotating active droplets with imposed planar anchoring exhibit an asymmetric shape and rotate around a point that does not coincide with the center of mass. This is most likely a centrifugal effect caused by the increasing rotational velocity.

Supplementary Movie 4.6: *"Walking" Extensile Droplet (normal anchoring)*

In the regime of high activity and intermediate anchoring strength ($\zeta = -0.0080$ and $W = -0.03$ in the system represented) extensile droplets with normal imposed anchoring exhibit a hybrid type of movement. This exotic dynamics arises from a combination between translation and rotation. As the droplet alternates motile spells and partial rotations, it gives the impression of moving in small "steps".

Simulations of nematic systems (used to generate movies 7 and 8) have been run using a slightly different set of parameters from the polar active gel simulations (stated in the main text). For the nematic case, we have used: $A = 0.16$, $K = 0.08$, $\alpha = 0.5$, $\kappa = 0.01$, $\xi = 1.1$, and $W = 0.1, -0.1$ for planar and normal anchoring, respectively.

Supplementary Movie 4.7: *Rotating Nematic Extensile Droplet (normal anchoring)*

Nematic extensile droplets (the activity parameter value in the system represented is $\zeta = 0.0025$) rotate for an imposed normal anchoring, in an analogous way to polar extensile droplets with rotation powered by a pair of elastic deformations.

Supplementary Movie 4.8 *Rotating Nematic Contractile Droplet (Planar anchoring)*

The nematic analogue of the polar contractile rotating state is found in nematic contractile droplets ($\zeta = -0.0035$ in the system represented)for an imposed planar anchoring as well.

Appendix C

Chapter 5 Supplementary Movies

The supplementary movies for chapter 5 can be found in the following link on DataSync: https://datasync.ed.ac.uk/index.php/s/AjP4ZfSEl07uHiV?path=%2FSupplementary_Materials%2FSupplementary_Movies_Chapter5. The directory is password protected, please contact the author if you do not have the password.

The following movies correspond to the time evolution of a quasi-2D system of active torque dipoles, with positions on a square layer of dimensions $L_y \times L_z = 100 \times 100$. At the boundaries, we have applied periodic conditions. The system's simulation parameters are quoted in the main text, here elasticity $K = 0.04$. Also as in the main text, the colour scale maps the polarisation component p_x, which is perpendicular to the plane $y \perp z$ of the system. Note that in quasi-2D systems of torque dipoles, we observe twisted states with the twist direction on the $y \perp z$ plane. Visualising p_x allows us to understand the areas where the polarisation twists out of the plane.

Supplementary Movie 5.1: *Transient defect dynamics*

For low values of the chiral activity ζ_τ (here $\zeta_\tau = 1 \times 10^{-4}$), we observe a transient state with topological defects. The defects are formed in two pairs of $\{+1, -1\}$ topological charge, as we can see from the orientation (the black arrows indicate the in-plane polarisation). Because of the twist deformations in the system (which are due to the chiral active stresses), the defects are not singular in the order parameter: the polarisation instead escapes into the x dimension (perpendicular

to the plane). The presence of non-singular defects is also common in equilibrium cholesterics. The defects drift slightly over time, as the system attempts to align, and then annihilate with the oppositely charged defect of the pair.

Supplementary Movie 5.2: *Turbulent states in nonequilibrium cholesterics*

For high values of the chiral activity ζ_τ (here $\zeta_\tau = 4\times10^{-2}$), we observe turbulent-like states. In these states, the orientation twists in different directions, forming a "leaf"-shaped pattern of cholesteric layers with competing orientations. The layers are continuously formed and rotated, resulting in a state that is seemingly chaotic. The dynamics of this state resembles active turbulence in active nematics and bacterial colonies.

Appendix D

Chapter 6 Supplementary Movies

The supplementary movies for chapter 6 can be found in the following link on DataSync: https://datasync.ed.ac.uk/index.php/s/AjP4ZfSEl07uHiV?path=%2FSupplementary_Materials%2FSupplementary_Movies_Chapter6. The directory is password protected, please contact the author if you do not have the password.

The movies correspond to the time evolution (t in simulation units) of a quasi-2D active fluid, with both extensile and chiral active stresses. The size of the system is $L_y \times L_z = 90 \times 90$ and periodic conditions are applied at the boundaries. The system's simulation parameters are quoted in the main text, here we also used elasticity $K = 0.04$ and extensile activity $\zeta_f = 5 \times 10^{-3}$; chiral activity ζ_τ is different in the different movies (stated in the descriptions below). Initial conditions are aligned on the plane, with some random variation. As in the main text, the colour scale maps the polarisation component p_x, which is perpendicular to the plane $y \perp z$ of the system. Thus, the periodic variation of p_x between 1 and -1 depicts a cholesteric-like twist, and allows us to distinguish "cholesteric layers".

Supplementary Movie 6.1: *Undulated cholesteric layers (vertical)*

Formation of undulated cholesteric layers due to the pitch-splay instability. We first observe fluctuations of the polarisation and twist, then the system stabilises with 2 vertical layers, which undulate. This is due to the extensile stresses setting up a pitch-splay instability. The bent regions induce active flows. However,

because there are two symmetric bends (back and forth), the fluid flows describing closed vortices and the systems is static (see figures in the main text). The chiral activity in the system is $\zeta_\tau = 1.5 \times 10^{-3}$.

Supplementary Movie 6.2: *Undulated cholesteric layers (horizontal)*

Similar to Suppl. Movie 6.1, here the formation of undulated layers is shown. In this case, the layers have a different orientation - horizontal. We observe some fluctuations in the twist and polarisation, followed by the formation of 2 horizontal layers, which are bent due to the pitch-splay instability. As in the previous case, the resultant fluid flow consists of closed vortices, and the layers do not move. The chiral activity in the system is $\zeta_\tau = 2 \times 10^{-3}$.

Supplementary Movie 6.3: *Bent cholesteric layers, drifting over time*

When the chiral activity is low compared to the extensile one (here $\zeta_\tau = 1 \times 10^{-3}$), the cholesteric layers bend, forming a structure of closed loops, which is motile. The bending of the layers is triggered by a pitch-splay instability. Because of the shape of the configuration, the regions of bend do not compensate each other and the resultant fluid flow drifts the entire system upwards.

Bibliography

[1] William Bialek, Andrea Cavagna, Irene Giardina, Thierry Mora, Edmondo Silvestri, Massimiliano Viale, and Aleksandra M. Walczak. Statistical mechanics for natural flocks of birds. *PNAS*, 109(13):4786–4791, 2012.

[2] Abhijit P. Deshpande, J. Murali Krishnan, and P. B. Sunil Kumar. *Rheology of Complex Fluids*. Springer, 2010.

[3] Christopher Dombrowski, Luis Cisneros, Sunita Chatkaew, Raymond E. Goldstein, and John O. Kessler. Self-concentration and large-scale coherence in bacterial dynamics. *Phys. Rev. Lett.*, 93(9):098103, 2004.

[4] Elsen Tjhung, Davide Marenduzzo, and Michael E. Cates. Spontaneous symmetry breaking in active droplets provides a generic route to motility. *PNAS*, 109(31):12381–12386, 2012.

[5] M E Cates. Diffusive transport without detailed balance in motile bacteria: does microbiology need statistical physics? *Reports on Progress in Physics*, 75(4):042601, mar 2012.

[6] Tamás Vicsek, András Czirók, Eshel Ben-Jacob, Inon Cohen, and Ofer Shochet. Novel type of phase transition in a system of self-driven particles. *Phys. Rev. Lett.*, 75:1226–1229, Aug 1995.

[7] Sriram Ramaswamy. The mechanics and statistics of active matter. *Annual Review of Condensed Matter Physics*, 1(1):323–345, 2010.

[8] Knut Drescher, Jörn Dunkel, Luis H. Cisneros, Sujoy Ganguly, and Raymond E. Goldstein. Fluid dynamics and noise in bacterial cell-cell and cell-surface scattering. *PNAS*, 108(27):10940–10945, 2011.

[9] C. Denniston, D. Marenduzzo, E. Orlandini, and J. M. Yeomans. Lattice boltzmann algorithm for three-dimensional liquid-crystal hydrodynamics. *Philosophical Transactions: Mathematical, Physical and Engineering Sciences*, 362(1821):1745–1754, 2004.

[10] C. M. Pooley and K. Furtado. Eliminating spurious velocities in the free-energy lattice boltzmann method. *Phys. Rev. E*, 77:046702, Apr 2008.

[11] Luca Giomi and Antonio DeSimone. Spontaneous division and motility in active nematic droplets. *Phys. Rev. Lett.*, 112:147802, Apr 2014.

[12] S. Fürthauer, M. Strempel, S. W. Grill, and F. Jülicher. Active chiral fluids. *The European Physical Journal E*, 35(9):89, Sep 2012.

[13] M. Siva Kumar and P. Philominathan. The physics of flagellar motion of e. coli during chemotaxis. *Biophysical Reviews*, 2(1):13–20, Feb 2010.

[14] Carl A. Whitfield, Tapan Chandra Adhyapak, Adriano Tiribocchi, Gareth P. Alexander, Davide Marenduzzo, and Sriram Ramaswamy. Hydrodynamic instabilities in active cholesteric liquid crystals. *The European Physical Journal E*, 40(4):50, Apr 2017.

[15] W. C. K. Poon. From *Clarkia* to *Escherichia* and janus: the physics of natural and syntetic active colloids. *Proceedings of the International School of Physics "Enrico Fermi", Course CLXXXIV "Physics of Complex Colloids", eds. C. Bechinger, F. Sciortino and P. Ziherl, IOS, Amsterdam: SIF, Bologna*, pages 317–386, 2013.

[16] Yashodhan Hatwalne, Sriram Ramaswamy, Madan Rao, and R. Aditi Simha. Rheology of active-particle suspensions. *Phys. Rev. Lett.*, 92(11):118101, 2004.

[17] P. G. de Gennes and J. Prost. *The Physics of Liquid Crystals*. Oxford University Press, 1993.

[18] Vijay Narayan, Sriram Ramaswamy, and Narayanan Menon. Long-lived giant number fluctuations in a swarming granular nematic. *Science*, 317:105, 2007.

[19] R. Voituriez, J. F. Joanny, and J. Prost. Spontaneous flow transition in active polar gels. *Europhys. Lett.*, 70(3):404–410, 2005.

[20] M.C. Marchetti, J. F. Joanny, S. Ramaswamy, T. B. Liverpool, J. Prost, Madan Rao, and R. Aditi Simha. Hydrodynamics of soft active matter. *Rev. Mod. Phys.*, 85(3):1143(47), 2013.

[21] Charles W. Wlgemuth. Collective swimming and the dynamics of bacterial turbulence. *Biophysical Journal*, 45(4):1564–1574, 2008.

[22] S.P. Thampi and J.M. Yeomans. Active turbulence in active nematics. *The European Physical Journal Special Topics*, 225(4):651–662, Jul 2016.

[23] Nicholas C. Makris, Purnima Ratilal, Deanelle T. Symonds, Srinivasan Jagannathan, Sunwoong Lee, and Redwood W. Nero. Fish population and behavior revealed by instantaneous continental shelf-scale imaging. *Science*, 311:660, 2006.

[24] Elena O. Budrene and Howard C. Berg. Complex patterns formed by motile cells of *Escherichia coli*. *Nature*, 349:630–633, 1991.

[25] F. J. Nédélec, T. Surrey, A. C. Maggs, and S. Leibler. Self-organization of microtubules and motors. *Nature*, 389:305–308, 1997.

[26] John Toner, Yuhai Tu, and Sriram Ramaswamy. Hydrodynamics and phases of flocks. *Annals of Physics*, 318:170–244, 2005.

[27] M. Ballerini, N. Cabibbo, R. Candelier, A. Cavagna, E. Cisbani, I. Giardina, V. Lecomte, A. Orlandi, G. Parisi, A. Procaccini, M. Viale, and V. Zdravkovic. Interaction ruling animal collective behavior depends on topological rather than metric distance: Evidence from a field study. *PNAS*, 105(4):1232–1237, 2007.

[28] M. E. Cates, D. Marenduzzo, I. Pagonabarraga, and J. Tailleur. Arrested phase separation in reproducing bacteria creates a generic route to pattern formation. *PNAS*, 107(26):11715–11720, 2010.

[29] James A. Shepiro. The significance of bacterial colony patterns. *BioEssays*, 17(7):597–607, 1995.

[30] H. C. Berg. *E. coli in motion*. Springer, NY, 2004.

[31] Aparna Baskarana and M. Cristina Marchettia. Statistical mechanics and hydrodynamics of bacterial suspensions. *PNAS*, 106(37):15567–15572, 2009.

[32] Elsen Tjhung. *Phenomenology and Simulations of Active Fluids*. PhD thesis, University of Edinburgh, 2013.

[33] Sumithra Sankararaman and Gautam I. Menon. Self-organized pattern formation in motor-microtubule mixtures. *Phys. Rev. E*, 70(3):031905(18), 2004.

[34] Eric Karsenti, François Nédélec, and Thomas Surrey. Modelling microtubule patterns. *Nature Cell Biology*, 8(11):1204–1211, 2006.

[35] Alexander B. Verkhovsky, Tatyana M. Svitkina, and Gary G. Borisy. Self-polarization and directional motility of cytoplasm. *Current Biology*, 9(1):11–20, 1999.

[36] Tanniemola B. Liverpool. Active gels: where polymer physics meets cytpskeletal dynamics. *Phil. Trans. R. Soc. A*, 364:3335–3355, 2006.

[37] J. Tailleur and M. E. Cates. Sedimentation, trapping, and rectification of dilute bacteria. *EPL (Europhysics Letters)*, 86(6):60002, 2009.

[38] Howard C. Berg. Bacterial behaviour. *Nature*, 254:389–392, 1975.

[39] K. Huang. *Statistical Mechanics*. Wiley & Sons, 1986.

[40] G. De Magistris and D. Marenduzzo. An introduction to the physics of active matter. *Physica A*, 418:65–77, 2015.

[41] Tamás Vicsek and Anna Zafeiris. Collective motion. *Physics Reports*, 517(3):71 – 140, 2012. Collective motion.

[42] Guillaume Grégoire and Hugues Chaté. Onset of collective and cohesive motion. *Phys. Rev. Lett.*, 92:025702, Jan 2004.

[43] Hugues Chaté, Francesco Ginelli, Guillaume Grégoire, and Franck Raynaud. Collective motion of self-propelled particles interacting without cohesion. *Phys. Rev. E*, 77:046113, Apr 2008.

[44] K. Kruse, J. F. Joanny, F. Jülicher, J. Prost, and K. Sekimoto. Asters, vortices, and rotating spirals in active gels of plar filaments. *Phys. Rev. Lett.*, 92(7):078101(4), 2004.

[45] F. Jülicher, K. Kruse, J. Prost, and J.-F. Joanny. Active behaviour of the cytoskeleton. *Physics Reports*, 449:3–28, 2007.

[46] P. M. Chaikin and T. C. Lubensky. *Principles of Condensed Matter Physics*. Cambridge University Press, 2000.

[47] W. Kung and M. C. Marchetti. Hydrodynamics of polar liquid crystals. *Phys. Rev. E*, 73:031708, 2006.

[48] Colin Denniston, Enzo Orlandini, and J. M. Yeomans. Lattice boltzmann simulations of liquid crystal hydrodynamics. *Phys. Rev. E*, 63:056702, Apr 2001.

[49] S. A. Edwards and J. M. Yeomans. Spontaneous flow states in active nematics: A unified picture. *EPL (Europhysics Letters)*, 85(1):18008, jan 2009.

[50] Sriram Ramaswamy and Madan Rao. Active-filament hydrodynamics: instabilities, boundary conditions and rheology. *New Journal of Physics*, 9(11):423–423, nov 2007.

[51] Michael R. Swift, E. Orlandini, W. R. Osborn, and J. M. Yeomans. Lattice boltzmann simulations of liquid-gas and binary fluid systems. *Phys. Rev. E*, 54:5041–5052, Nov 1996.

[52] Michael R. Swift, W. R. Osborn, and J. M. Yeomans. Lattice boltzmann simulation of nonideal fluids. *Phys. Rev. Lett.*, 75:830–833, Jul 1995.

[53] C. Denniston, E. Orlandini, and J. M. Yeomans. Simulations of liquid crystal hydrodynamics in the isotropic and nematic phases. *EPL (Europhysics Letters)*, 52(4):481, 2000.

[54] M. E. Cates, O. Henrich, D. Marenduzzo, and K. Stratford. Lattice boltzmann simulations of liquid crystalline fluids: active gels and blue phases. *Soft Matter*, 5:3791–3800, 2009.

[55] A. Tiribocchi, N. Stella, G. Gonnella, and A. Lamura. Hybrid lattice boltzmann model for binary fluid mixtures. *Phys. Rev. E*, 80:026701, Aug 2009.

[56] R. Benzi, S. Succi, and M. Vergassola. The lattice boltzmann equation: theory and applications. *Physics Reports*, 222(3):145 – 197, 1992.

[57] Shiyi Chen and Gary D. Doolen. Lattice boltzmann method for fluid flows. *Annual Review of Fluid Mechanics*, 30(1):329–364, 1998.

[58] P. L. Bhatnagar, E. P. Gross, and M. Krook. A model for collision processes in gases. i. small amplitude processes in charged and neutral one-component systems. *Phys. Rev.*, 94:511–525, May 1954.

[59] E. Tjhung, A. Tiribocchi, D. Marenduzzo, and M. E. Cates. A minimal physical model captures the shapes of crawling cells. *Nature Communications*, 6:5420, 2015.

[60] Tim Sanchez, Daniel T. N. Chen, Stephen J. DeCamp, Michael Heymann, and Zvonimir Dogic. Spontaneous motion in hierarchically assembled active matter. *Nature*, 491:431–434, November 2012.

[61] Carl A. Whitfield, Davide Marenduzzo, Raphaël Voituriez, and Rhoda J. Hawkins. Active polar fluid flow in finite droplets. *The European Physical Journal E*, 37(2):8, Feb 2014.

[62] Carl A Whitfield and Rhoda J Hawkins. Instabilities, motion and deformation of active fluid droplets. *New Journal of Physics*, 18(12):123016, 2016.

[63] S. Yabunaka, T. Ohta, and N. Yoshinaga. Self-propelled motion of a fluid droplet under chemical reaction. *The Journal of Chemical Physics*, 136(7):074904, 2012.

[64] Natsuhiko Yoshinaga. Spontaneous motion and deformation of a self-propelled droplet. *Phys. Rev. E*, 89:012913, Jan 2014.

[65] Shashi Thutupalli, Ralf Seemann, and Stephan Herminghaus. Swarming behavior of simple model squirmers. *New Journal of Physics*, 13(7):073021, 2011.

[66] M. Schmitt and H. Stark. Swimming active droplet: A theoretical analysis. *EPL (Europhysics Letters)*, 101(4):44008, 2013.

[67] Matthew L. Blow, Sumesh P. Thampi, and Julia M. Yeomans. Biphasic, lyotropic, active nematics. *Phys. Rev. Lett.*, 113:248303, Dec 2014.

[68] Giulio De Magistris, Matthew L. Blow, and Davide Marenduzzo. Arrested phase separation in biphasic active nematics. *in preparation*, 2016.

[69] S. A. Edwards and J. M. Yeomans. Spontaneous flow states in active nematics: A unified picture. *EPL (Europhysics Letters)*, 85(1):18008, 2009.

[70] K. Kruse, J. F. Joanny, F. Jülicher, J. Prost, and K. Sekimoto. Asters, vortices, and rotating spirals in active gels of polar filaments. *Phys. Rev. Lett.*, 92:078101, Feb 2004.

[71] J. Elgeti, M. E. Cates, and D. Marenduzzo. Defect hydrodynamics in 2d polar active fluids. *Soft Matter*, 7:3177–3185, 2011.

[72] Carsten Krüger, Gunnar Klös, Christian Bahr, and Corinna C. Maass. Curling liquid crystal microswimmers: A cascade of spontaneous symmetry breaking. *Phys. Rev. Lett.*, 117:048003, Jul 2016.

[73] Diana Khoromskaia and Gareth P Alexander. Vortex formation and dynamics of defects in active nematic shells. *New Journal of Physics*, 19(10):103043, nov 2017.

[74] J. Schwarz-Linek, C. Valeriani, A. Cacciuto, M. E. Cates, D. Marenduzzo, A. N. Morozov, and W. C. K. Poon. Phase separation and rotor self-assembly in active particle suspensions. *Proceedings of the National Academy of Sciences*, 109(11):4052–4057, 2012.

[75] Peter Satir. Chirality of the cytoskeleton in the origins of cellular asymmetry. *Philosophical Transactions of the Royal Society of London B: Biological Sciences*, 371(1710), 2016.

[76] Robert H.Depue Jr and Robert V. Rice. F-actin is a right-handed helix. *J. Mol. Biol.*, 12:302–303, 1965.

[77] Sundar Ram Naganathan, Sebastian Fürthauer, Masatoshi Nishikawa, Frank Jülicher, and Stephan W Grill. Active torque generation by the actomyosin cell cortex drives left–right symmetry breaking. *eLife*, 3:e04165, dec 2014.

[78] Yee Han Tee, Tom Shemesh, Visalatchi Thiagarajan, Rizal Fajar Hariadi, Karen L. Anderson, Christopher Page, Niels Volkmann, Dorit Hanein, Sivaraj Sivaramakrishnan, Michael M. Kozlov, and Alexander D. Bershadsky. Cellular chirality arising from the self-organization of the actin cytoskeleton. *Nature Cell Biology*, 17:445–457, 2015.

[79] Alex Mogilner and Ben Fogelson. Cytoskeletal chirality: Swirling cells tell left from right. *Current Biology*, 25(12):R501 – R503, 2015.

[80] Christian Pohl and Zhirong Bao. Chiral forces organize left-right patterning in c. elegans by uncoupling midline and anteroposterior axis. *Developmental Cell*, 19(3):402 – 412, 2010.

[81] Christopher L. Henley. Possible mechanisms for initiating macroscopic left-right asymmetry in developing organisms. *AIP Conference Proceedings*, 1134(1):54–62, 2009.

[82] Somdeb Ghose and R. Adhikari. Irreducible representations of oscillatory and swirling flows in active soft matter. *Phys. Rev. Lett.*, 112:118102, Mar 2014.

[83] On Shun Pak and Eric Lauga. Generalized squirming motion of a sphere. *Journal of Engineering Mathematics*, 88(1):1–28, Oct 2014.

[84] D. Marenduzzo, E. Orlandini, and J. M. Yeomans. Permeative flows in cholesteric liquid crystals. *Phys. Rev. Lett.*, 92:188301, May 2004.

[85] Elsen Tjhung, Michael E. Cates, and Davide Marenduzzo. Contractile and chiral activities codetermine the helicity of swimming droplet trajectories. *Proceedings of the National Academy of Sciences*, 114(18):4631–4636, 2017.

[86] Maria Strempel, Sebastian Fürthauer, Stephan Grill, and Frank Jülicher. Thin films of chiral motors. 12 2011.

[87] Yilin Wu, Basarab G. Hosu, and Howard C. Berg. Microbubbles reveal chiral fluid flows in bacterial swarms. *Proceedings of the National Academy of Sciences*, 108(10):4147–4151, 2011.

[88] G. De Magistris, A. Tiribocchi, C. A. Whitfield, R. J. Hawkins, M. E. Cates, and D. Marenduzzo. Spontaneous motility of passive emulsion droplets in polar active gels. *Soft Matter*, 10:7826–7837, 2014.

[89] A. R. Fialho, M. L. Blow, and D. Marenduzzo. Anchoring-driven spontaneous rotations in active gel droplets. *Soft Matter*, 13:5933–5941, 2017.

[90] Tom C. Lubensky. Hydrodynamics of cholesteric liquid crystals. *Phys. Rev. A*, 6:452–470, Jul 1972.

[91] K. Kruse, J. F. Joanny, F. Jülicher, J. Prost, and K. Sekimoto. Generic theory of active polar gels: a paradigm for cytoskeletal dynamics. *The European Physical Journal E*, 16(1):5–16, Jan 2005.

List of my Publications

[1] A. R. Fialho, M. L. Blow, and D. Marenduzzo. Anchoring-driven spontaneous rotations in active gel droplets. *Soft Matter*, 13:5933–5941, 2017.

[2] A. R. Fialho, E. Tjhung, and D. Marenduzzo. Emergence of a nonequilibrium cholesteric phase in active torque systems. *Draft in preparation.*